Downloaded from orbit.dtu.dk on: May 14, 2024

DTU Library

Long-wavelength Infrared Upconversion Spectroscopy and Imaging

Tseng, Yu-Pei

Publication date:
2019

Document Version
Publisher's PDF, also known as Version of record

Link back to DTU Orbit

Citation (APA):
Tseng, Y-P. (2019). *Long-wavelength Infrared Upconversion Spectroscopy and Imaging*. Technical University of Denmark.

General rights
Copyright and moral rights for the publications made accessible in the public portal are retained by the authors and/or other copyright owners and it is a condition of accessing publications that users recognise and abide by the legal requirements associated with these rights.

- Users may download and print one copy of any publication from the public portal for the purpose of private study or research.
- You may not further distribute the material or use it for any profit-making activity or commercial gain
- You may freely distribute the URL identifying the publication in the public portal

If you believe that this document breaches copyright please contact us providing details, and we will remove access to the work immediately and investigate your claim.

Infrared spectroscopy has found applications within diverse fields, such as environmental gas monitoring and medical applications e.g. exhaled breath analysis and cancer diagnostics. However, standard infrared detectors are suffering from the unavoidable dark noise originating from the finite temperature of the detector; even with cooling, their signal-to-noise ratio is still several orders of magnitude below that of silicon based detectors. This thesis presents the theoretical and experimental findings on a frequency upconversion detector and its potential applications.

Yu-Pei Tseng
yupts@fotonik.dtu.dk

DTU Fotonik, Risø Campus,
Frederiksborgvej 399, Building 128
4000 Roskilde

https://www.fotonik.dtu.dk

Yu-Pei Tseng

Long-wavelength Infrared Upconversion Spectroscopy and Imaging

Long-wavelength Infrared Upconversion Spectroscopy and Imaging

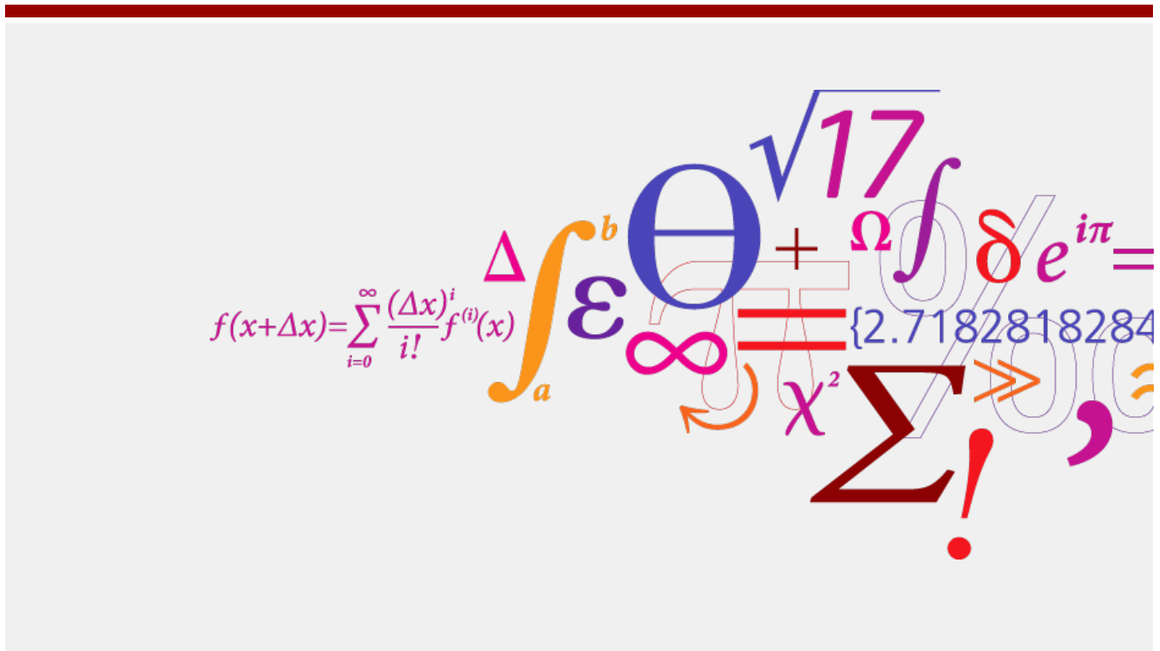

Yu-Pei Tseng
PhD Thesis, April 2019
Optical Sensor Technology Group

DTU Fotonik
Department of Photonics Engineering

Long-wavelength Infrared Upconversion Spectroscopy and Imaging

Yu Pei Tseng

Roskilde 2018

Long-wavelength Infrared Upconversion Spectroscopy and Imaging

Yu Pei Tseng

Dissertation
Department of Photonics Engineering
Technical University of Denmark

presented by
Yu Pei Tseng
from Taipei, Taiwan

Roskilde, 15. December 2018

Supervisor: Associate Prof. Peter Tidemand-Lichtenberg
Co-supervisor: Dr. Christian Pedersen

Heartfelt thanks to my family in Taiwan and those who gave me unconditional loves and constant supports in the journey

Abstract

Optical frequency conversion opens new horizons in the context of using silicon-based detectors for long-wavelength infrared (LWIR) detection, enabling tremendous scientific, technological advancement within diverse fields, such as cancer diagnostics, exhaled breath analysis, and environmental gas sensing. An infrared spectroscopic system is the fundamental tool for probing characteristic spectral signatures of molecules, e.g. in biological or gas samples, which requires sensitive and low-noise detection of LWIR signals. Mercury cadmium telluride (MCT) detectors and bolometers are the standard choices for direct LWIR detection, yet even with cooling their signal-to-noise ratio (SNR) is several orders of magnitude below that of their silicon counterparts. This thesis explores a LWIR upconversion detector, converting LWIR radiation at 9.4 µm to 12 µm into the near-infrared (NIR) range of 958 nm to 980 nm which is suitable for a silicon-based photodetector. The LWIR upconversion detector is combined with a quantum cascade laser (QCL) and a home-built microscopy unit (an X-Y translational stage) to implement a raster-scanning upconversion microscopy imaging system for analyzing microcalcifications present in a ductal carcinoma *in situ* (*DCIS*) breast cancer biopsy. This work involves the theoretical modeling and experimental characterization of the LWIR upconversion detector and the analysis of the *DCIS* biopsy in a comparison with a commercial Fourier-transform infrared (FTIR) imaging spectroscopy system.

Firstly, the LWIR upconversion detector is presented, converting the LWIR signal to the NIR, which can be acquired using a silicon detector. The LWIR upconversion detector is characterized in terms of conversion efficiency and acceptance parameters. It is subject to a theoretical modeling, which takes into account the finite beam size as well as diffraction and absorption of the infrared signal in the nonlinear crystal. A comparison between the integral approach and the plane-wave approximation is made. We show the capabilities of upconversion detection for LWIR sensing in a wide wavelength range, promising fast acquisition speeds and a good SNR even for single-pulse detection. The use of silicon detectors at room temperature can benefit a wide variety of applications employing LWIR spectroscopy.

Secondly, the upconversion detector is combined with a QCL source and a microscopy unit facilitating X-Y micro-movement for LWIR imaging detection of *DCIS*

breast cancer biopsy samples containing microcalcifications. In contrast to traditional diagnosis for cancers through examination of samples that are required to be endogenously stained, one interesting alternative way to identify a cancerous invasion in breast lesions is spectral analysis of microcalcifications without the need of endogenous staining of samples. We demonstrate an upconversion microscopy imaging system capable of providing chemical images at wavenumbers below $900\,\mathrm{cm}^{-1}$. Using a Micro-FTIR imaging system (Agilent 670) to detect LWIR images recorded below $900\,\mathrm{cm}^{-1}$ is unreliable due to unavoidable dark noise originating from the finite temperature of the LWIR detector. In contrast, the silicon detector-based LWIR upconversion imaging system enables measuring LWIR signals down to $830\,\mathrm{cm}^{-1}$, promising a better SNR in this spectral range than direct LWIR detection. The results show excellent agreement between upconversion raster scanning microscopy and Micro-FTIR imaging in terms of image structure and spectral features of breast microcalcifications. Discrete wavelength tuning of the QCL source to only relevant wavelengths with the biggest discrimination factor can substantially reduce the acquisition time.

Thirdly, a self-referencing system is being investigated with the purpose of noise reduction of the LWIR detection. The approach is to split the LWIR beam into two parts and use one as an unperturbed common-mode reference to remove the noise from the sample beam – the signal beam, which is transmitted through the sample. The experimental results show a promising degree of correlation between the signal and the reference beams, potentially allowing to improve the sensitivity and stability of the LWIR upconversion detection schemes.

Abstract

Optisk frekvenskonvertering åbner nye anvendelsesmuligheder for silicium baserede detektorer til detektion af langbølget infrarødt lys (LWIR) i videnskabelige, teknologiske formål indenfor så varierende områder som cancer diagnostik, analyse af udåndingsluft og miljøgas detektion. Et infrarødt spektroskopi system er det fundamentale værktøj til detektion af de karakteristiske spektrale signaturer af molekyler f.eks. i biologiske prøver og gasser, men det kræver følsomme sensorer med lav støj i det langbølgede spektralområde. Kviksølv cadmium tellur (MCT) detektorer og bolometre er standard for direkte detektion af LWIR, men selv med køling er deres signal til støj forhold (SNR) adskillige størrelsesordner dårligere end silicium detektorers. Denne afhandling undersøger en LWIR opkonversionsdetektor der konverterer LWIR med en bølgelængde i området 9.4 µm to 12 µm til det nær infrarøde (NIR) område 958 nm to 980 nm som kan detekteres med en silicium detektor. Denne LWIR opkonversionsdetektor er kombineret med en kvante kaskade laser (QCL) og en egenkonstrueret mikroskopenhed som kan foretage en raster skanning af en biologisk vævsprøve ved LWIR bølgelængder. Systemet er anvendt til måling af mikro forkalkninger i en vævsprøve med human brystcancer (Engelsk: ductal carcinoma *in situ*) (*DCIS*). Dette arbejde involverer teoretisk og eksperimentel karakterisering af LWIR opkonversionsdetektoren, analyse of DCIS vævsprøven og sammenligning af resultater målt med et kommercielt Fourier-transform infrarødt spektrometer (FTIR).

Først er LWIR opkonversionsdetektoren præsenteret og det beskrives hvordan et LWIR signal konverteres til et NIR signal, som kan detekteres med en silicium detektor. LWIR opkonversionsdetektorens konverterings-effektivitet og acceptansparametre er karakteriseret. Dernæst laves en teoretisk modellering som tager højde for den endelige pletstørrelse af LWIR samt diffraktion og absorption af LWIR stålingen i den ulineære krystal som er en central del af opkonverteringen og der laves en sammenligning med en planbølge model. Vi viser egenskaberne af opkonversionsdetektoren for LWIR målinger i et bredt bølgelængdeområde som muliggør høj dataopsamlingshastighed og god SNR sely for enkelt-puls detektion. Denne indirekte brug af en silicium detektorer til LWIR detektion kan benyttes i formbindelse med en lang række anvendelser, som har behov for LWIR spektroskopi.

Efterfølgende kombineres opkonversionsdetektoren med en QCL lyskilde og en mikroskopenhed med en X-Y mikrometer-platform som muliggør en 2D billeddannelse af DCIS brystcancer vævsprøverne der udviser mikroforkalkninger. I modsætning til traditionelle metoder til cancer diagnostik, som gøres ved hjælp af mikroskopi-undersøgelse af indfarvede vævsprøver, åbner dette system mulighed for at detektere mikroforkalkninger uden forudgående indfarvning. Vi demonstrerer en opkonverterings scanner med en 2D billeddannende raster scanner som optager billeder ved bølgetal under 900 cm^{-1}. Traditionelle Mikro-FTIR system (Agilent 670) til detektion af signaler under 900 cm^{-1} er upålideligt på grund af den u-undgålige mørkestrøm der skyldes temperaturen af LWIR detektoren. I sammenligning med direkte LWIR detektion, giver et opkonverterings system baseret på silicium detektorer, et bedre SNR i det spektrale område ned til 830 cm^{-1}. Resultaterne viser god overensstemmelse mellem billeder optaget med opkonverterings scanneren og det Mikro-FTIR billeddannende system hvad angår struktur og spektrale detaljer af mikroforkalkninger i brystbiopsier. QCL lyskilden kan indstilles til de specifikke bølgelængder, som giver den bedste vævs-specificitet. Herved spares tid i dataopsamlingen, da det kun er de relevante dele af spektret der registreres.

Slutteligt beskrives et system til støjreduktion baseret på en opsplitning af LWIR strålen før den anvendes til aftastning af prøven. Den ene del af strålen (referencen) passerer uden om prøven frem til detektions systemet og benyttes til støjreduktion af den del der passerer gennem prøven (målesignalet). De eksperimentelle resultater viser en høj grad af korrelation mellem referencen og målesignalet. Dette åbner mulighed for yderligere at forbedre følsomhed og stabilitet af opkonverterings princippet for LWIR.

Acknowledgments

This thesis would not have been possible without the support from many people. First and foremost, I would like to thank my supervisor, Peter Tidemand-Lichtenberg. You have been always open and supportive to my ideas, gave me suggestions and guided me through the project. I appreciate the freedom and the trust you gave to me to be able to gradually become independent in this work. On a personal level, you inspired me by your scientific dedication on establishing a link between academy and industry, always looking for a way to contribute to our society with your knowledge. I would also like to thank my co-supervisor Christian Pedersen for giving me the opportunity to work in his group.

I am grateful to my medical collaborates in Exeter University. More specifically, I would like to thank Prof. Nick Stone for his continuous support and for providing me the great opportunity to work on cancer research. I would also like to thank Pascaline Bouzy for her support and sharing in the field of biology. My sincere appreciation goes out to Henning Engelbrecht Larsen for support in LabVIEW programming and electronics which has been crucial in the project. I am thankful to Peter John Rodrigo and Michael Linde Jakobsen for sharing with me his tremendous knowledge and experience in the upconversion/optics fields. Many thanks to Finn Aage Christensen for giving me technical support. And I would like to thank Sylvain Mathonnière for his discussion of QCL device.

This work would not have been possible without the financial support for my research study through my PhD fellowship, Marie Skłodowska-Curie fellowship, Horizon 2020 research innovation programme under Grant Agreement No.642 661 and Otto Mønsteds Fond. I am grateful to all of my lab mates and the partners (Initial Training Networks, ITN) with whom I have had the pleasure to work during this project. I would like to thank Dr. Alexander Gliserin who proofread the thesis and provided insightful comments. I would also like to thank Casey Chew, Yun-Ting Hsu, Wan-Chen Lin, Wei-Ting Chen, Shao-Wei Chou, Shug-June Hwang, Ching-

Hsun Weng, Yu-Tzu Lin, and Su-Hua Shih who have unconditionally supported and encouraged me along the way during times of joy and frustration.

Last but not least, I would like to express my deepest gratitude to my siblings, Yu-Ting Tseng and Chi-Chuan Tseng, whose love and guidance are with me in whatever I pursue. This thesis would not have been possible without their warm love and endless support. This thesis is dedicated to my parents, especially to my mother in heaven, for their love and support throughout my life.

Thank you all.

Contents

Abstract **i**

Abstrakt **iii**

Acknowledgments **v**

List of publications **ix**

1 Introduction **1**
1.1 Motivation . . . 2
1.1.1 Recent progress . . . 3
1.2 Overview of this dissertation . . . 5

2 Theoretical background and fundamentals **7**
2.1 Historical overview . . . 7
2.2 Sum-frequency generation . . . 8
2.2.1 Plane-wave approximation . . . 8
2.2.2 Integral approach . . . 12

3 LWIR upconversion detector **17**
3.1 The LWIR upconversion detector . . . 17
3.1.1 LWIR source: quantum cascade laser . . . 20
3.2 Results and discussion . . . 21
3.2.1 Phase-matching angle tuning . . . 21
3.2.2 Acceptance bandwidth . . . 23
3.2.3 Upconverted intensity distribution . . . 24
3.2.4 Conversion efficiency . . . 26
3.2.5 LWIR pulse measurement . . . 29
3.3 Summary . . . 31

4 Breast cancer detection **33**
4.1 Background . . . 33
4.1.1 Standard breast cancer diagnosis . . . 33
4.1.2 label-free detection of biological samples . . . 35
4.1.3 Our approach . . . 37

4.2 Methods and Materials . . . 38
4.2.1 Early biomarker . . . 38
4.2.2 Synthetic carbonated-hydroxyapatite KBr pellets . . . 39
4.2.3 Breast cancer sample . . . 39
4.3 FTIR system . . . 40
4.3.1 Fundamental . . . 40
4.3.2 Micro-FTIR system . . . 41
4.4 First generation of the upconversion microscope imaging system . . . 42
4.4.1 Experimental setup . . . 42
4.4.2 Data acquisition . . . 43
4.4.3 Absorption spectroscopy . . . 44
4.4.4 Analysis of carbonated hydroxyapatite sample . . . 45
4.4.5 Analysis of breast cancer microcalcifications . . . 47
4.4.6 Short summary . . . 50
4.5 Second generation of the upconversion microscope imaging system . . . 51
4.5.1 Experimental setup . . . 51
4.5.2 Data acquisition . . . 52
4.5.3 Characterization of spatial resolution . . . 55
4.5.4 Microcalcifications from an *ex vivo* sample of breast *DCIS* . . . 55
4.5.5 Conclusion . . . 58

5 Preliminary study of a self-referencing system 61
5.1 Motivation . . . 61
5.2 Experimental setup . . . 61
5.3 Results . . . 62
5.4 Potential application using the self-referencing system . . . 65
5.5 Conclusion . . . 66

6 Summary and conclusions 67
6.1 Summary of the thesis . . . 67
6.2 Outlook for future work . . . 68

Appendix 71

Bibliography 75

List of publications

Y.-P. Tseng, C. Pedersen, and P. Tidemand-Lichtenberg. *Upconversion detection of long-wave infrared radiation from a quantum cascade laser*. Optical Materials Express **8** (2018) 10.1364/OME.8.001313.

Y.-P. Tseng, P. Bouzy, C. Pedersen, N. Stone, and P. Tidemand-Lichtenberg. *Upconversion raster scanning microscope for long-wavelength infrared imaging of breast cancer microcalcifications*. Biomedical optics express **9**, 4979–4987 (2018).

Y. P. Tseng, P. Bouzy, N. Stone, C. Pedersen, and P. Tidemand-Lichtenberg. *Long wavelength identification of microcalcifications in breast cancer tissue using a quantum cascade laser and upconversion detection*. Biomedical Vibrational Spectroscopy 2018: Advances in Research and Industry **10490**, 104900F (2018).

Y.-P. Tseng, C. Pedersen, and P. Tidemand-Lichtenberg. *Long-wave infrared upconverter*. In Optics InfoBase Conference Papers. Vol. Part F87-M, (2018).

Y.-P. Tseng, L. Meng, P. J. Rodrigo, P. Tidemand-Lichtenberg, and C. Pedersen. *Upconversion Detection for Gas Sensing Applications*. In, Oral presentation at the 4th International workshop on opportunities and challenges in mid-infrared laser-based gas sensing, Wroclaw, Poland. (May 2017).

P. Bouzy, Y.-P. Tseng, C. Pedersen, P. Tidemand-Lichtenberg, F. Palombo, and N. Stone. *Advances in mid-infrared spectroscopic imaging for analysis of breast cancer associated microcalcifications*. In Optics InfoBase Conference Papers. Vol. Part F87-M, (2018).

N. Hamburger, H. Hansen, F. Bak, M. Terkelsen, M. Christophersen, L. Bennedsen, Y.-P. Tseng, P. Tidemand-Lichtenberg, and C. Pedersen. *Development and test of optical sensor for real time measurement of volatile organic contaminants in air*. In, Poster Presentation (D3) at 10th international conference on remediation of chlorinated and recalcitrant compounds, Palm Springs, California, USA. (May 2016).

P. Bouzy, Y.-P. Tseng, C. Pedersen, P. Tidemand-Lichtenberg, H. Madupali, M. M. J. Tecklenburg, F. Palombo, and N. Stone. *Novel Spectroscopic Tools for Analysis of Breast Cancer associated Microcalcifications*. In, Poster presentation (78) at 10th conference SPEC 2018, Glasgow, Scotland (June 2018).

Chapter 1

Introduction

This dissertation presents a frequency upconversion detector used to convert long-wavelength infrared radiation (LWIR) of 9.4 µm to 12 µm into the wavelength region of 956 nm to 977 nm allowing for efficient, high-speed detection using standard silicon detectors. This LWIR upconversion detector is combined with a home-built raster scanning microscope imaging system for spectral analysis of microcalcifications in proliferative lesions and invasive cancer. Firstly, the LWIR upconversion was studied theoretically and characterized experimentally to elucidate the underlying parametric frequency conversion process in the long-wavelength region, which is crucial for the optimal operation of the system. Secondly, a raster scanning microscope imaging system was designed, combining a home-built microscopy unit, a quantum cascaded laser, and the LWIR upconversion detector to probe biological samples at discrete wavelengths of interest with the aim of being able to access the stages of disease progression. The system is capable of probing carbonate bands at 875 cm^{-1}, which is challenging to commercial Fourier-transform infrared spectroscopy (FTIR) systems to obtain reliable data in the LWIR regime (900 cm^{-1} to 800 cm^{-1}) due to their poor signal-to-noise ratio resulting in spectral artifacts. The project is apart of Mid-TECH consortium (Horizon 2020 research innovation, Initial Training Networks) which comprises 8 academic and industrial partners, providing doctoral training for 15 PhD students working on infrared technology with the aim of promoting infrared application. We combine infrared sources made by our partner (Humboldt University, ICFO, NKT, and Radiantis) with infrared detectors (DTU) for environmental, biological (Exeter University), and combustion (Lund University) researches.

1.1 Motivation

Many substances can be identified by their spectral features associated with fundamental rotational and vibrational absorption bands in the infrared spectral region. This has spurred much attention to infrared (IR) technologies relating to applications, such as infrared spectroscopy [1–4] and infrared hyperspectral imaging [5–8]. Infrared spectroscopy has found applications within diverse fields, such as environmental gas monitoring [9, 10] and medical applications e.g. exhaled breath analysis [11–13] and cancer diagnostics [14]. Throughout the past decades significant scientific progress has led to new mid-IR light sources, such as narrow-band optical parametric oscillators [15] and quantum cascade lasers (QCL's) [16]. Particularly the high efficiency, simple tuning properties and compact size of QCLs has made them the ideal light source for many IR applications. However, the options for infrared detection at the corresponding wavelengths are limited. Fig. 1.1 shows the normalized detectivities as a function of wavelength for a number of detectors [17].

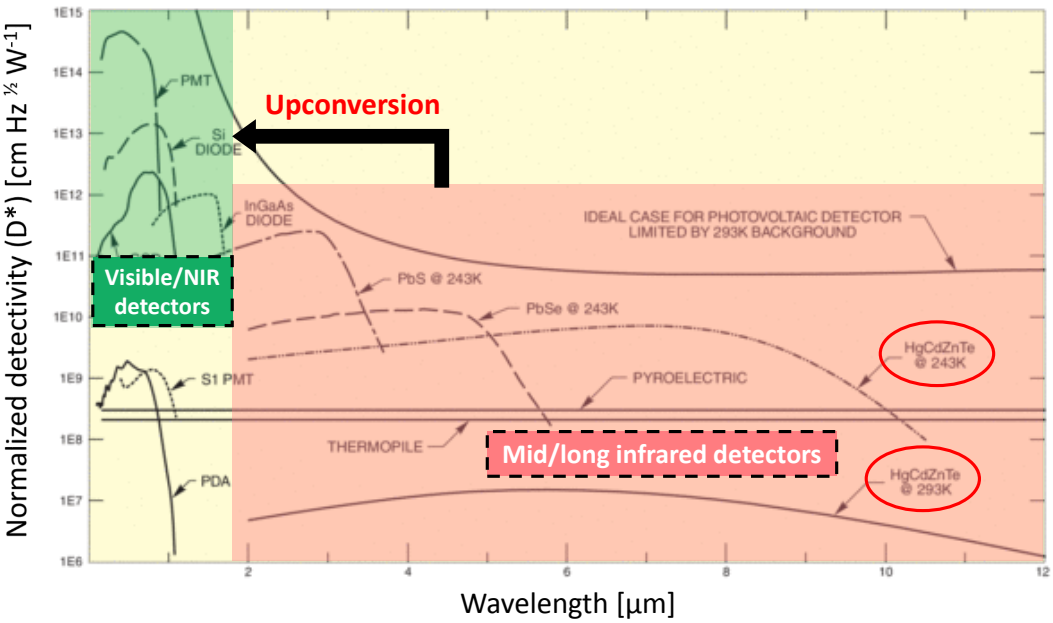

Figure 1.1: Approximate normalized detectivities as a function of wavelength for a number of detectors [17].

Typically, mercury cadmium telluride (MCT) detectors and bolometers are the standard choices for direct infrared detection. MCT detectors are widely used in spectroscopic systems, such as Fourier-transform infrared (FTIR) detectors, due to their broad spectral coverage for detection of infrared radiation. The normalized

detectivity shown in Fig. 1.1 is a figure of merit used to compare performance of different types of detectors, and defined as

$$D^* = \frac{\sqrt{A_D f}}{NEP} \tag{1.1}$$

where A_D is detector area, f is bandwidth of the detector, and NEP is the noise equivalent power, representing the radiant flux needed to obtain an output signal of the same power as the noise output from the detector. It is desirable for the NEP to be as low as possible. These LWIR detectors are suffering from the unavoidable dark noise originating from the finite temperature of the detector; therefore they are typically cooled down to liquid nitrogen temperatures (∼77 K) for noise reduction, potentially improving the signal-to-noise ratio (SNR). However, even with cooling, their SNR is still several orders of magnitude below that of silicon-based detectors. Therefore, we propose an alternative detection scheme based on frequency upconversion, translating mid and long infrared into the visible/near-infrared region for efficient, high-speed detection using a standard silicon detector without the need for cooling.

1.1.1 Recent progress

In recent years, frequency upconversion has been revitalized as an alternative approach to direct detection of infrared radiation. Upconversion relies on a nonlinear process, which is commonly referred to as sum-frequency generation. When long-wavelength (low energy) infrared photons are mixed with high-energy photons inside a nonlinear crystal, frequency upconversion from long infrared to near infrared (NIR) is realized according to energy and momentum conservation. This translation allows for simple detection of a LWIR signal using silicon detectors.

Most work on IR upconversion detection has been focused on the 1.5 µm to 5 µm range, where a $LiNbO_3$ (LN) crystal is the preferred nonlinear material. $LiNbO_3$ is broadly transparent from 0.25 µm to ∼5 µm and has been commercialized in the past decades. The effective nonlinearity (d_{eff}) of a bulk LN crystal is ∼4.6 pm/V, which is limiting the conversion efficiency. This has been improved by engineering the crystal: Fejer *et al.* [18] realized a technique called quasi-phase matching (QPM) in which the phase is corrected at assigned intervals using a structural periodicity fabricated into the crystal, adding an extra grating vector for compensation of phase mismatch. This allows to access the d_{33} coefficient of the LN crystal (∼16 pm/V), almost three times lager than that of a bulk LN crystal. This key improvement in conversion efficiency has enabled a multitude of new applications using these periodically poled lithium niobate (PPLN) crystals.

Høgstedt *et al.* [19] presented an upconversion module used to monitor atmospheric CO_2 concentrations in a differential absorption LIDAR measurement for the first time. The pulsed signals at 1572 nm are upconverted to 635 nm using a PPLN crystal and detected by a silicon photomultiplier tube. Dam *et al.* [20] developed a compact image upconversion device which can be easily attached to regular silicon cameras. A candle was used as a mid-IR illumination source mixed with 1064 nm pump light inside a PPLN crystal for mid-IR spectral imaging. PPLN based devices enables the conversion from 2.85 µm to 5 µm radiation to the ∼800 nm range by appropriate choice of poling structure and fine tuning using the crystal temperature for phase matching. Temporão *et al.* [21] developed a single-photon counter based on a PPLN nonlinear crystal to convert 4.65 µm radiation in 809 nm for infrared detection using a silicon avalanche photodiode detector (Si-APD). Although PPLN has beneficial properties for nonlinear optics, such as a large nonlinear coefficient of d_{eff}≈16 pm/V, it cannot be used beyond 5 µm due to high absorption at longer wavelengths.

Moving to longer wavelengths, the availability of appropriate nonlinear crystals with high nonlinearity, high transmission in the LWIR and simultaneously at the upconverted wavelength range combined with the ability to phase-match the nonlinear process is very limited. Thus, little has been published on upconversion beyond a 5 µm. In this region, $AgGaS_2$ is a promising nonlinear material of choice for upconversion-based LWIR applications, since it is commercially available, has a fairly high nonlinear coefficient, d_{eff}≈16 pm/V, and can be phase-matched over a broad range of wavelengths in the LWIR range when mixing with lasers in the 1 µm range. Tidemand-Lichtenberge *et al.* [4] extended upconversion spectroscopy into a wavelength range of up to 10 µm using an $AgGaS_2$ nonlinear crystal, in which IR emission from a Globar source is mixed with 1064 nm laser light for sum-frequency generation (SFG). This enables the device to probe absorption bands of a large number of gases as well as vibrational spectra for biomedical applications. In 2005 Karstad *et al.* demonstrated upconversion detection for free-space communication at 9.3 µm using sum-frequency generation of a LWIR QCL source and a 980 nm diode laser using $AgGaS_2$ as the nonlinear material [22]. Moreover, Zondy *et al.* demonstrated LWIR generation by difference-frequency mixing of 778 nm to 843 nm using $AgGaS_2$ [23]. Despite the experimental success, numerical simulations have not been very accurate so far in terms of power conversion efficiency considering parametric frequency conversion of focused LWIR Gaussian beams in $AgGaS_2$. Although $AgGaS_2$ has relatively low absorption loss below 8 µm, this is no longer the case in the 10 µm to 12 µm range, since at these wavelengths absorption and diffraction become increasingly important to be included for accurate modeling.

In this study, we develop a LWIR upconversion detector combining a solid-state pump laser at 1064 nm and an $AgGaS_2$ crystal to convert 9.4-12 µm infrared radiation emitted from a QCL into the NIR range. We derive a theoretical model and characterize the upconversion detector experimentally obtaining good agreement between theory and experimental data gaining improved understanding of the LWIR upconversion enabling system performance optimization in terms of efficiency and acceptance parameters. This system is then combined with a home-built microscope imaging system for biomedical applications. This upconversion microscopic imaging system is used to probe the chemical composition of breast cancer microcalcifications, with the aim of assessing disease progression. We then compare the results obtained using the upconversion microscopic imaging system with a commercial FTIR system.

1.2 Overview of this dissertation

After presenting the motivation of the work, which is providing an alternative scheme to IR detection based on parametric frequency conversion techniques, we introduce the theory of nonlinear optical frequency conversion based on the plane-wave approximation in chapter 2. This discussion is followed by an integral approach in which we consider interacting waves as focused Gaussian beams, taking into account diffraction effects, absorption and the angular dependence of the refractive index. The influence of beam diffraction and LWIR absorption in the nonlinear material is studied experimentally and theoretically. In chapter 3, we compare the integral approach with the plane-wave approximation in terms of acceptance bandwidth and conversion efficiency and show the importance of including the angular dependence of the refractive index for the upconverted signal when strong focusing is employed. This is very important in order to get good agreement between theoretical predictions and experimental results in the LWIR range. In chapter 4, we present a novel upconversion microscopic imaging system used to detect breast cancer microcalcifications. This system consists of the LWIR upconversion detector presented in chapter 3, a QCL, and a home-built microscope unit using a raster scanning approach. We analyze hydroxyapatite (HAP) powders and a ductal carcinoma *in situ* (*DCIS*) breast cancer biopsy for the spatial distribution and endogenous spectral features of the samples and compare the results with a commercial FTIR system. In chapter 5, we present a preliminary study of a self-referecing system with the purpose of noise reduction for the LWIR detection. We split the LWIR beam into two parts and use one of them as the common-mode signal (reference) to suppress the noise from the other (signal), which passes through the target under test and contains the infor-

mation about the sample. The thesis is concluded in chapter 6 with a summary and a discussion of future work.

Chapter 2

Theoretical background and fundamentals

In this chapter, we briefly introduce the theory of nonlinear parametric processes based on the plane-wave approximation followed by the integral theory in which absorption, beam diffraction, and walk-off were taken into account for a three-wave-mixing process in the LWIR range. These parameters are critical to be considered when moving to longer infrared wavelengths in order to appropriately operate the LWIR upconversion detector in real-world applications. The performance of the LWIR upconversion detector was experimentally evaluated in terms of efficiency, spectral coverage of the frequency upconversion, acceptance parameters and LWIR pulse measurements using silicon detectors. The experimental results were compared with the simulation results using both the plane-wave approximation and the integral approach. This shows how LWIR beam diffraction in connection with the birefringent nature of the nonlinear material influences the performance of upconverted signals in nonlinear parametric processes.

2.1 Historical overview

$AgGaS_2$ is a promising material for LWIR upconversion because of its broad transparency range up to 12 µm, large nonlinear coefficient of d_{eff} ≈16 pm/V and being commercially available. Researchers had demonstrated theoretically and experimentally frequency up- and down-conversion for LWIR detection and generation using $AgGaS_2$ crystals as the nonlinear medium. CO_2 lasers have been widely used as LWIR sources to study frequency conversion: however, most of these lasers can only operate at a single wavelength [24–26]. After tremendous technological progress in the past decades, quantum cascade lasers (QCLs) appear ideal for many IR applications due to their compact size and broadly tunable wavelength range with fast tuning speed. Karstad *et al.* [22] studied the upconversion process as a potential ap-

plication for free space communication, at a LWIR wavelength of 9.3 µm. Note that the $AgGaS_2$ nonlinear material is still relatively transparent at this wavelength, but this is no longer the case for the wavelength range from 10 µm to 12 µm [27]. The presented measured conversion efficiency of that study, was off by a factor of 50 compared to their theoretically predicted efficiency. The difference between experimental and theoretical efficiency may be due to limitations in their model. Zondy *et al.* [28] measured a conversion efficiency for difference-frequency generation (DFG) of $\sim$1 µW/W^2 when generating 10.2 µm radiation by mixing 778 nm and 843 nm light. The DFG efficiency is approximately 30 % smaller than their theoretically calculated efficiency. In particular, they neglected absorption. Generally, the numerical simulations presented so far have been not very accurate in predicting the power conversion efficiency, which limits their usefulness in the LWIR range. Here, we develop a more detailed theoretical model and extend the applicability of upconversion toward spectroscopy, using a broadly tunable, narrow linewidth QCL source in the LWIR range. At long infrared wavelengths in the 10 µm to 12 µm range, absorption and diffraction in $AgGaS_2$ are no longer negligible and must be included in the model for accurate predictions. Therefore, in the simulation we take into account, the beam sizes, powers and wavelengths of the pump light, LWIR radiation and upconverted signal, respectively, as well as the effective crystal length, beam diffraction, walk-off, absorption and transverse momentum. This provides a more accurate estimation of the conversion efficiency for the optimization of the upconversion system.

2.2 Sum-frequency generation

2.2.1 Plane-wave approximation

Classical electromagnetic wave theory is used to describe nonlinear optical phenomena, in particular the interaction between electromagnetic fields and matter, which consequently induces a radiation response at different frequencies in $\chi^{(2)}$ nonlinear media. Generally, the common approach to parametric frequency generation in a three-wave mixing process is to solve three coupled differential wave equations. This is extensively discussed in textbooks on nonlinear optics [29, 30], therefore only an abbreviated description of this standard approach is shown here. In this chapter, we focus on sum-frequency generation (SFG) as a result of three-wave interaction. In the SFG process, two incident waves, labeled as pump and IR signal, respectively, interact with a nonlinear $\chi^{(2)}$ medium, creating a new wave at the frequency ω_3 corresponding to the sum of the two incident frequencies, $\omega_3 = \omega_1 + \omega_2$, which is shown schematically in Fig. 2.1

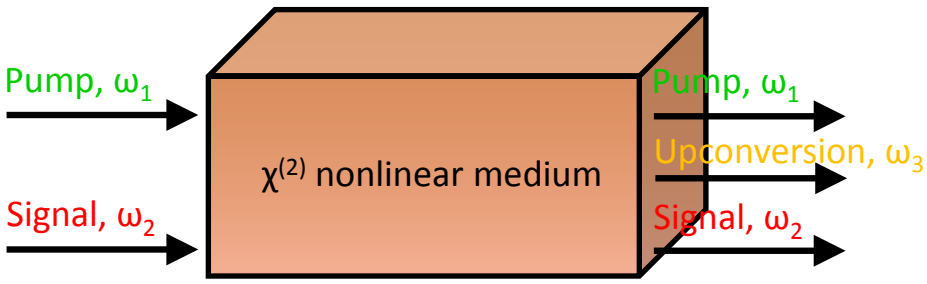

Figure 2.1: Schematic diagram of sum-frequency generation in a $\chi^{(2)}$ nonlinear medium. An IR signal at ω_2 is frequency-upconverted to ω_3 via the nonlinear interaction with the pump at ω_1.

We start from the maxwell's equations given by

$$\nabla \times \boldsymbol{E} = -\frac{\partial \boldsymbol{B}}{\partial t} \tag{2.1a}$$

$$\nabla \times \boldsymbol{H} = \boldsymbol{J} + \frac{\partial \boldsymbol{D}}{\partial t} \tag{2.1b}$$

$$\nabla \cdot \boldsymbol{D} = \rho \tag{2.1c}$$

$$\nabla \cdot \boldsymbol{B} = 0 \tag{2.1d}$$

where $\boldsymbol{E}$ and $\boldsymbol{H}$ are electric and magnetic fields, respectively, $\boldsymbol{B}$ is the magnetic flux density, and $\boldsymbol{D}$ is the electric displacement field, $\boldsymbol{J}$ is the free current density, and ρ is the charge density. $\boldsymbol{D}$ and nonlinear polarization $\boldsymbol{P_{NL}}$, are given by

$$\boldsymbol{D} = \epsilon_0 \epsilon_r \boldsymbol{E} + \boldsymbol{P_{NL}} \tag{2.2a}$$

$$\boldsymbol{P_{NL}} = \epsilon_0 \boldsymbol{\chi^{(2)}} \boldsymbol{E}\boldsymbol{E} \tag{2.2b}$$

where ϵ_0 is a vacuum permittivity and $\epsilon_r = 1 + \chi^{(1)} = n^2$ is the relative permittivity, n being the refrective index. $\chi^{(1)}$ and $\chi^{(2)} = 2\boldsymbol{d}$ ($\boldsymbol{d}$ is nonlinear coefficient as a function of position) are linear and nonlinear susceptibilities of the nonlinear medium, respectively. Here, we only consider the $\chi^{(2)}$ nonlinear process. Taking the curl of Eqn (2.1a) and using Eqn (2.1b), we obtain

$$\nabla^2 \boldsymbol{E} - \mu_0 \sigma \frac{\partial \boldsymbol{E}}{\partial t} - \mu_0 \epsilon \frac{\partial^2 \boldsymbol{E}}{\partial^2 t} = \mu_0 \frac{\partial^2 \boldsymbol{P}_{NL}}{\partial^2 t} \tag{2.3}$$

assuming $\rho = 0$ in an electrically neutral medium. Here, σ is the electric conductivity as a second order tensor in an anisotropic medium, but it is assumed as a scalar. σ is related to absorption coefficient, $\alpha = \mu_0 \sigma c/n$, where c is the speed of light, n is refractive index , and μ_0 is the permeability of free space. P_{NL} can be expressed as a scalar with two incident electric fields

$$P_{NL} = 2\epsilon_0 d_{eff} EE \tag{2.4}$$

where d_{eff} is the effective nonlinear coefficient contracted from a tensor ($\boldsymbol{d}$) to a scalar and can be found in terms of the polarization states of the interacting fields and geometry of the nonlinear medium regarding to crystal class. We introduce a variable $a_{\omega i}$ defined as the square root of the photon flux $\phi_{\omega_i} = \frac{I\omega_i}{\hbar\omega_i} = \frac{|E|^2}{2\eta\hbar\omega_i}$ at the frequency ω_i to simplify the equations Eqn (2.5). $\eta = \sqrt{\mu/\epsilon}$ is the impedance of the material and $\hbar = h/\pi$ is Planck's constant. Inserting a harmonic plane-wave electric field of the form $E(t) = A\exp\{-i(wt + kz)\} + c.c.$ along the z axis with A the amplitude, ω the angular frequency, $k = 2\pi/\lambda$ the wave vector and c. c. denoting complex conjugation, and using the slowly varying envelope approximation (i.e. the amplitude of $E(t)$ changes much slower than the phase of E), we obtain the following coupled differential wave equations:

$$\left(\frac{d}{dz} + \frac{\alpha_1}{2}\right) a_{\omega_1} = -\, iga_{\omega_3} a^*_{\omega_2} e^{-i\Delta kz} \tag{2.5a}$$

$$\left(\frac{d}{dz} + \frac{\alpha_2}{2}\right) a_{\omega_2} = -\, iga_{\omega_3} a^*_{\omega_1} e^{-i\Delta kz} \tag{2.5b}$$

$$\left(\frac{d}{dz} + \frac{\alpha_3}{2}\right) a_{\omega_3} = -\, iga_{\omega_1} a_{\omega_2} e^{i\Delta kz} \tag{2.5c}$$

where α_j are power loss coefficients with the indices 1,2,3 referring to the infrared, pump and upconverted signals, respectively. Δk is the phase mismatch between the three interacting waves, and g is the gain parameter given by $2\epsilon_0 d_{eff}$ $\sqrt{\frac{1}{2}\eta^3\hbar\omega_1\omega_2\omega_3}$. Fig. 2.2 shows the configurations of collinear and non-collinear phase-matching. In this work, collinear phase matching is used in chapter 3 and chapter 4 due to the better spatial overlap of two fundamental beams, leading to better up-conversion efficiency.

In general, the pump field is much stronger than the infrared field in SFG, therefore several assumptions were made in order to analytically solve the coupled differential wave equations, Eqn (2.5). We first assumed $a_{\omega_2}(\mathrm{z}) = a_{\omega_2}(0)$ i.e. non-depletion of the pump. Secondly, we consider perfect phase matching, in which $\Delta k = 0$. This can be achieved using phase matching techniques, such as birefringent phase match-

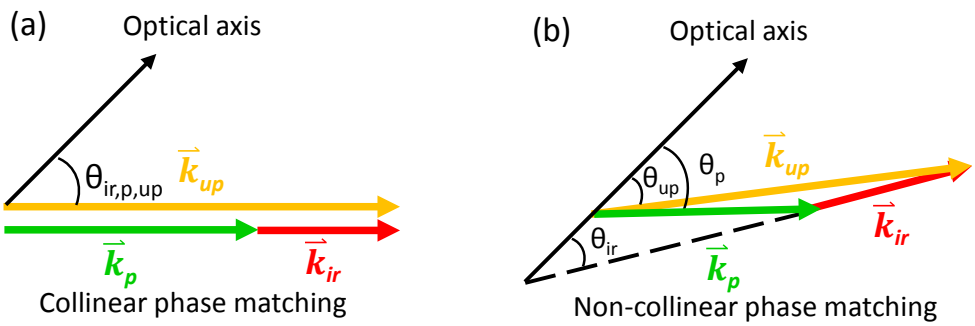

Figure 2.2: Schematic diagrams of collinear (a) and non-collinear (b) phase-matching geometries. θ_{ir}, p, up are the angles between momentum vectors of the IR, pump, and upconverted signals, respectively, and the optical axis of the nonlinear crystal.

ing or quasi phase matching (QPM). The absorption loss of the $AgGaS_2$ crystal used in this work is significant above 10 µm (see Fig. 3.3) and therefore must be taken into account for accurate modeling around and above the 10 µm range. Using the boundary conditions, $a_{\omega_2}(z) = a_{\omega_2}(0)$ for non-depletion of the pump and $a_{\omega_3}(0) = 0$, i.e. no upconverted signal the input of the nonlinear crystal, we obtain the solutions

$$\phi_{\omega_1}(z) = \phi_{\omega_1}(0)\cos^2(g a_{\omega_2}(0) z) \tag{2.6a}$$

$$\phi_{\omega_3}(z) = \phi_{\omega_1}(0)\sin^2(g a_{\omega_2}(0) z) \tag{2.6b}$$

We see that a conversion of energy occurs from the pump at ω_1 to the upconverted signal at ω_3. Considering the weak coupling between the interacting fields where ϕ_{ω_1} and ϕ_{ω_2} are assumed not depleted. Based on this assumption, using first-order Taylor expansion of the trigonometric function and substituting $\phi_{\omega_i} = \frac{I\omega_i}{\hbar\omega_i}$ into Eqn (2.6), the conversion efficiency (CE) of sum-frequency mixing results as

$$CE = \frac{I_{\omega_3}(z)}{I_{\omega_1}(0)} = \frac{1}{2}\eta^3\omega_3^2(\epsilon_0\chi^{(2)}_{eff})^2 I_{\omega_2}(0)L^2 \tag{2.7}$$

Typically, Eqn (2.6) is used to quantify the performance of upconversion systems in parametric frequency conversion, which is critical for the applications presented in this work. However, the solutions derived from this simple plane-wave approximation are insufficient for accurate estimation of the parameters relevant to the performance of these systems, i.e. the conversion efficiency for LWIR signals. This is because beam diffraction is not taken into account. We therefore extended the theoretical model

of nonlinear frequency conversion to include LWIR beam diffraction, considering interacting waves as Gaussian beams. The simulation data are compared with the experimental result in the following sections.

2.2.2 Integral approach

Here, we present a theoretical treatment in which beam diffraction, walk-off (effective crystal length), absorption, and angular dependent refractive index which is eliminated in Boyd-Kleinmann approach [31], are taken into account in parametric conversion process, where the interacting waves are considered as Gaussian beams. The integral approach is based on the far-field solution of the electromagnetic wave equation, integrating the electromagnetic fields radiated from all sources in a nonlinear medium. Note that we assumed that both pump and LWIR powers are not depleted in this case (small-signal approximation).

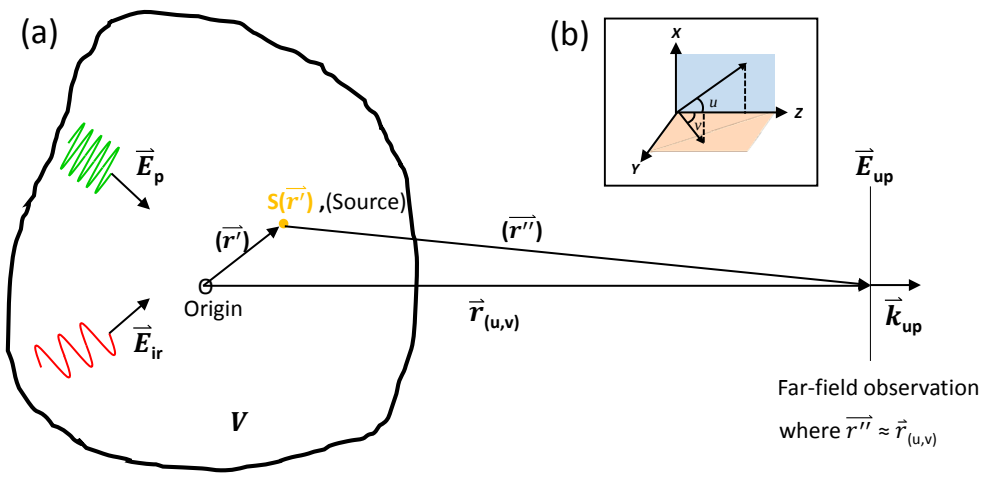

Figure 2.3: (a) Schematic layout of sum-frequency generation (SFG). Two input fields, pump ($\boldsymbol{E_p}$) and infrared ($\boldsymbol{E_{ir}}$) are interacted with a $\chi^{(2)}$ nonlinear medium, generating a new frequency component ($\boldsymbol{E_{up}}$). (b) coordinate system used (for more detail, see Fig. 2.5).

In the SFG process, a LWIR signal at ω_{ir} is combined with a pump field at ω_p to produce an upconverted signal at ω_{up}. The LWIR and the mixing fields are treated as Gaussian electromagnetic beams with finite beam sizes. The layout and coordinate system of the upconversion scheme is depicted in Fig. 2.3. Using the integral approach, the upconverted electric field (E_{up}) in the direction given by the angles (u, v) at a distance, $r_{uv} = |\boldsymbol{r_{uv}}|$, between the source point and the far field observation point can be expressed by [29, 32, 33].

$$E_{up}(r_{uv}, \boldsymbol{k_{up}}) \equiv \frac{\exp(-ik_{up}r_{uv})}{4\pi r_{uv}} \int_V S_{up}(\boldsymbol{r'}) \exp(i\boldsymbol{k_{up}} \cdot \boldsymbol{r'}) dr' \tag{2.8}$$

where V is the volume of the nonlinear material and $\boldsymbol{k_{up}}$ is the wave vector of the upconverted electric field parallel to $\boldsymbol{r_{uv}}$, see Fig. 2.3. The source term, $S_{up}(\boldsymbol{r'})$ in $\chi^{(2)}$ nonlinear process is given by

$$S_{up}(\boldsymbol{r'}) = -\mu_0 \frac{\partial^2 P_{up}}{\partial^2 t} = \frac{2d_{eff}\omega_{up}^2}{c^2} E_p(\boldsymbol{r'}) E_{ir}(\boldsymbol{r'}) e^{-i(\boldsymbol{k_{ir}}+\boldsymbol{k_p})\cdot \boldsymbol{r'}} \tag{2.9}$$

where P_{up} is the polarization density of the upconverted field, given by

$$P_{up} = 2\epsilon_0 d_{eff} E_p(\boldsymbol{r'}) E_{ir}(\boldsymbol{r'}) e^{-i(\boldsymbol{k_{ir}}+\boldsymbol{k_p})\cdot \boldsymbol{r'}} e^{i(\omega_{ir}+\omega_p)t} \tag{2.10}$$

where the angular frequency of the upconverted signal $\omega_{up} = \omega_{ir} + \omega_p$, $E_p(\boldsymbol{r'})$ and $E_{ir}(\boldsymbol{r'})$ are the electric fields of the pump (p) and IR (ir) signals, respectively. $E_p(\boldsymbol{r'})$ and $E_{ir}(\boldsymbol{r'})$ are given by

$$E_p(\boldsymbol{r'}) \exp(-ik_{pz}z) = \frac{E_p}{1 + i\frac{z}{z_{Rp}}} \exp(-ik_{pz}z) \exp\{-\frac{u^2 + v^2}{W_p^2(1 + i\frac{z}{z_{Rp}})}\} \tag{2.11}$$

$$E_{ir}(\boldsymbol{r'}) \exp(-ik_{irz}z) = \frac{E_{ir}}{1 + i\frac{z}{z_{Rir}}} \exp(-ik_{irz}z) \exp\{-\frac{u^2 + v^2}{W_{ir}^2(1 + i\frac{z}{z_{Rir}})}\} \tag{2.12}$$

where $k_{(p,ir)z}$ are the wave vectors of the LWIR and the upconverted waves, respectively, propagating in the z direction (see Fig. 2.4). u describes the propagation angle of the fields relative to the z-direction in the plane of the optical axis (extraordinary plane) and v is the angle in the perpendicular direction (ordinary plane) relative to the z-direction, see Fig. 2.5. E_p and E_{ir} are the amplitudes of the electric fields, W_p and W_{ir} are the beam waists, and z_{R_p} and $z_{R_{ir}}$ are the Rayleigh range of the pump and infrared electric field, respectively, given by $z_{R(p,ir)} = k_{(p,ir)}\mathrm{W}_{(p,ir)}^2/2$. Inserting Eqn (2.9), Eqn (2.11), and Eqn (2.12) into Eqn (2.8), the upconverted field results as

$$E_{up}(u,v,r_{uv}) = \frac{4d_{eff}\pi^2}{c\epsilon_0\lambda_{up}^2}\sqrt{\frac{2P_{ir}}{n_{ir}\pi W_{ir}^2}}\sqrt{\frac{2P_p}{n_p\pi W_p^2}}\frac{e^{-i\boldsymbol{k_{up}}\cdot\boldsymbol{r_{uv}}}}{r_{uv}}\int_{-\frac{l}{2}}^{\frac{l}{2}}\frac{W_{ir}^2W_p^2}{W_{ir}^2+W_p^2+i\frac{\lambda_{ir}z}{\pi n_{ir}}+i\frac{\lambda_p z}{\pi n_p}}\times$$

$$\exp\left\{-\frac{1}{4}\left(\frac{(W_{ir}^2+i\frac{\lambda_{ir}z}{\pi n_{ir}})(W_p^2+i\frac{\lambda_p z}{\pi n_p})}{W_{ir}^2+W_p^2+i\frac{\lambda_{ir}z}{\pi n_{ir}}+i\frac{\lambda_p z}{\pi n_p}}\right)(\Delta k_u^2+\Delta k_v^2)\right\}\exp\left\{-\frac{\alpha_{ir}}{2}\left(z+\frac{l}{2}\right)\right\}e^{i\Delta k_z z}dz \tag{2.13}$$

where α_{ir} is the field absorption coefficient for the LWIR radiation, l is the length of the nonlinear crystal, $r_{(u,v)}$ is the distance from the source to the far field observation point, n_p and n_{ir} are the refractive indices of the nonlinear crystal at the pump and LWIR frequency, respectively. Δk_u and Δk_v denote the transverse phase-mismatch in the u and v directions, respectively, and Δk_z is the longitudinal phase mismatch along the z direction. Note that it is essential to take the transverse phase-mismatch into account if the LWIR beam is tightly focused, i.e. Rayleigh range is short compared to the crystal length. This is usually ignored in calculations of using plane-wave approximation. The phase-mismatch term Δk can be calculated according to the Sellmeier equations [34, 35] for the the nonlinear material for the propagation directions of the interacting fields. Δk is separated into a longitudinal, Δk_z and a transverse Δk_T contribution, shown in Fig. 2.4.

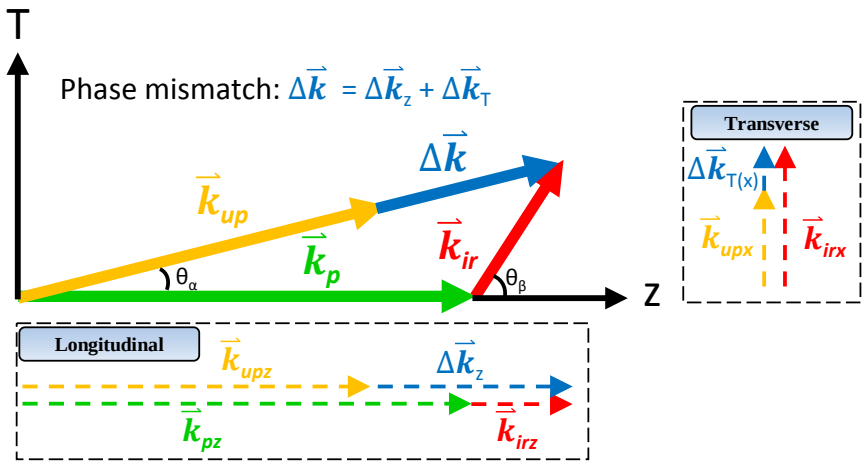

Figure 2.4: An example of phase mismatch, showing the geometric relations between the wave vectors of the three interacting fields. Δk is decomposed into longitudinal and transverse terms (Δk_z, Δk_T), in which the which the labels Z and T correspond to the axes of the coordinate system as shown in the graph.

Δk_z and Δk_T are given by

$$\Delta k_z = 2\pi \left(\frac{n_{e_{up}}(\theta_{up}, \lambda_{up})}{\lambda_{up}} \cdot \cos(\rho_{up}) - \frac{n_{o_p}(\theta_p, \lambda_p)}{\lambda_{ir}} - \frac{n_{e_{ir}}(\theta_{ir}, \lambda_{ir})}{\lambda_{ir}} \cdot \cos(\rho_{ir}) \right) \tag{2.14a}$$

$$\Delta k_T = 2\pi \left(\frac{n_{e_{up}}(\theta_{up}, \lambda_{up})}{\lambda_{up}} \cdot \sin(\rho_{up}) - \frac{n_{e_{ir}}(\theta_{ir}, \lambda_{ir})}{\lambda_{ir}} \cdot \sin(\rho_{ir}) \right) \tag{2.14b}$$

where n_{o_i} and n_{e_i} denote the ordinary (o) and extraordinary (e) refractive index of the nonlinear material, ρ_i is the angle between k_i and the z axis in the nonlinear crystal. θ_i is the angle between k_i and the optical axis of the crystal, where "i" indicates the LWIR (ir), pump (p) and upconverted (up) field, respectively. Fig. 2.5 shows the schematic geometry of the coordinate system and parameters used in Eqn (2.14a) and Eqn (2.14b) for the calculation of the phase mismatch term, $\Delta \boldsymbol{k} = \Delta \boldsymbol{k_z} + \Delta \boldsymbol{k_T}$. The pump field is considered to propagate along the z-direction.

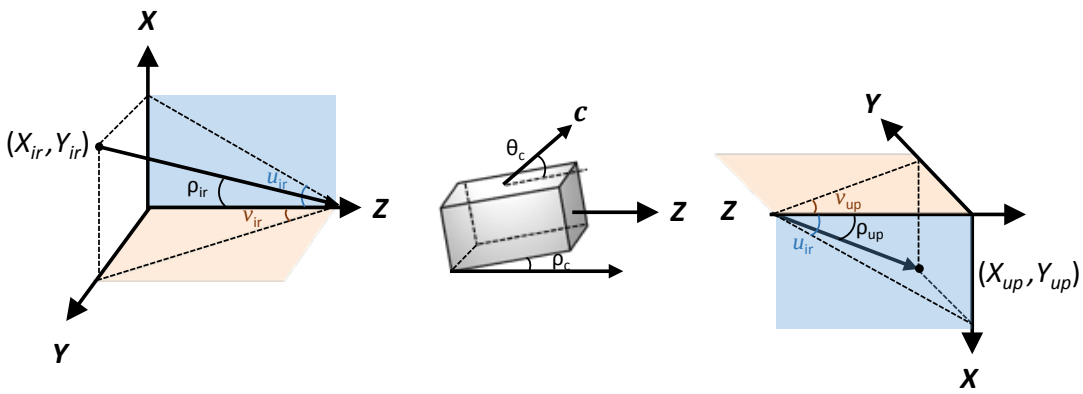

Figure 2.5: Schematic layout of the coordinate system, illustrating the parameters defined for the theoretical calculations. u_i and v_i are the internal angles between wave vectors projected to the *X-Z* and *Y-Z* planes ,respectively. The *X-Z* plane is parallel to the optical axis, $\boldsymbol{c}$. ρ_c is the crystal rotation angle and θ_c is the cutting angle of the crystal.

ρ_i (i indicates ir, pump, upconversion) describes the internal angles inside the nonlinear crystal, given by

$$\cos(\rho_i) = \frac{1}{\sqrt{\tan^2(u_i) + \tan^2(v_i) + 1}} \tag{2.15}$$

The extraordinary index of refraction depends on the angle of the propagating waves relative to the optical axis, and is given by

$$\frac{1}{n_e^2(\theta_i, \lambda_i)} = \frac{\sin^2(\theta_i)}{n_e^2(\lambda_i)} + \frac{\cos^2(\theta_i)}{n_e^2(\lambda_i)} \tag{2.16}$$

where λ_i denote the wavelength of the electromagnetic fields and θ_i is given by

$$\theta_i = \cos^{-1}\left(\frac{\cos(\theta_c + u_i + \rho c^*)\cos(v_i)}{\sqrt{\cos^2(v_i) + \cos^2(u_i)\sin^2(v_i)}}\right) \tag{2.17}$$

θ_c is the cutting angle of the nonlinear crystal. ρc^* is the internal refracted angle of the incident pump beam (inside the nonlinear crystal) to the normal plane of the nonlinear crystal's surface, given by

$$\rho c^* = \sin^{-1}\left(\frac{\sin u^{ex} - \rho c}{n_o(\lambda_p)}\right) \tag{2.18}$$

where u^{ex} is the external angle of the incident pump beam to the normal incidence of the nonlinear crystal in u plane and $n_o(\lambda p)$ is the refractive index at the pump wavelength (λ_p). ρc^* indicates how the rotation of the nonlinear crystal and an externally angled pump beam affects the internal propagating angles. The total upconverted power, P_{up} is obtained by integrating the absolute square of the upconverted field E_{up} shown in Eqn (2.13) with respect to u and v directions:

$$P_{up} = \frac{c\epsilon_0 n_{up}}{2}\int_u\int_v |E_{up}(u, v, r_{uv})|^2 r_{uv}^2 du dv \tag{2.19}$$

Note that the refractive index n_{up} as well as the phase-mismatch Δk depend on the directions, u and v.

Chapter 3

LWIR upconversion detector

3.1 The LWIR upconversion detector

The upconversion setup is illustrated in Fig. 3.1. The pump source is a diode-pumped 1064 nm Nd:YVO_4 laser in continuous-wave operation, delivering up to 3 W of output power, see Fig. 3.2. A laser diode at the wavelength of 808 nm is used to pump the 3 mm × 3 mm × 10 mm Nd:YVO_4 laser crystal, coated by anti-reflection (for 1064 µm and 808 µm) on both ends, within a 3.5 cm long cavity, achieving 50 % slope efficiency. The diode-pumped solid state laser provides a pump beam with a good spatial mode and narrow spectral linewidth. When mixing a pump field at 1064 nm and a LWIR field of 9.4 µm to 12 µm using an $AgGaS_2$ crystal, we obtain upconverted radiation within a wavelength range of ∼956 nm to 977 nm, at which the $AgGaS_2$ crystal is highly transparent. Note that a master oscillator power amplifier (MOPA) could alternatively be used as the pump source for the upconversion. MOPA is a semiconductor laser in continuous-wave operation, tunable from 973.7 nm to 983.4 nm with 5.5 W output power [36], which device (from one of our ITN partners) had been preliminarily tested. One of the advantages of using this laser is to be able to move the upconverted wavelength to the shorter wavelength region of e.g. ∼882 nm to 900 nm (when converting the LWIR from 9.4 µm to 12 µm) in which wavelength region silicon-based detectors have better quantum efficiency, compared to using the 1064 µm solid state pump laser.

The astigmatic output beam emitted from the QCL is circularized using two cylindrical ZnSe lenses of focal lengths $f_1 = 25.4$ mm and $f_2 = 50.8$ mm, respectively. A half-wave plate ($\lambda/2$) is used to align the polarization of the LWIR radiation along the extraordinary axis of the nonlinear crystal. Two lenses of focal lengths $f_3 = 50$ mm and $f_4 = 150$ mm are used to focus the QCL and the mixing beam into the nonlinear crystal via a beam combiner. The beam combiner is highly transparent

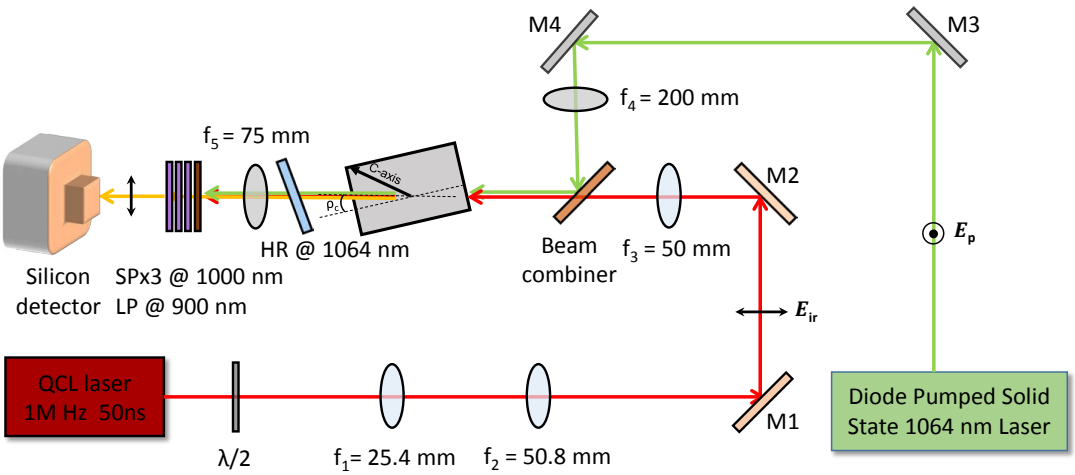

Figure 3.1: Schematic layout of the experimental setup for upconversion detection. $\boldsymbol{E_p}$ is the pump field which is linearly polarized perpendicular to the image plane. $\boldsymbol{E_{ir}}$ is the LWIR field which is linearly polarized along the image plane and parallel to the optical axis of the crystal (C-axis). ρ_c is the crystal's rotation angle.

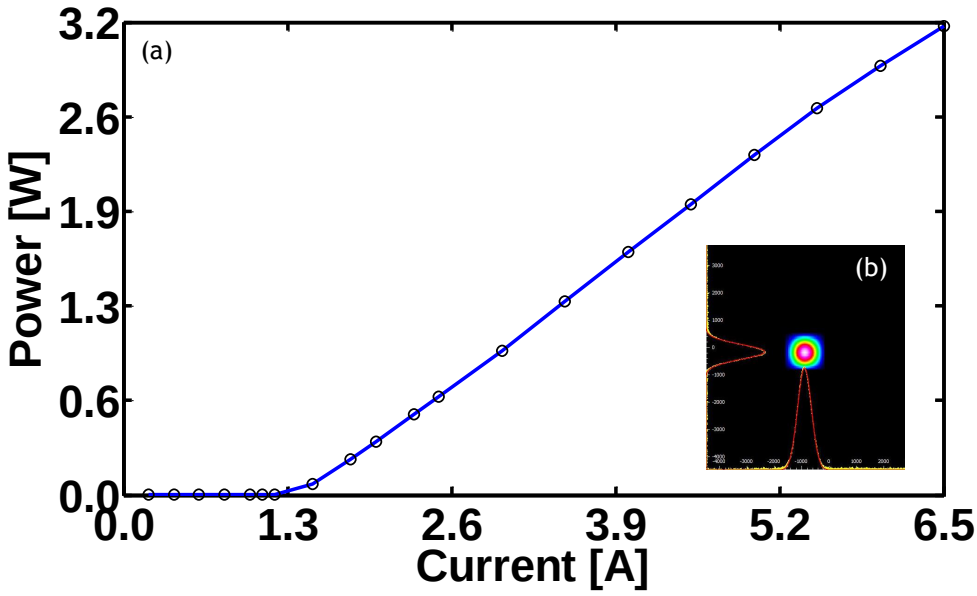

Figure 3.2: (a) Output optical power of the pump source as a function of the operating current of the diode laser. (b) Beam profile of the pump source with the intensity distributions (yellow curves) in both directions fitted with Gaussian (red curves).

at 10.6 µm and highly reflective at 1064 nm, but its transmission loss (up to ∼30 %) varies over the tuning range of the LWIR signal. After passing through the beam combiner, both beams are focused at the center of the nonlinear crystal with a waist radius of ∼100 µm. The spot size of the LWIR beam is characterized using a pinhole with a diameter of ∼200 µm and the optical power is measured before and after the pinhole in order to calculate the beam diameter at the position of the pinhole using Gaussian beam theory.

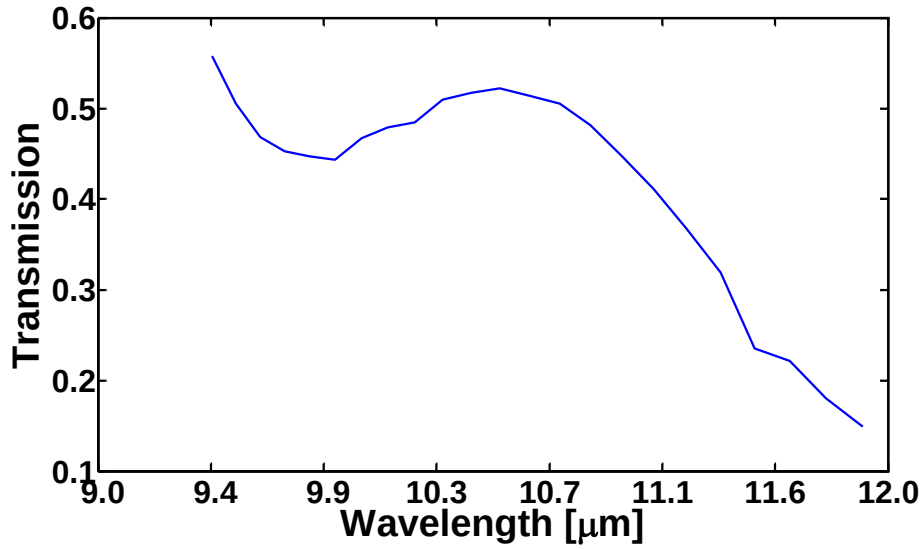

Figure 3.3: Transmission curve of the $AgGaS_2$ nonlinear crystal versus the QCL wavelength

The $AgGaS_2$ crystal was mounted on a piezo controlled rotation stage (ECR3030, Attocube) for angle-tuned birefringent phase-matching, in which the crystal was rotated at each wavelength to find the optimum conversion efficiency. The upconverted signal was collimated with a lens of focal length $f_5 = 75$ mm, filtered using a high-reflective mirror at 1064 nm followed by three short-pass (SP 1000 nm) filters and a long-pass (LP 900 nm) filter, before being detected with a silicon detector. Fig. 3.3 shows the transmission curve of the $AgGaS_2$ crystal, which was calculated as the ratio of the measured power before and after the $AgGaS_2$ crystal, while tuning the wavelength of the QCL. Although $AgGaS_2$ has relatively low absorption loss below 8 µm [27], this is no longer the case in the 9 µm to 12 µm range. It can be seen that the transmission is significantly reduced above 9 µm. Therefore, it is essential to take absorption into account for accurate modeling when using an $AgGaS_2$ crystal for long wavelength upconversion.

3.1.1 LWIR source: quantum cascade laser

A quantum cascade laser (QCL) is a semiconductor laser using inter-subband transitions for radiative emission, which is different from conventional diode lasers, for which the laser frequency is determined by the energy gap between the conduction and valence bands where the radiative transitions occur, see Fig. 3.4. Due to the lack of materials with a bandgap of 0.1 eV to 0.4 eV for LWIR radiation, conventional interband laser diodes are not suitable for LWIR generation. The quantum cascade laser is a unipolar laser, relying on only one type of carrier. Therefore, the optical emission is determined by the heterostructured conduction band (inter-subband). The optical frequency is no longer determined by the bandgap of the material (interband) but by the energy spacing of the subbands. In the inter-subband structure, each electron tunnels through several biased active regions (quantum wells) separated by potential barriers formed by the heterostructure. A photon is emitted after each tunneling process with an energy corresponding to the potential difference between the quantum wells introduced by the external bias. Typically, a QCL is constituted of tens to hundreds of periods (cascading) to improve efficiency by reusing the same electron to generate multiple photons from subsequent tunneling processes.

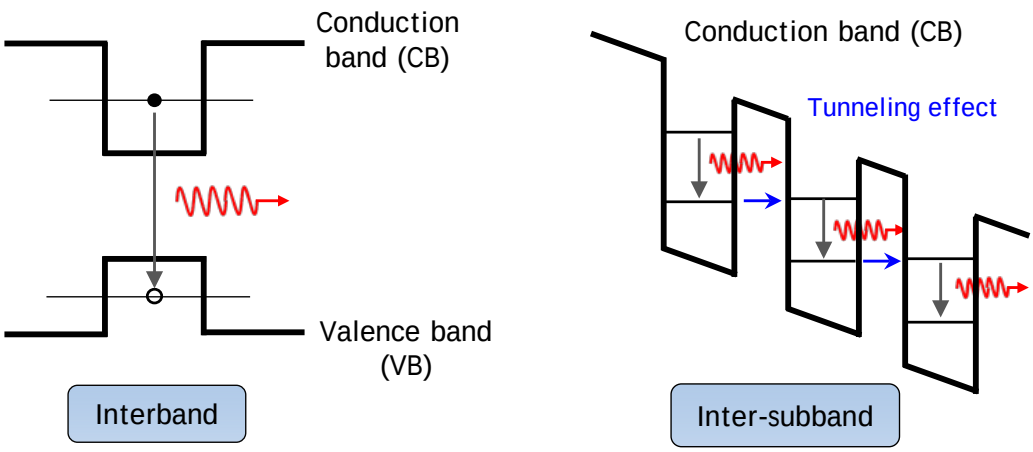

Figure 3.4: Comparison between radiative transitions occurring in a quantum well using interband and inter-subband mechanisms. A QCL is using the inter-subband approach with the transitions taking place between two subbands.

In this work, a quantum cascade laser (Mini-QCL 100, BLOCK engineering) is used as a narrow linewidth LWIR source. The QCL is widely tunable from 9.4 µm to 12 µm and delivers 50 ns-pulses with 1 MHz repetition rate. Fig. 3.5 shows the

normalized spectral output of the QCL at different wavelength settings from 9.35 µm (1070 cm^{-1}) to 11.9 µm (840 cm^{-1}) at ∼120 nm (10 cm^{-1}) intervals. The spectra were measured with a free-space coupled optical spectrum analyzer (OSA207C, Thorlabs). The linewidth of the QCL emission was found to be ∼1 cm^{-1} for all wavelength settings. Fig. 3.6 shows the optical output power of the QCL laser as a function of wavelength. The maximum output power was ∼11.4 mW at the wavelength of 10.4 µm.

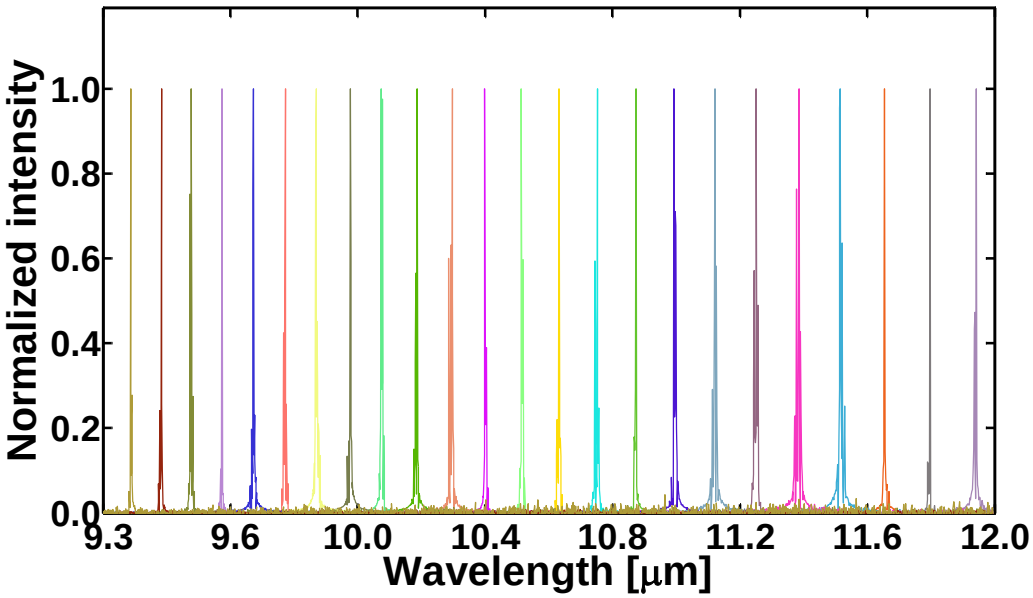

Figure 3.5: Normalized spectral output of the QCL at different wavelengths denoted by different colors.

3.2 Results and discussion

3.2.1 Phase-matching angle tuning

We analyzed the LWIR upconversion detector for the spectral coverage of upconversion using angle-tuned phase matching. Fig. 3.7 shows the angle tuning of the phase-matching condition where the crystal was rotated for each LWIR wavelength for optimal conversion efficiency. LWIR signals in the wavelength range of 9.4 µm to 12 µm were upconverted to the NIR region (from 956 nm to 977 nm) by type II collinear phase-matching. Two fundamental electric fields, extraordinary and ordinary (e-ray and o-ray), with polarization states perpendicular to each other are propagating collinearly inside the nonlinear crystal, as shown in Fig. 2.2(a). Since

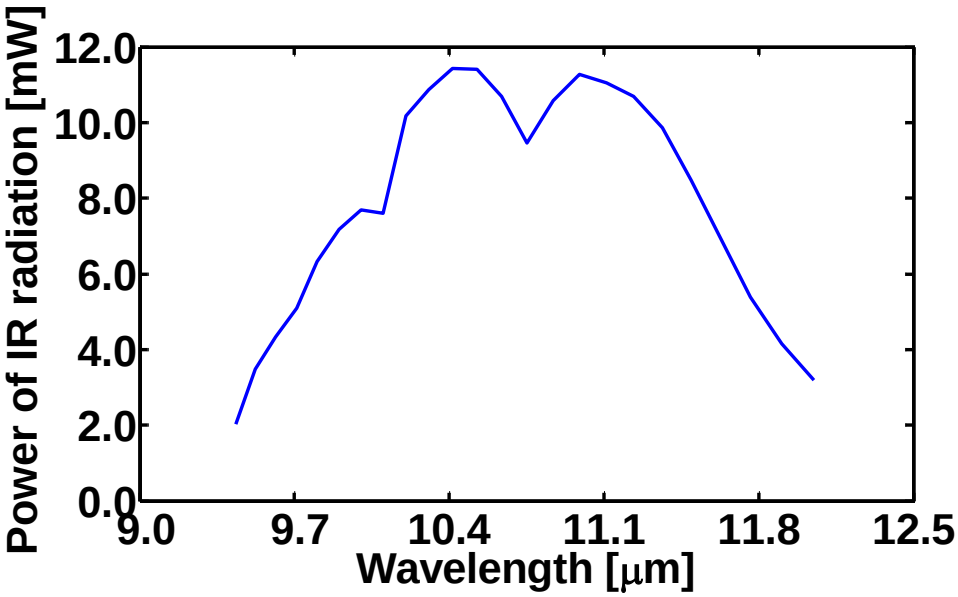

Figure 3.6: Output optical power of the QCL source as a function of wavelength.

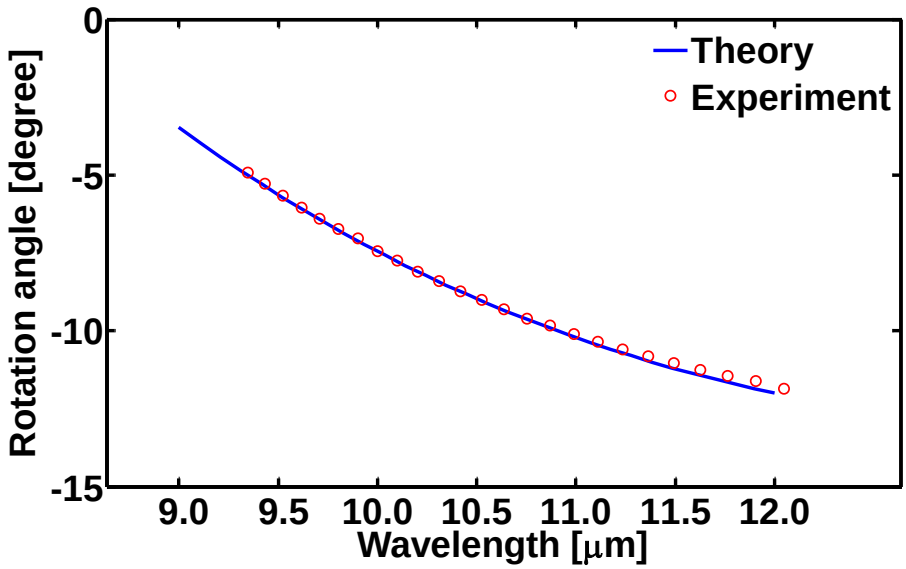

Figure 3.7: Phase-matching angle tuning versus wavelength of long-wave infrared from 9.4 μm to 12 μm at ∼120 nm (10 cm^{-1}) intervals. Blue plot is the theoretical calculation simulated at the temperature of 23°.

the refractive index of the e-ray is wavelength and angle dependent, the phase of the e-ray can be altered by rotating the crystal to fulfill the phase-matching condition for maximum conversion efficiency. For collinear phase-matching, both the LWIR and the pump beams were aligned collinearly, thus the internal angles u_i and v_i (i indicate pump and IR, respectively) were assumed to be 0 in the following calculations for Δk using Eqn (2.17).

The angle of the nonlinear crystal was optimized for optimum phase-matching where we obtained the highest power conversion efficiency of the incident light. The upconverted signal was detected using a silicon detector (S120C, Thorlabs). The blue curve shown in Fig. 3.7 was calculated using the plane-wave approximation based on the Sellmeier equation from references [34, 35]. The red circles indicate the angles where we obtained maximum upconverted power at that wavelength setting of the QCL. It can be seen that the measured phase-matching angles (red circles) show good agreement with the theoretical calculation (blue curve).

3.2.2 Acceptance bandwidth

We investigated the angular and wavelength acceptance bandwidths of the nonlinear frequency conversion process because these parameters limit the conversion efficiency of the upconversion detector setup in real-world applications. Fig. 3.8 shows the measured and the simulated conversion efficiencies as a function of rotation angle of the nonlinear crystal. The graphs have been normalized to account for the different conversion efficiencies obtained for the two different numerical models, plane-wave approximation and integral approach.

The simulated results in Fig. 3.8 were obtained using Eqn (2.7) and Eqn (2.19). The LWIR wavelength was fixed at 10.3 µm and the upconverted signal was measured at each rotation angle of the nonlinear crystal using a silicon detector. The measured full width at half maximum (FWHM) bandwidth is $\sim$0.4°. It is clearly evident that the plane-wave approximation is no longer valid in this wavelength range due to diffraction of the LWIR beam with a beam size of $W_{ir} = W_p = 100\,\mu m$.

The solid and dashed blue lines in Fig. 3.8 represent simulation results using the plane-wave approximation for crystal lengths of 10 mm and 7.7 mm, respectively. In order to account for the walk-off of the extraordinary LWIR beam (e-ray), an effective interaction length of 7.7 mm was found [31] at a walk-off angle of ρ_{ir} $\sim$23 mrad. The solid and dashed red lines in Fig. 3.8 depict simulation results using the integral approach, as described in Eqn (2.13) and Eqn (2.19), for crystal lengths of 10 mm and 7.7 mm, respectively. Gouy phase-shift results in a change of the central angle and wavelength in the acceptance graphs in Fig. 3.8 and Fig. 3.9, shifting the crystal rotation angle by 0.05° or the phase-matched wavelength by 15 nm, respectively.

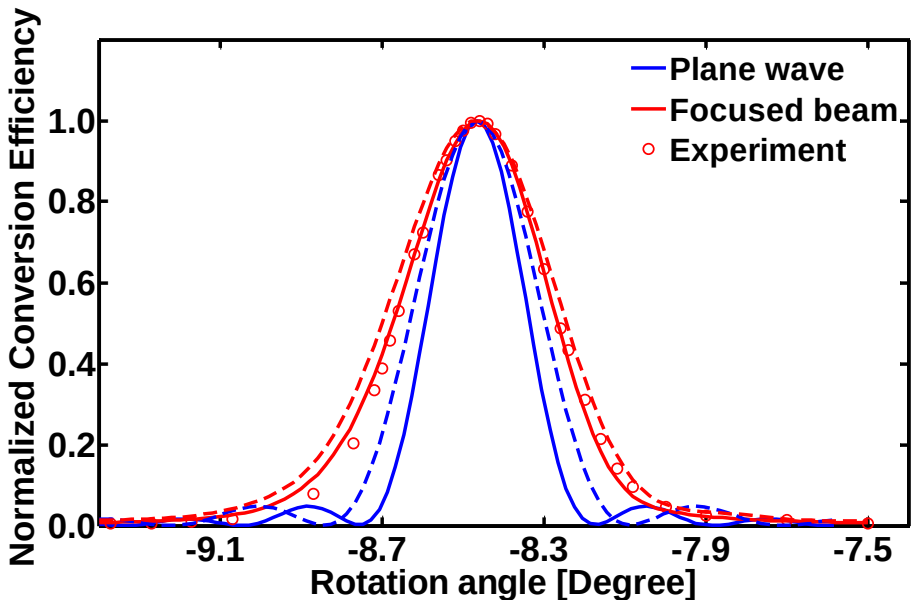

Figure 3.8: Conversion efficiency versus crystal rotation angle at a wavelength of 10.3 µm. To compare the acceptance bandwidth, the angles calculated using plane-wave approximationthe (blue) has been shifted by ∼0.05° to account for the different phase matching condition obtained for two different numerical models, plane-wave approximation and integral approach.

To compare the acceptance bandwidth, the graphs for plane-wave interaction (blue) shown in Fig. 3.8 and Fig. 3.9 have been shifted by ∼0.05° and 15 nm, respectively, to account for the different phase matching condition obtained for two different numerical models, plane-wave approximation and integral approach. The integral approach is seen to be in good agreement with the measured data (red circles). Similar results are shown for the wavelength acceptance bandwidth at a fixed crystal rotation of -8.5°, yielding a FWHM wavelength acceptance bandwidth of ∼120 nm, see Fig. 3.9. Good agreement is found between the measured data and the simulation obtained using the integral approach, while the plane-wave method is inaccurate.

3.2.3 Upconverted intensity distribution

The upconverted intensity distribution is evaluated based on the integral approach using Eqn (2.13), in which the influences of beam diffraction at LWIR wavelengths and the transmission efficiency of the nonlinear material were taken into account. The refractive index of the nonlinear crystal corresponding to the upconverted signal depends on the directions of wave-propagation, generally not taken into account in the traditional Boyd-Kleinmann approach [31]. The v-direction is parallel to the ordinary plane of the nonlinear crystal, therefore the phase of the incident waves

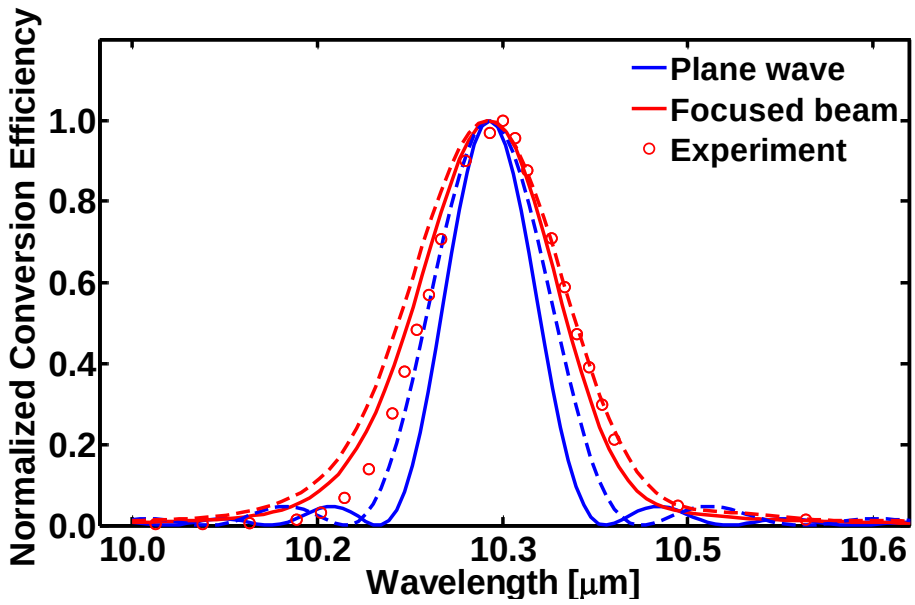

Figure 3.9: Wavelength acceptance bandwidth at -8.5° crystal rotation angle. To compare the acceptance bandwidth, the wavelengths calculated using plane-wave approximationthe (blue) has been shifted by 15 nm to account for the different phase matching condition obtained for two different numerical models, plane-wave approximation and integral approach.

in v-direction is symmetric, resulting in a symmetric intensity distribution. This is due to the diffraction of the LWIR beam and the refractive index of the $AgGaS_2$ leading to a symmetrically Δk along the v plane. However, this is not the case in the u-direction, which is parallel to the extraordinary plane of the nonlinear crystal. The angular dependence of the refractive index breaks the rotational symmetry of the intensity distribution, which is usually observed in upconverted signals. As a result, the upconverted signal becomes elliptical or even breaks up into several lobes due to alternation of constructive and destructive interference due to the superposition of the phases of the upconverted signal (asymmetric Δk distribution in u plane) in the u-direction within the far-field of the upconverted signal.

Fig. 3.10 depicts beam profiles of the upconverted signal acquired with a silicon camera (ueye, IDS), showing both experimental and simulated intensity distributions at wavelengths of 10 µm, 10.3 µm and 10.6 µm, respectively, for three different crystal angles. For each wavelength, the experimental upconverted intensity distributions are shown for crystal rotation angles of $-7.9°$, $-8.8°$ and $-9.6°$, respectively. The simulated upconverted beam profiles are shown for crystal rotation angles of $-7.5°$, $-8.4°$ and $-9.2°$, respectively. The images labeled 'Central' in Fig. 3.10 were measured/simulated at optimum power conversion efficiency. The upconverted power obtained at phase-matched crystal rotation angles is significantly larger than at

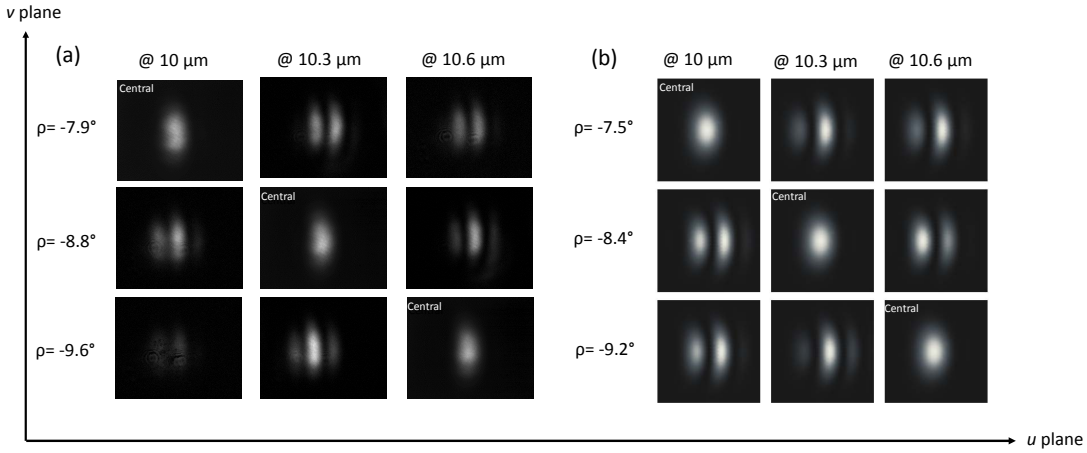

Figure 3.10: beam profiles of the upconverted signal detected with a Si-based camera at crystal rotation angles of $-7.9°$, $-8.8°$ and $-9.6°$ obtained at the wavelengths of 10 µm, 10.3 µm and 10.6 µm, respectively. Images labeled 'Central' denote optimum phase-matching angles. (b) Simulated images of upconverted signal intensities at crystal rotation angles of $-7.5°$, $-8.4°$ and $-9.2°$ at wavelengths of 10 µm, 10.3 µm and 10.6 µm, respectively.

non-optimal phase-matching angles. Therefore, the integration time for the image acquisition was adjusted accordingly in order not to saturate the Si-camera. At a wavelength of 10 µm, integration times of 5 ms, 600 ms and 890 ms were used corresponding to rotation angles of $-7.9°$ (optimum phase-matching angle), $-8.8°$ and $-9.6°$, respectively. The simulated intensities (Fig. 3.10(b)) are normalized to the maximum power found at each simulated crystal rotation angle (ρ) and wavelength. Rotating the crystal angle away from the optimum phase-matching condition results in multi-lobed intensity profiles. This is due to phase differences in upconverted signals along the extraordinary plane (v-direction), resulting in constructive and destructive interference. Fig. 3.10(b) shows the simulated intensity distribution using Eqn (2.13) at 10 µm, 10.3 µm and 10.6 µm, respectively. For maximum conversion efficiency, the crystal rotation was found to be offset by 0.4° compared to the measurements for all images. This is likely due to a systematic error in setting the crystal rotation angles in the experiment. In conclusion, we find good qualitative agreement between the measured intensity distributions of the upconverted beam profiles and the simulated results using Eqn (2.13) and Eqn (2.19).

3.2.4 Conversion efficiency

Fig. 3.11 shows the upconverted power as a function of the LWIR wavelength. The blue line was calculated using the plane-wave approximation with 10 mm interaction length. The wavelength–dependent power from the QCL was used as input, shown

in Fig. 3.6, and the LWIR absorption in the nonlinear crystal was not taken into account. The dotted red line (without crystal absorption) and solid/dashed red lines (with crystal absorption) were simulated using Eqn (2.13) and Eqn (2.19) with interaction lengths of 10 mm and 7.7 mm, respectively. The red circles are experimental data, measuring the upconverted power with a silicon power meter for optimized crystal rotation. The upconverted power was corrected for filter losses. Optimizing the phase mismatch to accommodate for Gouy phase-shift increases the conversion efficiency by ∼3 % compared to $\Delta k = 0$ (optimum for plane-wave interaction).

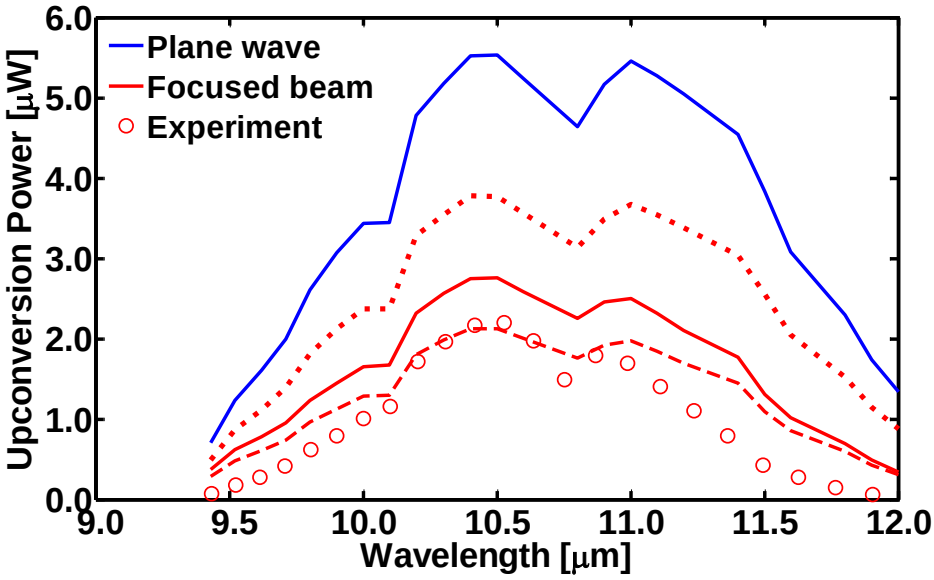

Figure 3.11: Experimental (red circles) and theoretical (lines) upconversion powers using the plane-wave approximation without absorption for 10 mm crystal length (blue line), and a focused infrared beam using the integral method for a crystal length of 10 mm without (dotted red line) and with absorption (solid red line). The dashed red line shows the simulated upconverted power for 7.7 mm crystal length with absorption using the integral method.

The system was aligned at a LWIR wavelength of $\lambda_{ir} = 10.3\,\mu\text{m}$, yielding a maximum measured upconverted power of ∼2.2 µW for a constant mixing power of ∼320 mW at 1064 nm. The $AgGaS_2$ crystal has poor thermal conductivity, thus the pump power was reduced from the available 3 W to 320 mW to minimize thermal effects in the nonlinear medium. As the crystal was rotated for optimum phase matching at the different QCL wavelengths, the refractive index difference for the two fields resulted in a reduced spatial overlap, leading to a decreased upconversion efficiency when tuning the QCL wavelength away from 10.3 µm. Furthermore, it was observed that both beam pointing stability and mode quality of the QCL

laser degraded as it was tuned towards longer wavelengths, reducing the conversion efficiency.

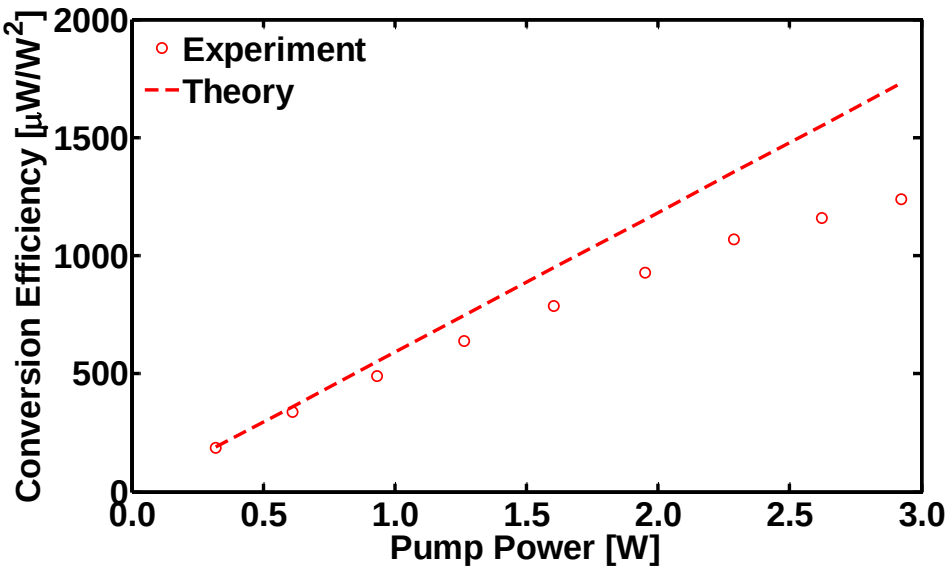

Figure 3.12: Experimental upconversion efficiency (red circles) as a function of pump power at a constant infrared power. The dashed red line shows the upconversion efficiency calculated at an IR power of 10.47 mW for a 7.7 mm interaction length using the integral method.

The measured upconversion efficiency as a function of mixing power for a signal wavelength of 10.3 µm is depicted in Fig. 3.12, exhibiting a linear increase of the conversion efficiency with increasing pump power. Since $AgGaS_2$ has poor thermal conductivity, thermal lensing becomes an increasing issue as the mixing power increases, leading to a reduced accuracy of the theoretical modeling, see Fig. 3.12. This model can used to optimize the performance of the LWIR upconversion detector before its implementation. Fig. 3.13 illustrates the simulated upconverted power as a function of the beam waist (radius) of the LWIR and the pump beams using the integral approach (dashed red line) and the plane-wave approximation (blue line). The upconverted power are calculated at an IR power of 10.47 mW for a 7.7 mm interaction length and the beam waists of the LWIR beam and the pump beam are set identically ($W_{ir} = W_p$). It is can be seen that the maximum upconverted power is found at the beam size of ∼45 µm. The upconverted power calculated at the beam waist above ∼350 µm using the integral approach starts approaching to the power calculated using the plane-wave approximation. The conversion efficiency can be further optimized by separately modeling the beam sizes of the LWIR and the pump beams using the integral approach, see Fig. 3.14. The upconversion efficiencies are calculated at an IR power of 10.47 mW for a 7.7 mm interaction length.

The maximum upconverted power simulated using the integral approach is found at the beam sizes of ∼45 µm and ∼40 µm for the LWIR beam and the pump beam, respectively. It can be seen importantly, the beam diffraction needs to be taken into account in order to accurately estimate the performance of the LWIR upconversion detector, even for relatively large beam sizes.

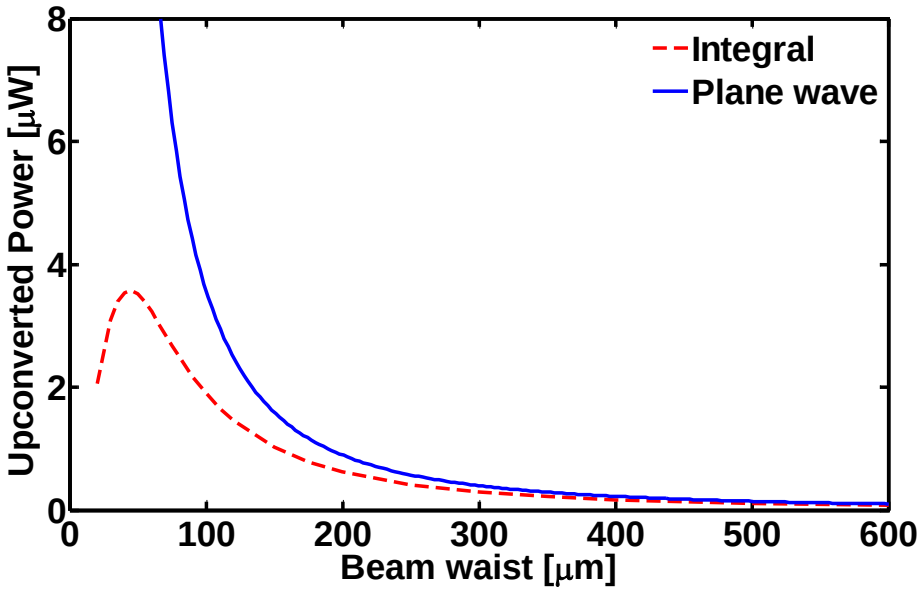

Figure 3.13: Simulated upconversion efficiencies as a function of beam waist (radius) of the LWIR and the pump beams (varied at the same size) using the integral approach (dashed red line) and the plane wave approximation (blue line). Both lines shows the upconversion efficiencies calculated at an IR power of 10.47 mW for a 7.7 mm interaction length.

3.2.5 LWIR pulse measurement

Direct detection of LWIR pulses has traditionally been challenging due to a slow rise time of conventional infrared detectors, i.e. MCT detectors. Upconversion allows for the use of silicon detectors with typically much faster response times. Fig. 3.15(a) shows exemplary oscilloscope traces of upconverted LWIR pulses with a duration of 50 ns (λ_{ir} = 10.3 µm). The upconverted signal was detected by a silicon avalanche photodiode (APD210, Thorlabs) with a rise time of 500 ps, showing good signal to noise ratio even for single-pulse detection. The average power of the LWIR signal was varied between 5.24 mW to 10.22 mW by adjusting the QCL driving current. Fig. 3.15(b) shows oscilloscope traces averaged by 50 sweeps and enlarged time scale in order to visualize the pulse separation of 1 µs. It should be noted that the pulse shape is skewed due to the AC-coupled mode of operation of the APD detector.

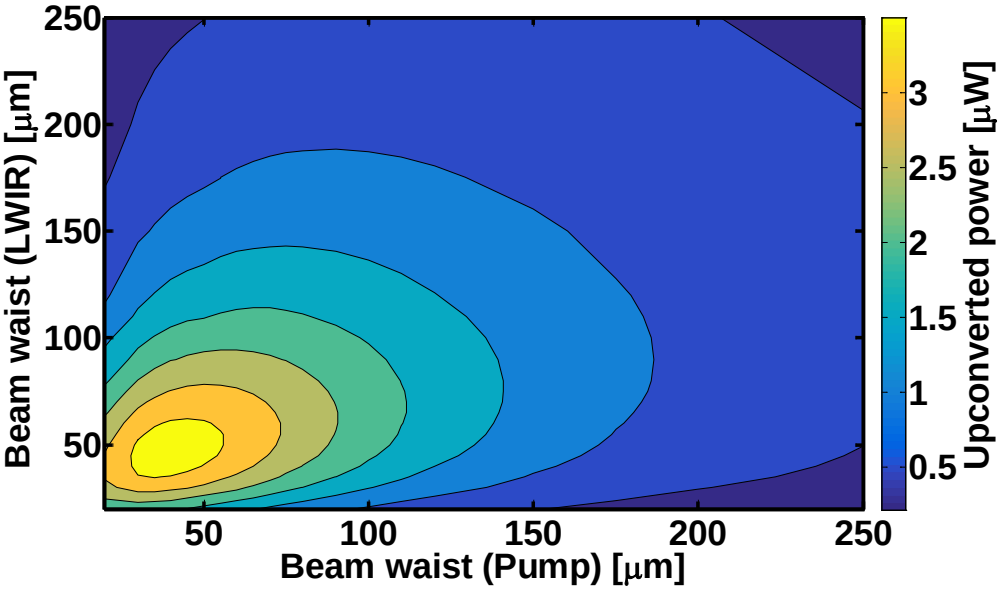

Figure 3.14: Simulated upconversion efficiencies as a function of beam waist (radius) of the LWIR and the pump beams using the integral approach. The upconversion efficiencies calculated at an IR power of 10.47 mW for a 7.7 mm interaction length.

When using a stable continuous-wave pump laser for the upconversion process, the frequency upconversion scheme does not add timing jitter nor amplitude fluctuations to the upconverted signals, hence allowing for direct pulse characterization.

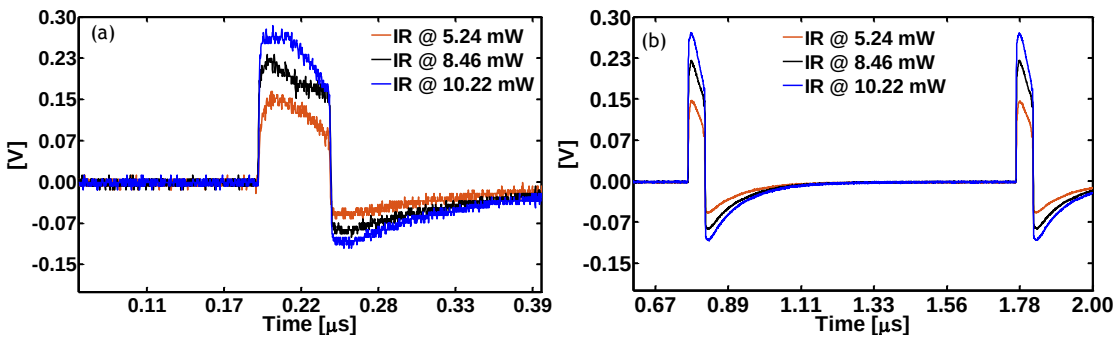

Figure 3.15: (a) Oscilloscope traces of upconverted 50-ns pulses at IR powers of 5.24 mW, 8.48 mW and 10.22 mW respectively. (b) Oscilloscope traces of upconverted signals averaged by 50 sweeps.

3.3 Summary

In this chapter we demonstrated the capabilities of upconversion detection for long-wave infrared sensing in a wide wavelength range with fast acquisition speeds and a good signal-to-noise ratio even for single-pulse detection. This is suitable for real-world applications at room temperature using only silicon detectors and the fast acquisition time enables real-time measurements. In addition, a detailed numerical model was presented, showing excellent agreement with measured data, in terms of both conversion efficiency and acceptance parameters, in which we take into account the finite beam sizes, diffraction, angular dependent refractive index and absorption of the infrared signal in the nonlinear crystal. Such detailed analysis paves the way for upconversion detection to be used not only for raster-scanned imaging in the LWIR wavelength range to identify breast cancer microcalcifications, which is discussed in chapter 4, but also for gas monitoring, see section 5.3. Although the absorption of the $AgGaS_2$ crystal increases dramatically above 8 µm, it is still possible to use this material for upconversion detection up to about 12 µm if the losses are properly accounted for in the simulations for accurate predictions. The obtained results show great potential for upconversion detection in long-wave infrared spectroscopy. Furthermore, the detection wavelength range of LWIR can be expanded from 12 µm to ∼18 µm by using an $AgGaSe_2$ as the nonlinear crystal, which has good transparency, e.g. ∼95 % transmission at a wavelength of 12 µm in contrast an $AgGaS_2$ crystal, which has only ∼10 % transmission at 12 µm, however, at the expense of having to use longer wavelength mixing lasers to enable phase matching. This is discussed in section 6.2 as apart of future work.

Chapter 4

Breast cancer detection

In contrast to traditional diagnosis for cancers through examination of samples that are required to be endogenously stained, one interesting alternative way to identify a cancerous invasion in breast lesions is spectral analysis of microcalcifications. Here, we present an upconversion microscopy imaging system capable of providing chemical images with wavenumbers below 900 cm^{-1}. IR signals below 900 cm^{-1} detected using a regular FTIR system (Agilent 670) are suffering from a poor signal to noise ratio due to unavoidable dark noise originating from the finite temperature of the LWIR detector as pointed out in section 1.1, combined with the generally low spectral brightness of broadband light sources in this spectral range. Silicon detectors on the other hand have low leakage current and generally offer lower noise and cost, but they are only sensitive up to about 1000 nm of wavelength (10 000 cm^{-1}) and thus cannot be used for LWIR detection directly. In this work, we combine an upconversion system for converting LWIR into NIR signals, which can be easily acquired by silicon based detectors, with a high brightness tunable QCL and a microscopy unit (facilitating X-Y micro-movement) for LWIR imaging detection of biological samples. One advantage of such system is that there is no need of endogenous staining of samples. By using a silicon detector, the upconversion system is capable of measuring LWIR signals down to 830 cm^{-1}, potentially giving a better SNR in this spectral range than direct LWIR detectors.

4.1 Background

4.1.1 Standard breast cancer diagnosis

Breast cancer is the second most common cause of cancer death among women after lung cancer in the United States in 2018 [37]. To improve the prognosis for these

patients, an early diagnosis is necessary. Microcalcifications, which are abnormal deposits of calcium in the mammary gland, is an early marker for breast cancer [14]. Microcalcifications are classified according to their spatial distribution in the breast as well as their biochemical composition. The current method to detect these calcifications is mainly based on X-ray mammography. A mammogram can assist in identifying suspicious breast calcifications, but, unfortunately, this technique cannot accurately discriminate between microcalcifications from a benign or a malignant lesion. Fig. 4.1 shows examples of microcalcifications associated with (a) benign and (b) malignant changes via screening mammography. A biopsy is recommended as the practical procedure to examine suspected radiological findings in human breast.

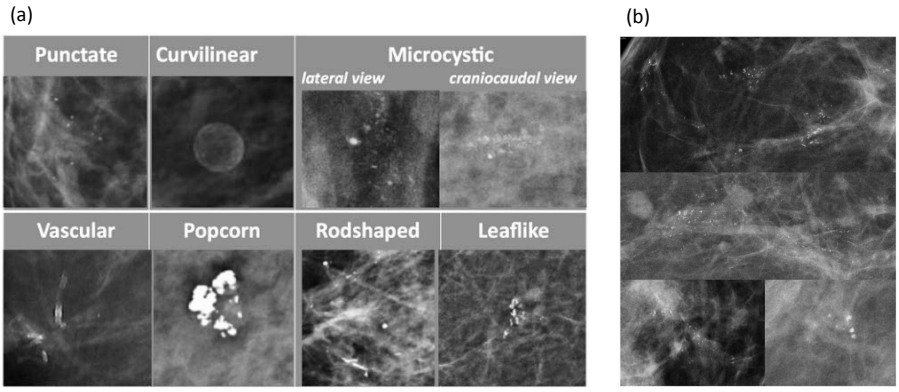

Figure 4.1: Examples of microcalcifications (white specks) associated with (a) benign and (b) malignant changes. Figure adapted from [38].

The biopsy is thinly sectioned using a microtome before being stained with hematoxylin and eosin (H&E). H&E staining is used to dye cells in corresponding colors for visualizing molecular composition under a microscope. Hematoxylin dyes basophilic cell components (e.g. nuclei of cells) with a blue color, whereas eosin stains acidophilic cell components (e.g. cellular protein) pink. The stained tissue sample is analyzed by experienced histo-pathologists to reach a medical diagnosis with given types of cancer and grades based on pathological examination. Fig. 4.2 shows a histological section of a ductal carcinoma *in situ* (*DCIS*) containing microcalcifications. The biopsy is stained with H&E staining and imaged with a transmission microscope. Biopsy followed by transitional histological analysis remains a gold standard for identification and classification of breast cancer. To complement histo-pathologic assessment, a protocol of stainless imaging is highly desirable and vibrational spectroscopic techniques have such analytical capability.

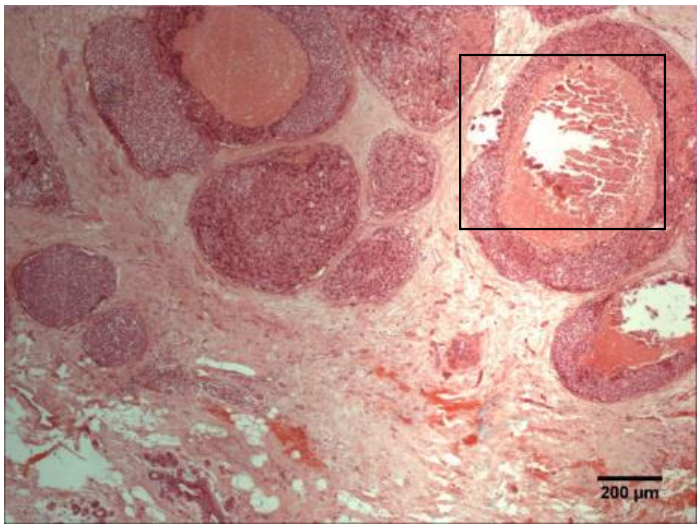

Figure 4.2: H&E stained ductal carcinoma *in situ* (*DCIS*) containing microcalcifications marked with a black square.

4.1.2 label-free detection of biological samples

Molecular bonds with a vibrational dipole moment are IR active. Therefore, infrared spectroscopy can be used to probe chemical structures and to obtain molecular information from biological samples, making it a powerful and sensitive tool for label-free biomedical diagnosis [39]. The combination of microscopy and mid-infrared or Raman spectroscopy has progressed over the past decades, providing spectral information as well as the distribution of the different constituents without exogenous staining of the samples [40]. In addition, vibrational spectroscopic imaging can be used for label-free mapping of tissue sections to provide a spatial distribution of the molecular composition within cells and tissues without the need for staining. Mid-IR absorption spectra [41] or Raman inelastic scattering spectra are recorded at each microscopic pixel in the image, resulting in a multi-dimensional dataset, which can be used to investigate diseases based on subtle changes in the characteristic spectral signatures. Raman and IR hyperspectral imaging are complimentary approaches and have been demonstrated to be able to discriminate numerous diseases based on spectral imaging of molecular changes associated with early and late diseases in various organs [42–45]. Hyperspectral imaging is a technique that combines spectroscopy and imaging where monochromatic images can be retrieved from a hyperspectral data cube in which each individual image contains spatial (X, Y) and spectral (Z) information, shown in Fig. 4.3.

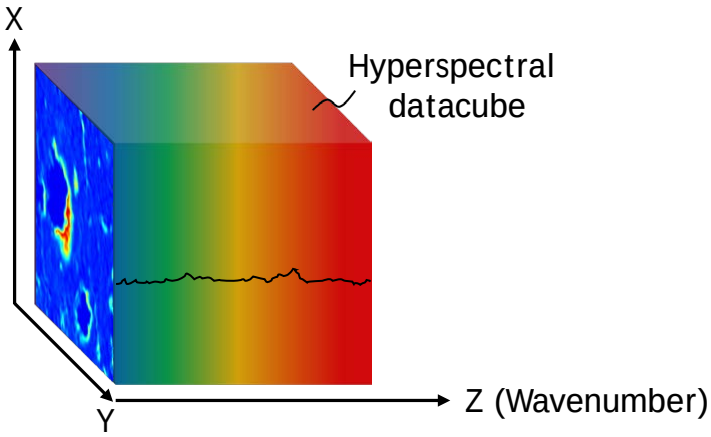

Figure 4.3: A schematic concept of a hyperspectral data cube containing spatial (X, Y) and spectral information (Z).

Raman spectroscopy was first demonstrated by Haka *et al.*for the analysis of the chemical composition of microcalcifications in different lesions of the breast [46]. Raman spectroscopic imaging can provide complimentary vibrational molecular spectral information on tissue samples with less sample preparation effort than in the case of IR imaging where the tissue sample needs to be dried in order to remove the effect of water saturating the IR signals. However, Raman spectroscopy is a slower method due to the low scattering cross-section of biomolecules. In order to increase the Raman signal, coherent Raman scattering (CRS) techniques have been developed [47]. It has been demonstrated that the coherent anti-Stokes Raman scattering (CARS) and stimulated Raman scattering (SRS), can provide cellular and chemical compositions from tissues, such as from calcified cartilage [48]. CRS techniques are able to provide fast label-free imaging acquisition. Raman and CRS spectroscopy have many advantages such as high resolution and low water sensitivity, but autofluorescence from the biological sample is the most important challenge to overcome. Further improvement of these techniques is expected to deliver numerous tools for use on *ex vivo* fluids, cells and tissues for point of care analysis in pathology or *in vivo* clinical applications.

Fourier-transform infrared (FTIR) imaging is reasonably rapid (tens of minutes per spectral image) and is recognized as a highly effective and reliable method for providing spectral analysis of biological tissue samples [49]. However, FTIR is currently too slow for real-time imaging, which is required for rapid hyperspectral pathology. In recent years, discrete frequency IR microscopes with tunable mid-IR laser sources, such as quantum cascade lasers, optical parametric oscillators or filtered supercontinuum light sources have been demonstrated, enabling label-free classification of cancerous tissue [6–8, 50–52]. By tuning the illuminating wavelength to a

molecular absorption resonance of interest, real-time molecular IR imaging can be utilized for immediate unstained tissue analysis as a rapid assessment. Furthermore, for advanced spectral predication of disease, the Bhargava group has shown that using a commercial confocal microscope with a QCL source coupled to a mercury cadmium telluride (MCT) detector it was possible to automatically screen breast tissue biopsies (1 mm diameter) in ∼1 h in high definition [53].

To date, all the above IR imaging techniques have relied upon detectors sensitive to mid-IR photons, e.g. mercury cadmium telluride focal plane arrays (MCT-FPA) or micro bolometers for LWIR detection. However, these detectors have a signal-to-noise ratio several orders of magnitude lower than that of silicon detectors and need cooling for optimal operation. Even with cooling, these direct LWIR detectors are still noisy compared to silicon detectors. Another issue is the temporal response of most direct LWIR detectors being much slower than their silicon counterparts, resulting in either low signal-to-noise ratio or long acquisition time for direct LWIR detection [54].

4.1.3 Our approach

In this work, we have advanced the current state of the infrared spectroscopic imaging technique by developing a frequency upconversion apparatus combined with a raster scanning infrared imaging microscopy system. Our approach is to convert the LWIR signal transmitted through the sample into the visible and near IR range via nonlinear frequency conversion and to subsequently use a silicon detector to detect the converted signal. This allows for the use of silicon detectors, which are fast, sensitive and cost efficient compared to their mid-infrared counterparts, and improving the signal-to-noise ratio compared to direct LWIR detection. The upconversion imaging system obtain monochromatic images, for a given setting of the light source. This is especially useful for imaging the carbonate composition of breast cancer microcalcifications at $875\,\mathrm{cm}^{-1}$. It is challenging to perform the measurement by using a commercial Micro-FTIR system (Agilent 620) due to the poor signal-to-noise ratio of the MCT-FPA detector. The upconversion imaging system, consisting of a LWIR upconversion detector, a home-built microscopy unit, and a QCL, is presented in this work as a novel diagnostic tool for biomedical analysis of breast cancer biopsy. The spectral intensity ratio of carbonate ($875\,\mathrm{cm}^{-1}$) and phosphate ($1020\,\mathrm{cm}^{-1}$) bands is found to be a discriminator for breast cancer [14]. In contrast to FTIR which is taking an entire IR spectrum at a time, the QCL laser allows for discrete wavelength tuning at the particular wavelengths of interest and provides better brightness compared to a thermal light source. Scanning few wavelengths of interest is adequate

to discriminate the degree of the pathology in breast cancer [14], which potentially improves the acquisition time enabling rapid assessment.

4.2 Methods and Materials

4.2.1 Early biomarker

Microcalcifications are abnormal deposits of calcium in the mammary gland and classified according their spatial distribution in the breast as well as their biochemical composition. In fact, two types of calcifications are observed in the breast. Type I consisting of calcium oxalate are mainly found in benign lesions and type II composed of calcium hydroxyapatite (HAP) are involved in proliferative lesions and invasive cancer. HAP crystals are made of mixing carbonate ($CO_3{}^{2-}$), hydroxyl (OH^-) and phosphate ($PO_4{}^{3-}$) ions. In biological tissues, HAP is not a pure compound but contains within its lattice around 5 % to 6 % of carbonate substitution [55]. Two types of substitution have been observed for the intercalation of carbonate in the HAP lattice: type A when $CO_3{}^{2-}$ replaces the OH– ions, and type B when $CO_3{}^{2-}$ replaces the $PO_4{}^{3-}$ ions [56]. The chemical nature of the microcalcification (i.e. carbonate/phosphate levels) can be used to differentiate the grade of the breast disease. In order to understand the pathological mineralization process in breast cancer microcalcification, we first analyze hydroxyapatite potassium bromide (KBr) pellets synthesized by carbonated and KBr powders using both FTIR and the upconversion microscopy system. Thereafter a breast cancer tissue is studied for spectral features at corresponding spatial locations.

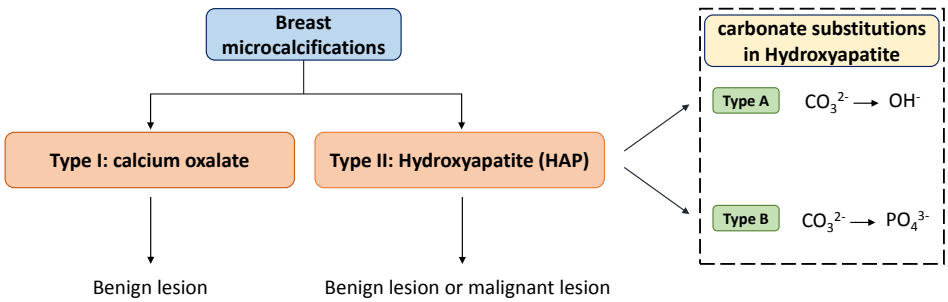

Figure 4.4: Schematic diagram of two types of microcalcifications found in the breasts and two types of carbonate substitutions observed in the hydroxyapatite lattice

4.2.2 Synthetic carbonated-hydroxyapatite KBr pellets

The mechanisms inducing the formation of calcium hydroxyapatite associated with breast cancer cells remain unclear. To understand the mineralization process, we analyze the spectral features of synthetic carbonated-hydroxyapatite samples at concentration levels of 5 % to 6 % which is similar in concentration to that of cancerous microcalcifications found in human breast.

KBr is typically used as a window material mixed with powder samples and compressed into solid pellet when performing spectral analysis. It is optically transparent within the range of 4000 cm^{-1} to 400 cm^{-1}, leading to little interference in absorption measurements. KBr pellets of different standard minerals containing carbonate substitutions of 1.24 %, 2.92 %, 4.43 %, 5.24 %, 7.52 % and 8.12 %, respectively, were made according to the following protocol: 99 mg powdered KBr was added to 0.5 mg of HAP before being ground together by a mortar and pestle. The mixture was transferred into a hydraulic press and compressed for ∼30 min with a pressure of 10 tons/176 mm^2, forming a solid pellet sample with a thickness of ∼220 µm. A pure pellet containing only 100 mg of KBr was used to obtain a background spectrum. The HAP powders were provided by Prof. Mary Tecklenburg, Central Michigan University, USA. The pellets being analyzed in this study were made by our medical partner at the University of Exeter.

4.2.3 Breast cancer sample

The *ex vivo* breast cancer biopsy [57] containing microcalcifications was from a patient who had undergone a biopsy for mammographically suspicious breast lesions and it was selected from the histo-pathological report. The biopsy was embedded in paraffin and two 3 µm-thick adjacent sections were cut from the biopsy sample for further diagnostic analysis. One section without H&E staining was mounted onto a 0.5 mm-thick barium fluoride (BaF_2) disc and analyzed using the Micro-FTIR and the upconversion microscopy systems. The tissue section is required to be this thin to enable sufficient IR light penetration into the highly absorbing mineralized tissue for FTIR analysis. The other section was stained with H&E staining and used for medical histological analysis as the gold standard reference. The images of both sections are shown in Fig. 4.5.

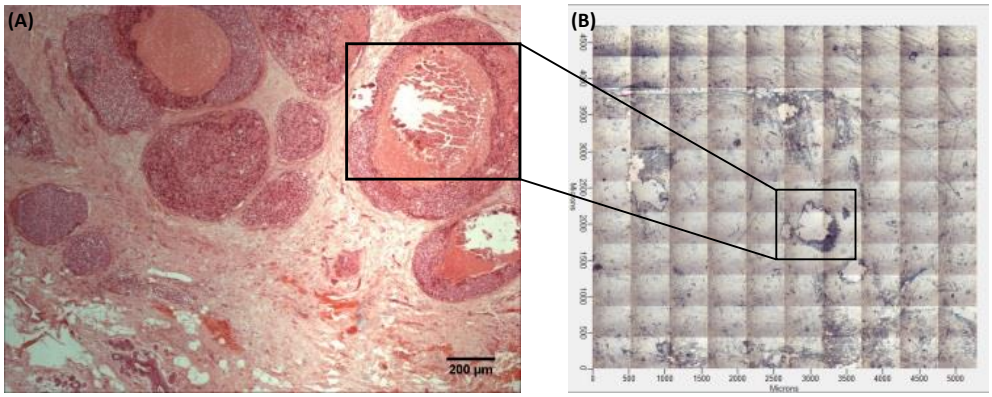

Figure 4.5: Transmission microscope images of histological sections of ductal carcinoma *in situ* (*DCIS*) breast cancer microcalcifications with (a) H&E staining and (b) unstaining for the analysis by the infrared spectroscopic imaging system. The area corresponding to microcalcification in the biopsy sample is marked with black squares.

4.3 FTIR system

4.3.1 Fundamental

Fourier transform infrared spectroscopy with the application of a Michelson interferometer is an analytical technique capable of collecting absorption spectra over a wide wavelength range through Fourier transform of the acquired signals. FTIR is commonly used for biomedical analysis of tissue samples with spectral studies based on their relatively weak vibration features. Fig. 4.6 shows the operation principle of a FTIR system. FTIR generally consists of a broadband light source, a Michelson interferometer, and an IR detector as the key components. A globar (thermal source) is used as the illumination source in FTIR, emitting infrared radiation at a continuum of wavenumbers over a wide IR range. By moving the mirror in one arm, an interferogram is obtained containing information about the light passing through the instrument and ultimately through the sample. This interferogram is Fourier-transformed to retrieve the spectrum of the IR radiation at the output of the instrument.

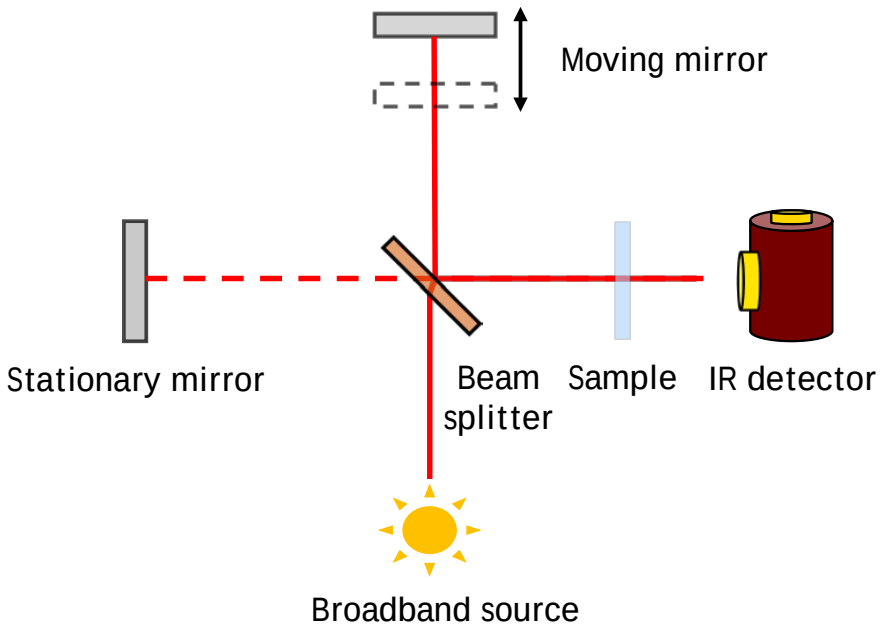

Figure 4.6: An illustration of the operational principle of an FTIR system. Light is split into two arms by a beam-splitter before being reflected by mirrors and recombined at the beam-splitter. An interferogram is produced according to the changes in optical path length. The infrared light from both arms is passing the sample and is subject to interaction with the substance and the result is measured by the IR detector. A Fourier transform converts the interferogram into an equivalent spectrum representing the intensity of the infrared signals versus frequency or wavelength.

4.3.2 Micro-FTIR system

A Micro-FTIR system was used in this study for biomedical identification of breast cancer tissue. The Micro-FTIR system can operate in both single-point and spatial imaging modes using either a MCT or a MCT-FPA (focal plane array) detector. The MCT-FPA detector has 128 × 128 pixels, which allows acquisition of spectral information from different spatial locations simultaneously. The Micro-FTIR system consists of a globar source, an Agilent 670 FTIR spectrometer, an Agilent 620 FTIR microscope, and the aforementioned IR detector. The FTIR spectrometer is coupled to a microscope, which consists of a 15× cassegrain objective and a beam condenser. The MCT-FPA IR detector has to be cooled with liquid nitrogen to ∼77 K for optimal operation.

4.4 First generation of the upconversion microscope imaging system

4.4.1 Experimental setup

Fig. 4.7 illustrates the first generation of the upconversion microscope imaging system. It consists of a QCL, a home-built microscopy unit (consisting of the microscope and a X-Y translation stage), and the LWIR upconversion detector unit described in chapter 3. The settings (the beam waists of both pump and QCL) are remained the same as those used in chapter 3 but power of the pump source is set to ∼1.6 W to increase upconverted signals.

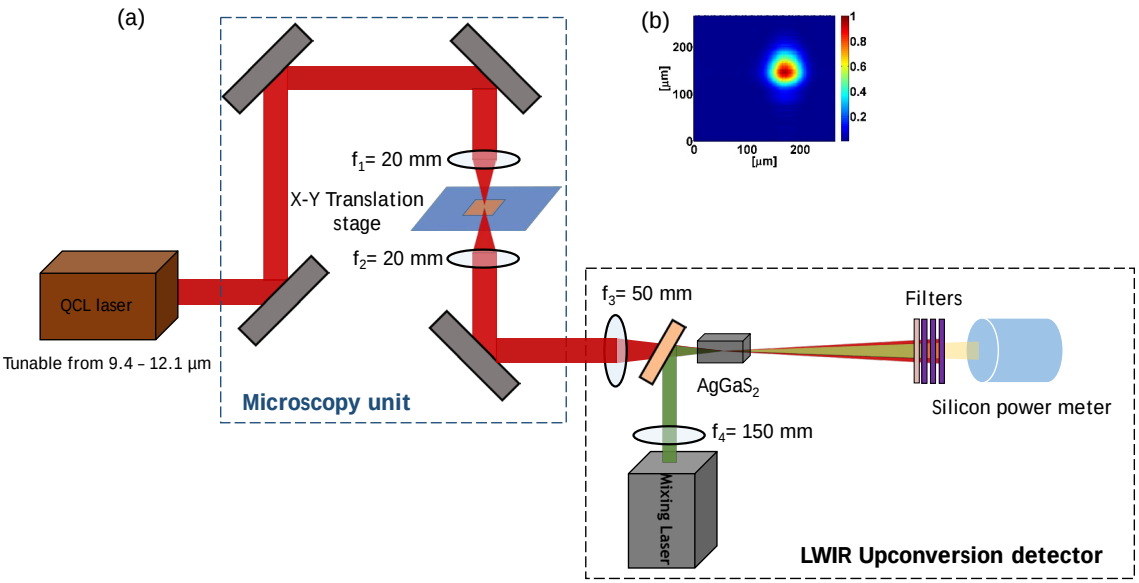

Figure 4.7: (a)Schematic layout of the first generation upconversion raster scanning microscopy imaging system. The upconversion system consists of a LWIR light source, a scanning microscopy unit, and an upconversion detector.(b) Beam profile at the focus of LWIR light source.

The QCL can be tuned to emit light in the range from 1060 cm^{-1} to 830 cm^{-1} (9.43 µm to 12 µm) with a linewidth of ∼1 cm^{-1}, see subsection 3.1.1. The LWIR beam is coupled into the microscopy unit and focused onto the sample placed on the X-Y translation stage. The X-Y translation stage moves the sample in a plane perpendicular to the beam waist, which is stationary and focused using two ZnSe lenses ($f_1 = f_2 = 20$ mm) mounted on Z-axis translation mounts. The beam diameter

of the LWIR beam defines the minimal spatial resolution at which the raster scanned images are acquired by combining each scanned point into a two-dimensional array. The LWIR beam diameter was measured using the knife edge method, where a knife is placed on the X-Y translation stage and scanned across the LWIR beam in both the X- and Y-direction. The measured beam size is found to be Gaussian with a diameter of 96 µm. Fig. 4.8 shows a schematic of the experimental setup of the first generation upconversion microscopy imaging system.

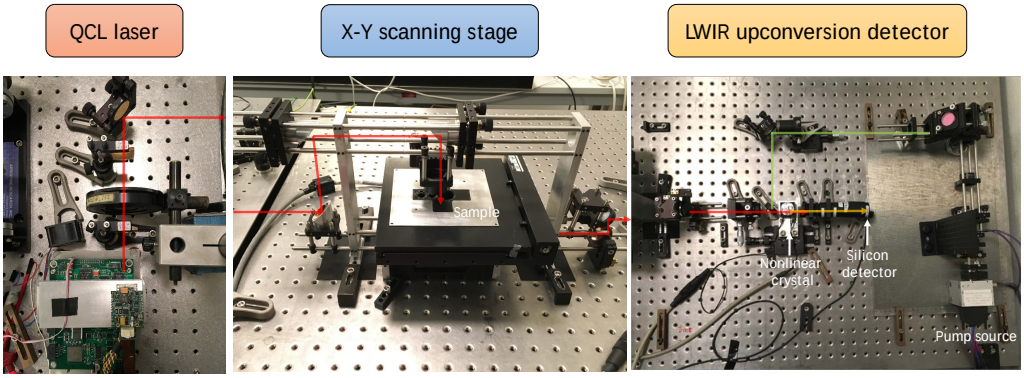

Figure 4.8: Photos of the experimental setup of the first generation upconversion microscope imaging system consisting of a QCL, a microscopy unit, and an upconversion detector.

4.4.2 Data acquisition

The X-Y translation stage scans in two dimensions to form a 2D image of the sample. The The acquired images are monochromatic as the QCL wavelength is held fixed during a complete 2D scan. The X-Y translation stage moves to an (X-Y) position, which is assigned according to a programmed scan pattern. Once the X-Y translation stage arrives at the requested position, the stage stops and wait until a signal from the silicon detector has been acquired. The process is repeated until the scan pattern is completed. This configuration is called Move-Pause because the X-Y translation stage does not move while the silicon detector acquires the upconverted signal, see Fig. 4.9.

The X-Y translation stage takes ∼0.2 s to move a step while the detector is set to pause state. The duration of ACQ state is ∼0.3 s due to the averaging of 100 samples with an integration time of 3 ms each. The acquisition time for a single pixel in the move-pause mode limits the speed of the upconversion system.

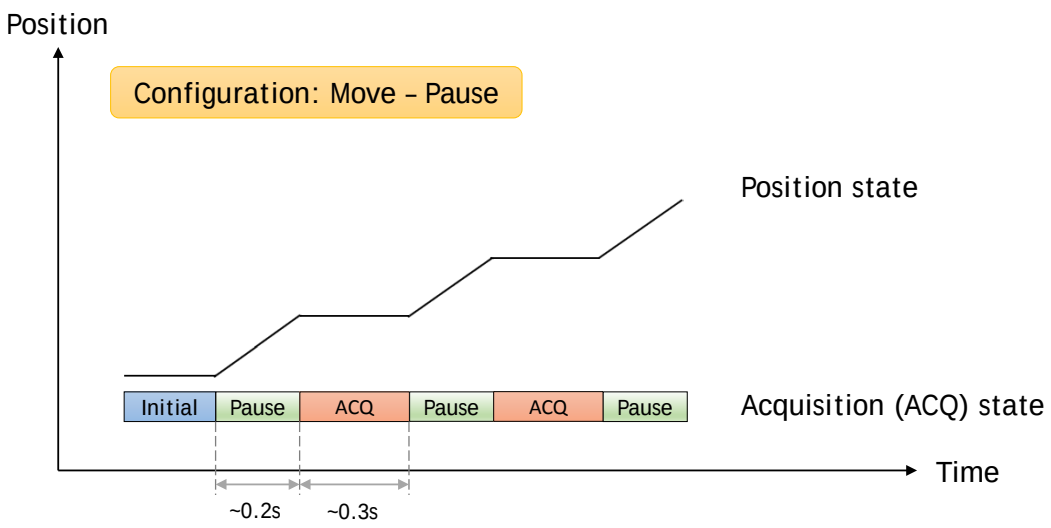

Figure 4.9: Schematic illustration of the concept of sequential movement and data acquisition of the upconversion system during a 2D image scan. The X-Y translation stage moves and pauses in an alternating pattern and the silicon detector signal is acquired (ACQ) while the X-Y translation stage is in the paused state. The durations of the pause and the ACQ states are ∼0.2 s and ∼0.3 s, respectively. In the initial state, the QCL wavelength is set and the X-Y translation stage is moved to a start-position.

4.4.3 Absorption spectroscopy

In this work, we are particularly interested in absorption spectroscopy in the LWIR region. Light is absorbed by the sample at specific wavelengths, revealing the unique absorption features of the tissue sample. It is well known that molecular 'fingerprints' allow exploring biochemical properties of biological tissues based on molecular functional groups and biochemical bond signatures. The absorbance is calculated from the measured transmittance through the sample. The transmission is the ratio of the detected signal with and without the sample given by

$$T = \frac{I_o}{I_i} \tag{4.1}$$

where I_o is the detected intensity of the LWIR beam passing through the sample and I_i is the LWIR beam intensity transmitted through a substrate without a sample, see Fig. 4.10. BaF_2 was used as the substrate and sample carrier material due to its excellent transmission in the LWIR region.

The absorbance is given by

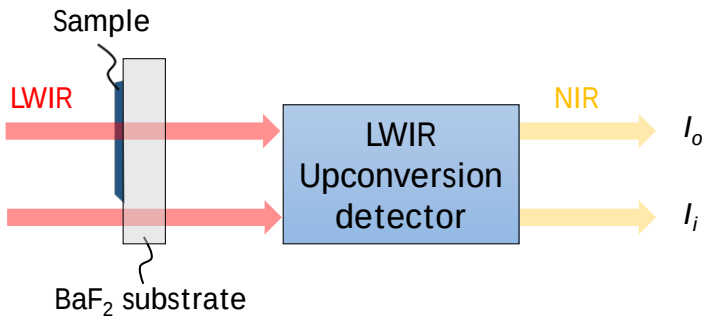

Figure 4.10: Schematic concept of an absorbance measurement. The LWIR signal passing through the sample and the BaF_2 substrate is upconverted into the NIR region. The transmitted beam through the sample is I_o and the signal passing only through the substrate has the intensity I_i ($I_i > I_0$).

$$A = -\log(T) = -\log \frac{I_o}{I_i} \tag{4.2}$$

Eqn (4.2) is used for calculating the absorbance and the results are presented in the following sections.

4.4.4 Analysis of carbonated hydroxyapatite sample

Fig. 4.11 shows the absorption spectra of the carbonated hydroxyapatite samples obtained using both the Micro-FTIR and the upconversion detection system. The micro-FTIR system is used in single-point mode, i.e. collecting one spectrum from a single detector element, to analyze the KBr pellets containing carbonate substitution of 1.24 %, 2.92 %, 4.43 %, 5.24 %, 7.52 % and 8.12 %, respectively. A pure pellet containing only KBr powder is used to obtain a background reference spectrum. Each spectrum with different amount of carbonate substitution was obtained by averaging 32 scans and the background spectrum was obtained by averaging 64 scans. The FTIR spectra are recorded in the spectral range of 4000 cm^{-1} to 700 cm^{-1} with a spectral resolution of 4 cm^{-1}. Phosphate absorption peaks are found in the range of 1020 cm^{-1} to 1040 cm^{-1} and at 962 cm^{-1}, and a carbonate peak is observed at 875 cm^{-1} using the FTIR system. Note that the FTIR spectra are post-processed with baseline correction and curve fitting using a commercial software (OPUS), which is contrast to the upconversion spectra presented as its raw data. This leads to the different scales in absorbance (Y-axis) in both graphs.

The HAP samples with 7.52 % and 2.92 % carbonate substitution was subsequently analyzed using the upconversion system. The upconversion spectra were measured at a single (X,Y) position at the KBr pellets with a beam radius of 48 µm.

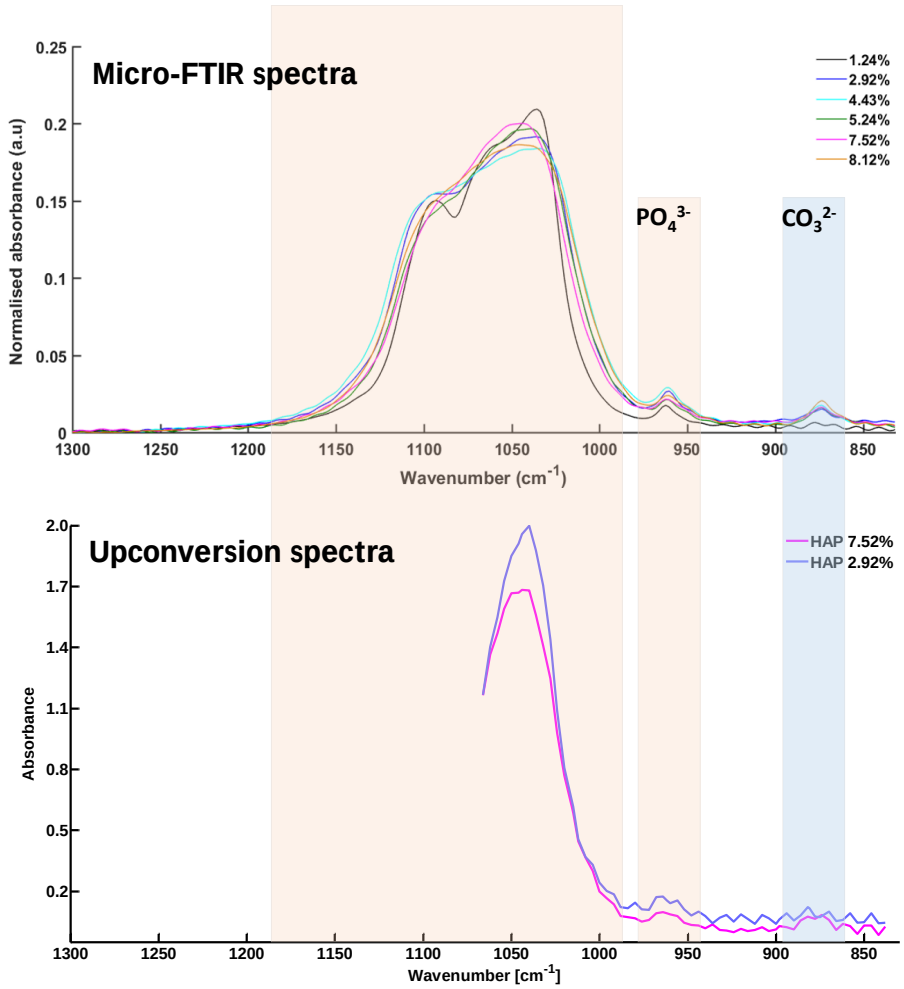

Figure 4.11: Spectra of KBr pellets containing HAP powders measured by the micro-FTIR system in the spectral range 1300 cm^{-1} to 830 cm^{-1} (top) and by the upconversion system (bottom) in the spectral range of 1068 cm^{-1} to 830 cm^{-1}

The upconversion spectra are recorded from 1066 cm^{-1} to 830 cm^{-1} in steps of 4 cm^{-1} and 5 scans were averaged for each pellet. Absorption peaks of phosphate and carbonate bands are observed in the spectra at 1044 cm^{-1}, 964 cm^{-1} and 875 $cm^{-1}$for the sample with 7.52 % carbonate substitution, and at 1044 cm^{-1} and 964 cm^{-1} for the sample with 2.92 % carbonate substitution.

Note that the absorption spectrum measured using the upconversion system shows artefacts as a periodic modulation of the signal, resulting in the carbonate band to be hardly observed (blue line, upconversion spectrum) for the sample with 2.92 % carbonate substitution. In order to investigate the origin of the artefacts in the upconversion spectra, the transmission profile (2D image) of the HAP 7.52 % pellet

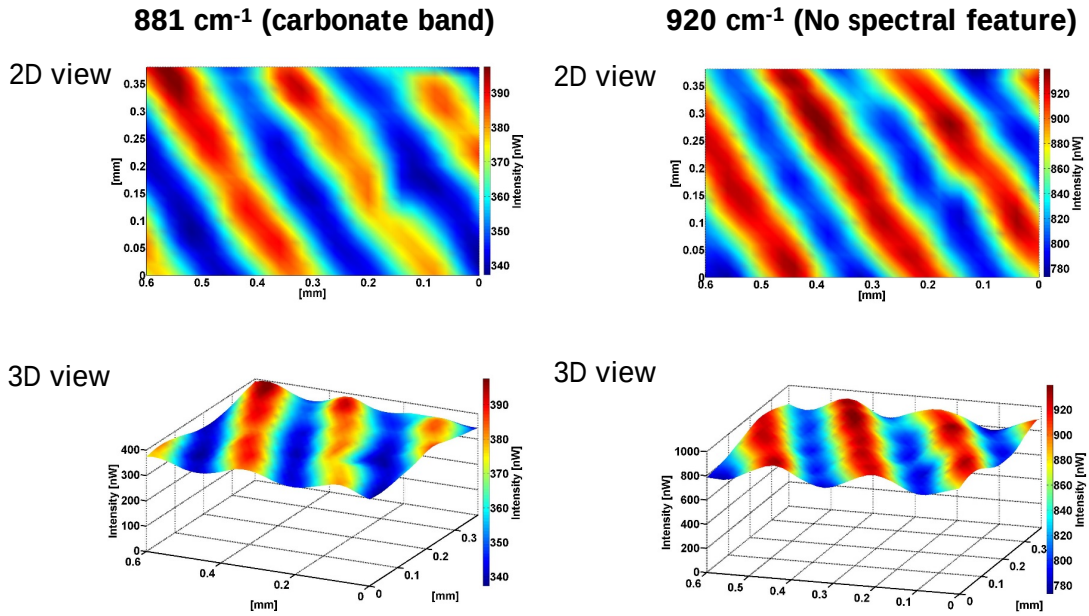

Figure 4.12: 2D/3D Intensity maps of HAP with 7.52 % carbonate substitution measured at 881 cm^{-1} to 920 cm^{-1} respectively measured using the upconversion system. Note the different scales at the two wavelengths.

was recorded at 881 cm^{-1} (carbonate band) and 920 cm^{-1} (no spectral features) using the upconversion system with raster scanning for comparison, which is shown in Fig. 4.12.

The same area was scanned at the two wavelengths showing an interference-like pattern, albeit spatially shifted. A similar pattern was observed in another pellet (not shown). The interference fringes are moving with wavelength, hence, we can attribute the artefact present in the upconverted spectra to the interference between the front and back surface of the pellet when using a coherent illumination source like the QCL rather than to heterogeneity of the HAP powder in the pellet. The transmitted intensity distributions shown in Fig. 4.12 are consistent when using a coherent light source on a slightly wedged pellet. One way to be considered removing the unwanted periodic modulation pattern from signals is to average an scanned area large enough to suppress the intensity modulation if HAP samples are very uniform.

4.4.5 Analysis of breast cancer microcalcifications

Fig. 4.13 shows the FTIR and the upconverted images of microcalcifications found in ductal carcinoma *in situ* breast cancer tissue. Fig. 4.13(a) depicts a histological section of in situ breast cancer tissue with H&E staining.Fig. 4.13(b) is obtained

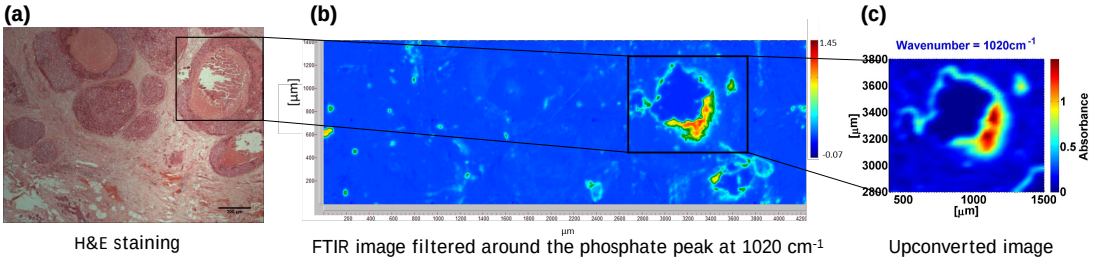

Figure 4.13: (a) Histological section with H&E staining using a transmission microscope with 4× magnification. (b) FTIR image filtered around the phosphate peak at 1020 cm^{-1} with 15x magnification (pixel size: 5.5 µm × 5.5 µm). (c) Upconverted image at the phosphate peak illuminated at 1020 cm^{-1} with scan step size of 20 µm.

at 1020 cm^{-1} using the micro-FTIR imaging system with a 128 × 128 pixel MCT-FPA detector. Fig. 4.13(c) shows the same tissue sample imaged by the upconversion system measured at the same wavenumber of 1020 cm^{-1} corresponding to the phosphate band. The upconverted image was measured by raster scanning with step size of 20 µm. The LWIR signal transmitted through the sample was upconverted from 1020 cm^{-1} into NIR (959 nm) which was detected using a silicon based power meter. The upconverted image shows good agreement with the FTIR image at a similar wavenumber. The acquisition time of an upconverted image with an area of 1 mm^2 is ∼20 min. This is due to the limited response time of the system when operating in the move and pause scanning acquisition mode.

Only few discrete wavelengths are required to identify the microcalcifications for phosphate and carbonate bands at 1020 cm^{-1} and 875 cm^{-1}. Fig. 4.13 shows the upconverted images obtained at the wavenumbers of 1020 cm^{-1}, 975 cm^{-1}, 964 cm^{-1}, 920 cm^{-1}, 881 cm^{-1}, 875 cm^{-1} and 842 cm^{-1}, respectively, acquired with a raster scanning step size of 20 µm. It is evident that there is a significant decrease in signal (increased absorbance) at the phosphate absorption band in the microcalcification area (black square) compared to the surrounding. Acquiring images at other wavelengths allows an estimation of the relative compositional contributions to the spectral absorption, thus enabling further analysis of the spectral features of the microcalcifications.

The absorption spectrum was analyzed in an area where the phosphate band is highly absorbing, as shown in Fig. 4.15(a). Fig. 4.15(b) shows the spectrum extracted from the microcalcification area (dashed square), whereas Fig. 4.15(c) shows a spectrum extracted from the surrounding tissue. The MCT-FPA detector becomes increasingly noisy in the LWIR regime (800 cm^{-1} to 900 cm^{-1}), therefore the signatures below 900 cm^{-1} cannot be considered reliable. The upconverted spectra

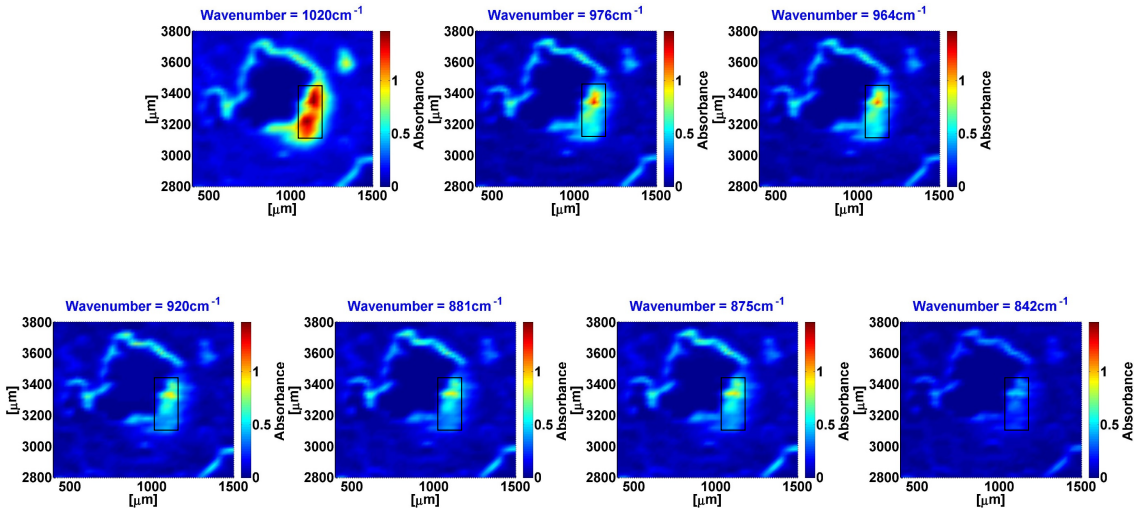

Figure 4.14: Upconverted images of ductal carcinoma *in situ* breast cancer tissue obtained at 1020 cm^{-1}, 975 cm^{-1}, 964 cm^{-1}, 920 cm^{-1}, 881 cm^{-1}, 875 cm^{-1} and 842 cm^{-1} corresponding to upconverted signals in the wavelength range of 959 nm to 976 nm.

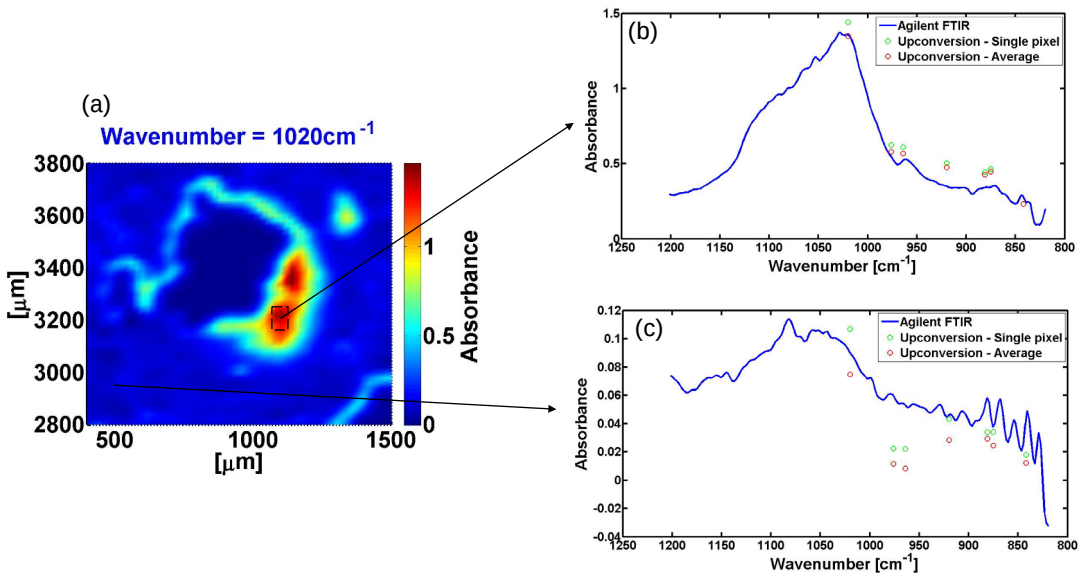

Figure 4.15: (a) Upconverted image at phosphate peak at 1020 cm^{-1} and spectra measured using micro-FTIR imaging (b) and upconversion (c) systems from microcalcification and tissue surrounding in the *DCIS* breast sample.

are retrieved from a series of images (shown in Fig. 4.14) measured at 1020 cm^{-1}, 975 cm^{-1}, 964 cm^{-1}, 920 cm^{-1}, 881 cm^{-1}, 875 cm^{-1} and 842 cm^{-1} respectively, providing the spectral information from an images extended up to 842 cm^{-1}. The spectral information in this LWIR range is critical to identify carbonate composition of the microcalcifications for discriminating between benign and malignant breast lesions, however the micro-FTIR system is limited by the MCT-FPA detector's inherently poor sensitivity in this wavelength range. The FTIR and upconverted spectra obtained from the surrounding tissue exhibit only a small phosphate absorption feature by the tissue in this area. The signals from a single pixel (green circles) and an average of 6 pixels (red circles) using upconversion are shown in Fig. 4.15(b) and (c). For comparison, a spectrum has also been extracted from the FTIR image (Fig. 4.13b) recorded by the micro-FTIR imaging system.

4.4.6 Short summary

We showed that breast cancer tissues can be analyzed using an upconversion detector with a raster scanning microscopy system at discrete wavenumbers. This has the potential to improve the signal-to noise ratio using silicon based detectors when compared to direct detection in the LWIR range. It is possible to detect the carbonate bands at 875 cm^{-1}, which can be challenging to measure with the micro-FTIR imaging system due to a combination of the limited number of IR photons at this wavelength provided by the globar illumination source and the MCT-FPA detector's inherently poor sensitivity in this wavelength range. This study paves the way for the development of a practical upconversion detector combined with a microscopy unit for biomedical diagnosis. Due to the limited response time of the silicon based power meter, the acquisition has to be done in move-and-pause mode and consequently the total time is ∼20 min per image (∼1 mm^2 at 20 µm step size). This limits the applicability of the upconversion system being used in the clinical routine. Therefore, we improved the first generation system by using a silicon amplified photodetector (PDA100, Thorlabs) to lower the response time of the detector by three orders of magnitude. At the same time, the move-and-pause mode is replaced by constant-velocity movement while the detector signal is being acquired continuously. This scheme lowers the acquisition time by a factor of ∼30 (shown in 4.5).

4.5 Second generation of the upconversion microscope imaging system

4.5.1 Experimental setup

The second generation of the upconversion imaging microscopy system is illustrated in Fig. 4.16. The X-Y translation stage scans in two dimensions using raster scanning (snake-scan), as shown in Fig. 4.16(b).

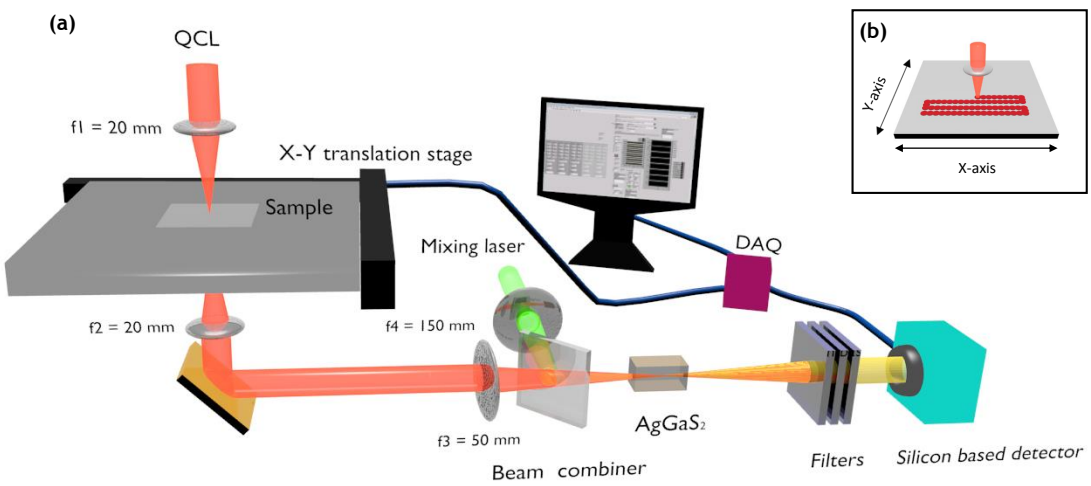

Figure 4.16: (a) Schematic layout of the experimental setup for the upconversion raster scanning microscope. (b) Raster scanning scheme of the snake-scan mode.

Several changes have been made in the setup with the aim of improving acquisition time and spatial resolution compared to the move-pause mode employed in the first generation system. Notably, a beam expander (not shown) is inserted which is composed of a pair of ZnSe lenses with focal lengths of 50 mm and 100 mm, respectively, to increase the beam diameter of the LWIR beam before being focused (f_1) onto the sample. This configuration allows the light to be focused down to a smaller spot than without the beam expander, thus leading to improved spatial resolution. The LWIR beam waist is found to be ∼28 µm (radius) in the plane of the biological sample. This is measured using the knife edge method. After passing through the sample, the LWIR beam is collimated (f_2) and refocused (f_3) into a nonlinear crystal where it is mixed with a pump beam via a beam combiner for sum-frequency generation. A silicon photodiode (PDA100, Thorlabs) with a response time of ∼350 µs (3 dB bandwidth of 1 kHz and a gain of 4.75×10^6 V/W) is used to detect the upconverted signal. In contrast, the response time of the detector used in the first

generation system (silicon power meter, Thorlabs S120C) is ∼300 ms due to the averaging of 100 samples with an integration time of 3 ms each.

4.5.2 Data acquisition

The X-Y translation stage scans in two dimensions using raster scanning, as shown in Fig. 4.16(b). The X-Y translation stage moves in the X-direction (fast axis) with a constant velocity of 5 mm/s and in the Y-axis (slow axis) in steps of a fixed size for transitioning between the X-axis lines. When the X-Y translation stage is moving along the Y-axis by e.g. a 10 µm step, the acquired upconverted signal during the Y motion is not used as it is outside the region of interest. This part of the acquired signal is subsequently discarded, and only the upconverted signal obtained on the detector while the stage is moving with a constant speed along the X-axis is preserved for the image reconstruction algorithm. The step size in the Y-direction (single step) is adjusted based on the LWIR beam size. We chose a step size of 10 µm, which is ∼5 times smaller than the LWIR beam size, constituting a compromise between image resolution and overall scan duration. The translation stage has angular encoders on the axis spindles. Each encoder provides quadrature electric signals used to track the (X, Y) position. The quadrature signal enables tracking in both the forward and backward directions. The (X, Y) position and the analog signal from the Si detector are processed by a data acquisition module (DAQ National Instruments NI-6251). The sampling rate of the DAQ module is set to 100 kHz to gain better SNR and avoid aliasing and the samples are acquired simultaneously from the analog to digital converter (ADC) and the position decoders, meaning that the detector measurement is recorded along with the corresponding X-Y position. Fig. 4.17 illustrates the concept of the data acquisition where the detector signal is acquired (ACQ) while the X-Y translation stage is moving with a constant speed.

The upconverted signal acquired on the silicon detector is low-pass filtered with a 1 kHz (3 dB bandwidth) analog passive first-order RC filter. The cut-off frequency was chosen such that it preserves the signal representing the image features at the target, but rejects unwanted high-frequency components, essentially working as an anti-aliasing filter for the subsequent temporal sampling at 100 kHz. Because the sampling rate is 100 times the bandwidth of the signal of interest, there is a wide frequency range for this analog filter to operate in and it is sufficient to use a first-order passive filter, greatly simplifying the electronics. The frequency of interest is determined by the scanning velocity of the X-Y translation stage and the feature size of the target to resolve, which is given by

$$f = \frac{v}{d} = v\xi \tag{4.3}$$

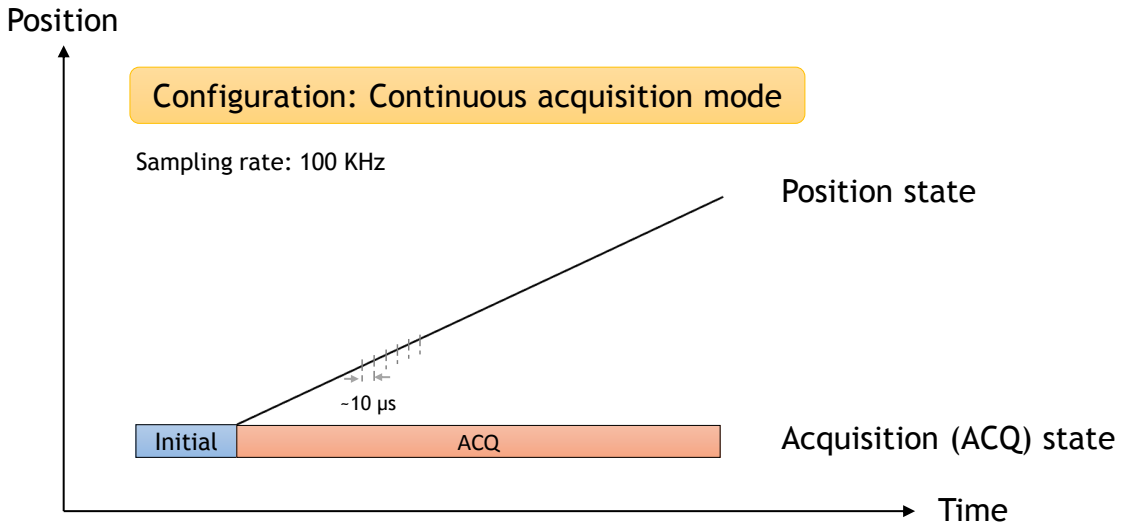

Figure 4.17: Schematic concept of the scanning data acquisition for obtaining 2D monochromatic images. The silicon detector signal and the (X, Y) position are acquired (ACQ) while the X-Y translation stage moves with a constant speed along the fast axis (X-scan). Once the X-scan is completed, the X-Y translation stage moves a step in the Y direction for the next X-scan. This scan is in the opposite direction to the previous X-scan. Since the position (X, Y) of the X-Y translation stage is known at all times, the direction of its movement is not important for the correct reconstruction of the image.

where v is the scanning velocity and d is the feature size of the target. Here, $\xi = 1/d$ denotes the spatial frequency. Thus, if moving the X-Y translation stage at 5 mm/s over a structure with a period of 25 µm, a temporal signal with a frequency of 200 Hz is produced.

To remove all signals outside the frequency band of interest, the digital data stream is subsequently digitally filtered by a finite impulse response (FIR) low-pass filter (Filter Express VI, LabVIEW). The passband frequency of the FIR filter is 200 Hz with 0.1 dB of passband ripple and the stopband edge is at 2 kHz with ∼81 dB of attenuation. The FIR filter has an impulse response with a full-width half maximum of ∼0.6 ms, which corresponds to a spatial width of 3 µm at a velocity of 5 mm/s.

Fig. 4.18 illustrates the signal characteristics in the processing chain from the target transmission, in which the target is illuminated with a LWIR Gaussian beam with a diameter of ∼56 µm (red curve). The signal is electronically filtered with a digital lowpass filter, which is approximated with Gaussian impulse response (cyan curve). We show the exemplary transmission signals of the LWIR beam illuminating slits (blue rectangles) with sizes of 62.5 µm and 35 µm, respectively, corresponding to the sizes of the USAF 1951 resolution target of group 3 (first and sixth elements,

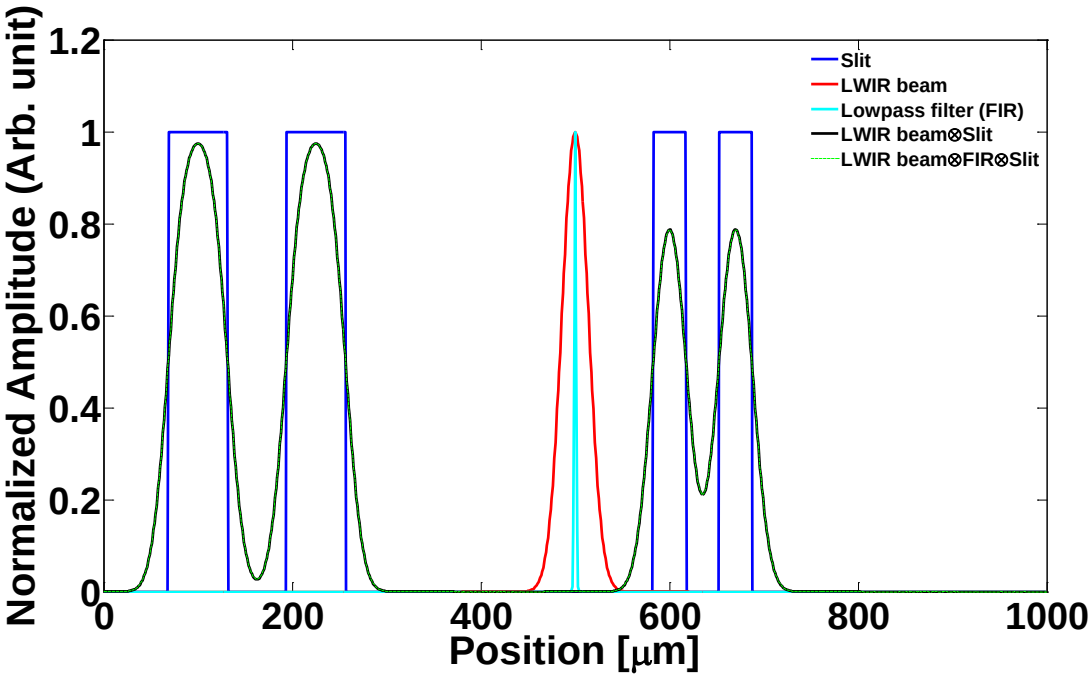

Figure 4.18: An illustration of the signal characteristics in the processing chain from target transmission, over illumination with a Gaussian beam (red curve) through electronic filtering with a digital low pass filter (approximated with Gaussian impulse response) (cyan curve). The example has the typical beam and filter values. The target has an artificial slit pattern of here 2 different slit widths but all same transmission (blue curve).

respectively). The black curve shows the signals obtained through the convolution of the LWIR beam (56 µm) with the slits (62.5 µm and 35 µm, respectively). The dashed green curve shows the signals obtained through the convolution of the LWIR beam, and the slits, after applying the digital lowpass filter to the LWIR beam via convolution. As the width corresponding to the FIR lowpass filter is much smaller than the scanning beam diameter of ∼56 µm, the filter only slightly deteriorate the combined spatial resolution. The decreasing amplitude (observed at the slits with 35 µm width in Fig. 4.18) reflects the narrow aperture of the slit compared to the larger LWIR illumination beam, see Fig. 4.19(d). Note that the fringe visibility is reduced by both the narrow slits as well as the narrow gaps between the slits, which block transmission.

The filtered signals are then binned according to the corresponding position (X, Y), and combined into an image array with an assigned pixel size of (X, Y) = (10 µm, 10 µm). The pixel size in the X direction can be arbitrarily assigned, e.g. to 2 µm smaller than that in the Y direction. This is because the data obtained in the Y direction is composed of single steps per X-line instead of a continuous data from constant-velocity movement of the stage along the X-axis. The binning of the

samples into the 10 µm × 10 µm array is done by averaging all samples within the respective spatial interval.

The field of view of the image is subsequently cropped by removing about 10 % of the outer border of the image. This discards regions with non-constant velocity at the end of each X-scan where the stage is accelerating and decelerating before stepping to the next line in the slow (Y-axis) direction. The remaining inner image portion is then resampled into a 1000 x 1000 pixel image, i.e. with a pixel size of 1.8 µm × 1.8 µm for a scan area of 1.8 mm × 1.8 mm. The resampling uses standard image processing algorithms (cubic spline), which are part of the LabVIEW Processing Toolkit.

4.5.3 Characterization of spatial resolution

The performance of the spatial resolution performance for the upconversion microscopy is demonstrated by imaging a USAF 1951 resolution target. The resolution target is placed on the X-Y translation stage for raster scanning and illuminated by the LWIR beam at 970 cm^{-1}. The transmitted light is mixed with the 1064 nm laser for sum-frequency generation, giving an upconversion signal at 964 nm, which is detected with a silicon detector. Fig. 4.19(a) and (b) show upconversion images of the resolution target group 2 and 3, respectively. The intensity profiles across the horizontal set of bars (red/blue dashed lines) are depicted in Fig. 4.19(c) and (d), respectively. The target features are well resolved above a feature size larger than ∼35 µm, which was the smallest features in the available free path transmission target (Group 3, element 6). The decreasing intensity in Fig. 4.19(d) for finer structures reflects the narrow aperture compared to the larger illumination beam diameter, as discussed in the previous section. However, the modulation between the lines clearly shows that the lines are spatially resolved. Note that this effect is the same as illustrated numerically in Fig. 4.18.

4.5.4 Microcalcifications from an *ex vivo* sample of breast *DCIS*

The study presented here aims to develop a novel diagnostic tool for analyzing breast cancer tissue biopsies in the 1060 cm^{-1} to 830 cm^{-1} spectral range, retrieving spectral information related to the phosphate and carbonate bands. In this wavelength region, these bands do not suffer from paraffin signal attenuation. If only few wavelengths are required for the spectral analysis, discrete wavelength tuning is a time efficient approach to acquire the spectral signatures of the tissue sample under investigation, which is different from traditional FTIR systems acquiring spectral data

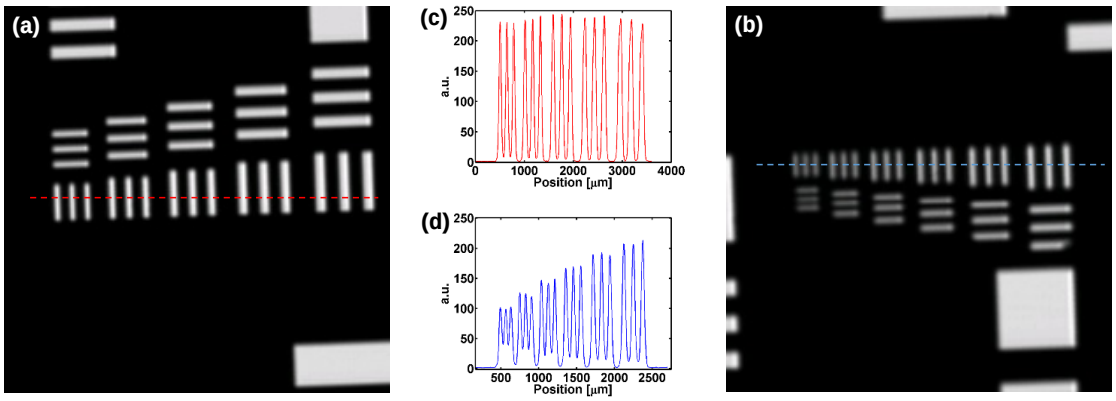

Figure 4.19: USAF 1951 optical resolution target (a) group 2, element 2 to 6 (b) group 3, element 1 to 6 imaged with the upconversion raster scanning microscopy in transmission. The images obtained at 970 cm^{-1} (10.31 µm), corresponding to an upconverted signal at 964 nm.Intensity profiles across the horizontal set of bars (red/blue dashed lines) are plotted in (c) and (d), respectively

at all wavelength at a time. Fig. 4.20(a) shows a histological section of the *DCIS* sample with H&E staining under an optical transmission microscope. An adjacent unstained section is evaluated using micro-FTIR imaging, see Fig. 4.20(b), and the upconversion raster scanning microscopy system, see Fig. 4.20(c).

The FTIR and upconverted images are obtained at the phosphate peak at 1020 cm^{-1}. The LWIR signal transmitted through the sample is upconverted from 1020 cm^{-1} into the near infrared at 964 nm and detected using a silicon detector. The area (0.5 mm^2) of the microcalcification in the biopsy sample is marked with black squares in Fig. 4.20. The acquisition time of the FTIR image with an area of 0.5 mm^2 as a single image tile of 64 averaged scans in the spectral range of 3900 cm^{-1} to 900 cm^{-1} at a spectral resolution of 4 cm^{-1}, is about 5 min. A monochromatic image of the same area can be measured in 30 s using the second generation of the upconversion imaging system. The actual acquisition time using the upconversion system mainly depends on the number of wavelengths needed to identify the microcalcifications and the desired image size. The image acquisition time is currently limited by the scan speed of the X-Y translation stage, but higher scan speed will reduce the signal-to-noise ratio as a result of reduced integration time of an individual pixel. In addition, the image quality can be improved using a LWIR beam with reduced beam diameter for the illumination. This requires good optics to focus the beam down to the size as close as possible for a given wavelength (diffraction limit). The beam profile of QCL is not perfectly round, therefore a spatial filtering e.g. a pinhole may be required for circling the beam with the subsequent expense at

losing signal strength. The beam size of the pump beam can be reduced in order to only upconvert a part of the LWIR beam giving signals from a reduced spatial area where the LWIR beam interacts with the sample.

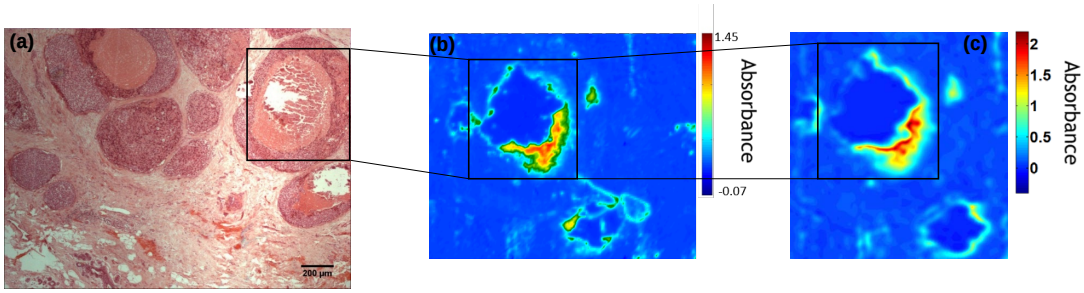

Figure 4.20: (a) Histological section of *DCIS* breast cancer microcalcifications with H&E staining imaged with an optical transmission microscope. The area marked with the black squares is $\sim$0.5 mm^2. (b) FTIR absorbance image with a size of $\sim$1.4 mm $\times$ 1.7 mm filtered around the phosphate peak at 1020 cm^{-1} (c) Upconversion absorbance image with a size of $\sim$1.3 mm $\times$ 1.2 mm obtained at 1020 cm^{-1} corresponding to an upconverted signal at 958.8 nm wavelength.

Only few discrete wavelengths are required to identify the microcalcifications via the phosphate and carbonate bands at 1020 cm^{-1} and 875 cm^{-1}, respectively. In order to map out the spectral features of the microcalcifications and compare the spectra, multispectral imaging is performed with the upconversion system and compared to spectra obtained with the Micro-FTIR system. Fig. 4.21(a) shows multispectral images obtained with the upconversion system at 1040 cm^{-1}, 1032 cm^{-1}, 1020 cm^{-1}, 1005 cm^{-1}, 970 cm^{-1}, 962 cm^{-1}, 950 cm^{-1}, 910 cm^{-1}, 881 cm^{-1}, 875 cm^{-1}, 860 cm^{-1} and 850 cm^{-1}, respectively.

The wavelength of interest is set by adjusting the QCL having a bandwidth of 1 cm^{-1} and the nonlinear crystal is rotated for optimal conversion efficiency for each wavelength [58]. Reference measurements on an empty area of the BaF_2 sample mount were performed at each wavelength for calculating of the sample absorbance. Fig. 4.21(b) shows absorbance spectra obtained using the Micro-FTIR (solid lines) and upconversion system (dots) on a region of *DCIS* (containing a microcalcification), and Fig. 4.21(c) shows the corresponding absorbance spectra measured in an area of non-cancerous connective tissue (not containing calcifications). The FTIR system becomes noisy in the LWIR regime below 900 cm^{-1}, resulting in spectral artefacts. The upconverted absorbance is retrieved from the series of images shown in Fig. 4.21(a) and extracted from an area where the phosphate band is highly absorbing (pink arrow) and from surrounding tissue (orange arrow). A significant increase in absorbance (peak at $\sim$1.3) is seen at the phosphate absorption band in the micro-

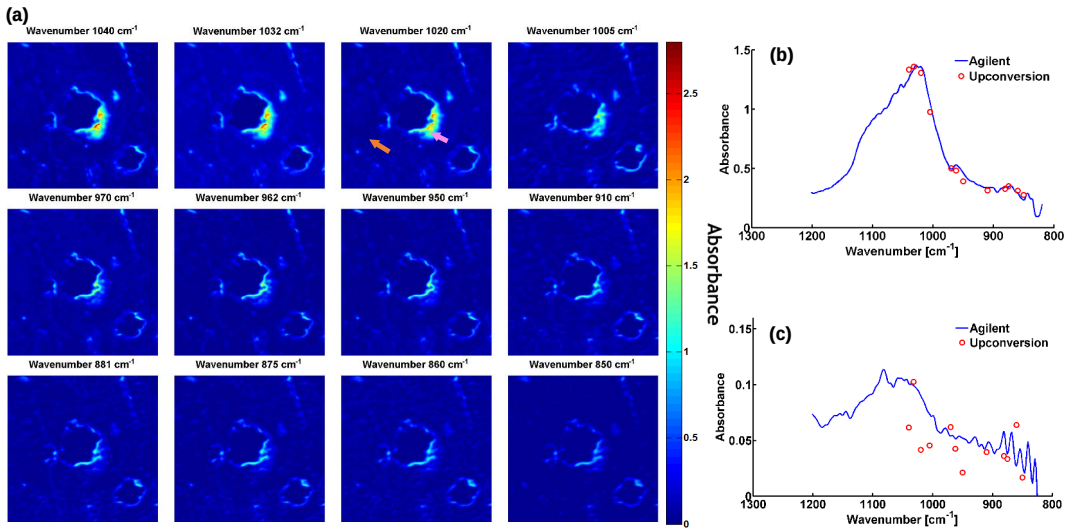

Figure 4.21: (a) Multispectral upconversion images of the *DCIS* breast cancer microcalcifications obtained at 1040 cm^{-1}, 1032 cm^{-1}, 1020 cm^{-1}, 1005 cm^{-1}, 970 cm^{-1}, 962 cm^{-1}, 950 cm^{-1}, 910 cm^{-1}, 881 cm^{-1}, 875 cm^{-1}, 860 cm^{-1} and 850 cm^{-1} respectively, corresponding to upconverted signals in the wavelength range of 958 nm to 976 nm. Spectra measured using the Micro-FTIR and upconversion system from (b) a microcalcification area (pink arrow) and (c) surrounding tissue (orange arrow). Note the different absorbance scales in (b) and (c).

calcification area (pink arrow) compared to the surrounding. The carbonate peak can be also seen around 875 cm^{-1}. The upconverted spectrum shows a good agreement with the FTIR spectrum. Generally, upconversion detector could measure LWIR signal at low signal levels (high absorbance) due to the very low dark noise in the Si detector [59, 60]. This is very pertinent to the highly absorbing breast calcifications and may allow for the use of thicker samples and still maintain a sufficient contrast.

4.5.5 Conclusion

We demonstrate that breast cancer tissues can be analyzed using the upconversion raster scanning microscopy system without the use of exogenous staining. The use of upconversion can enable fast image acquisition compared to FTIR microscopic imaging through the use of silicon detectors, potentially improving speed and the signal-to noise ratio at low cost and without the need for cryogenic cooling. The presented result shows excellent agreement between upconversion raster scanning microscopy and Micro-FTIR imaging in terms of imaging and spectral features of breast microcalcifications. Discrete wavelength turning to only relevant wavelengths with the biggest discrimination factor can substantially reduce the acquisition time. This new approach has the potential to measure fresh tissue samples without the

need for exogenous staining and with a significantly improved speed over Micro-FTIR imaging. We also measured 14 breast cancer biopsies at different stages of benign, *DCIS*, and invasive ductal carcinoma (*IDC*) using both the commercial Micro-FTIR system and the upconversion imaging system. The analysis of the data from both systems (data cubes of spectrally resolved images) is the subject of currently ongoing research.

Chapter 5

Preliminary study of a self-referencing system

This chapter reports the experimental implementation of a self-referencing system for noise reduction, promising to improve the sensitivity and stability of the LWIR detection. The system is capable of being used in upconversion-based systems.

5.1 Motivation

The self-referencing system was developed with the aim of noise reduction for the LWIR detection. The approach is to split the LWIR beam into two parts and use one of them as the common-mode signal (reference) to remove the noise from the other (signal), which passes through the target under test and contains the information about the sample, e.g. a biological sample or a gas sample. Here, we perform a preliminary correlation analysis of both LWIR beams without a sample present.

5.2 Experimental setup

Fig. 5.1 shows the schematic layout of the self-referencing system for the LWIR detection, consisting of a QCL source, a pump source, a nonlinear crystal, and a silicon detector as the key components. The LWIR beam is split into two parts via a beam-splitter (70 % transmission, 30 % reflection, nominal). Both beams are parallelly displaced and impinge on a 90° off-axis parabolic mirror at an equal distance to its center where a hole was drilled. Both beam are focused by the parabolic mirror into the $AgGaS_2$ crystal at equal incident angles to the surface normal of the nonlinear crystal. The hole at the center of the 90° off-axis parabolic mirror is 3 mm in diameter and the focal length is 25.4 cm. The pump beam passes through the

3 mm-hole into the 5 mm × 5 mm × 10 mm $AgGaS_2$ crystal with a cutting angle of 43.3°. Both separated LWIR beams are mixed with the pump beam inside the $AgGaS_2$ crystal for sum-frequency generation in which the upconverted signals are acquired by a silicon CCD (uEye, IDS) camera. The pump source is a master oscillator power amplifier (MOPA) semiconductor laser operating in a continuous-wave mode, delivering up to 3 W of output power.

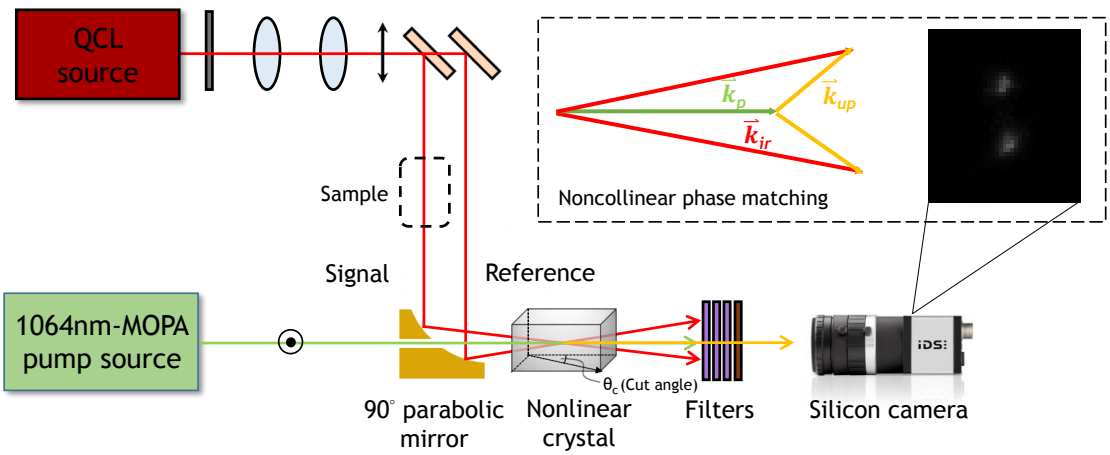

Figure 5.1: Schematic layout of the self-referencing system for the LWIR detection. Type II non-collinear phase matching is used here. The sample is not present in the self-referencing measurement.

The Fig. 5.2 shows the experimental setup of the self-referencing system.

5.3 Results

The reference and the signal beams at a wavelength of 10.25 µm are upconverted to the NIR at 963.9 nm using type II non-collinear phase-matching configuration (see Fig. 5.1) in which the LWIR and the pump beams are polarized extraordinarily and ordinarily, respectively, and crossed inside the crystal at an angle. Fig. 5.3 shows the phase-matching wavelength tuning curves of the signal and the reference in which the upconverted signals are acquired using the silicon camera for each wavelength.

The obtained upconverted intensities are normalized to account for the different powers of both LWIR beams due to the 70/30 splitter. The result shows that both LWIR beams at a wavelength of 10.25 µm are upconverted to NIR at 963.9 nm with a similar conversion efficiency. The curves for the reference (green) and signal (blue) beams are not perfectly overlapping due to imperfect optical alignment of the off-axis parabolic mirror and thus slightly different incidence angles for both LWIR beams. Accurate alignment of the LWIR beams is challenging, since they

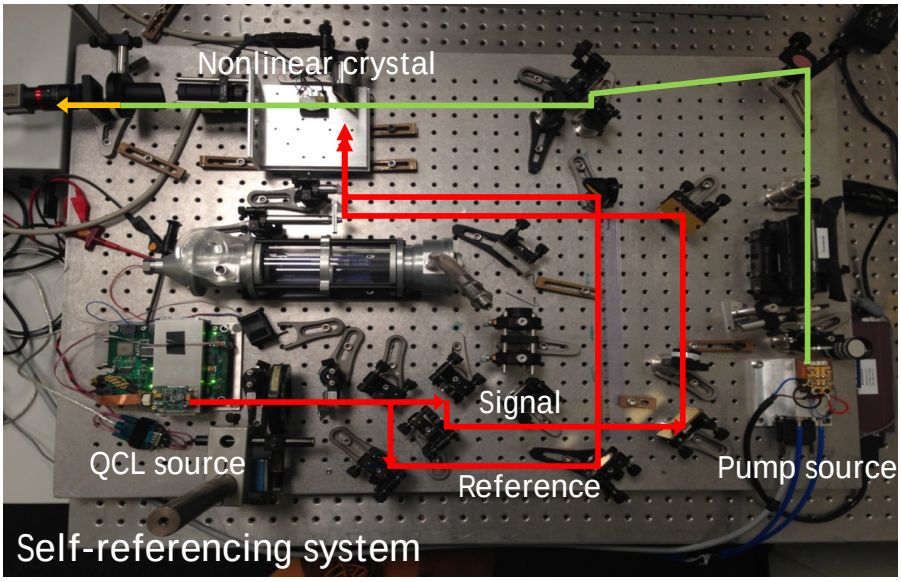

Figure 5.2: Photograph of the self-referencing system for LWIR detection in the laboratory.

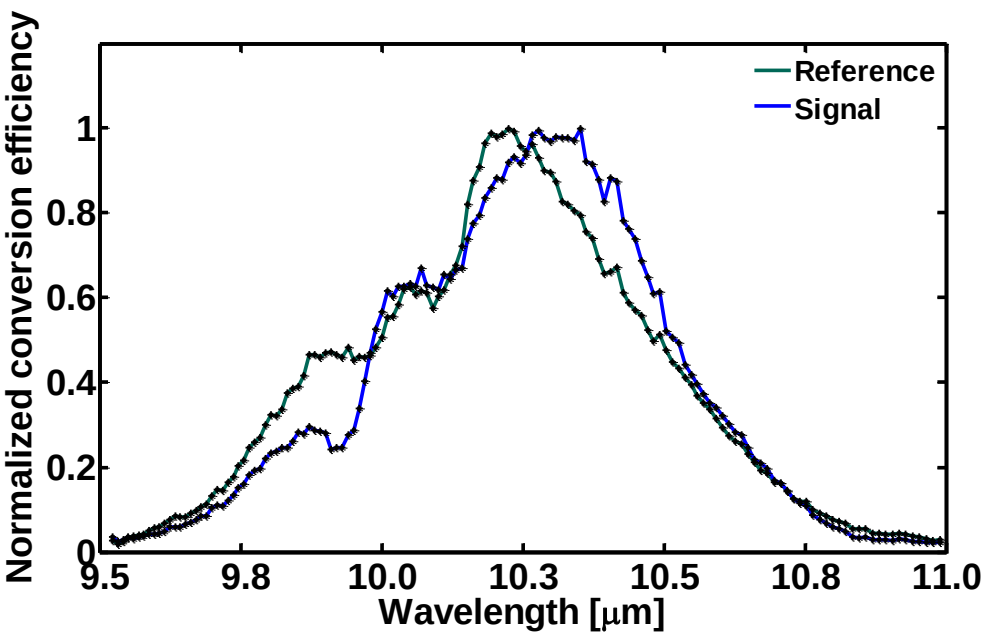

Figure 5.3: Phase-matching wavelength tuning curves of the signal and reference beams for sum-frequency generation. The crystal rotation angle is fixed at $-2.3°$.

are invisible to regular IR detector cards and can only be visualized by much less sensitive thermal detector cards, which convert the optical power of the beam into the heat resulting in a color changes. This is due to a lack of florescent phosphor for converting LWIR to visible. The slightly different conversion efficiency due to imperfect alignment (Fig. 5.3) does not affect the correlation analysis but it might introduce a systematic error when used as a reference for absorbance measurements of actual samples if not corrected. Thus, a power calibration of the upconverted reference beam can be performed at each wavelength, correcting for the systematic error due to imperfect alignment. The corrected reference intensity can then be used for referencing the signal beam during measurements in order to eliminate power fluctuations via post-processing.

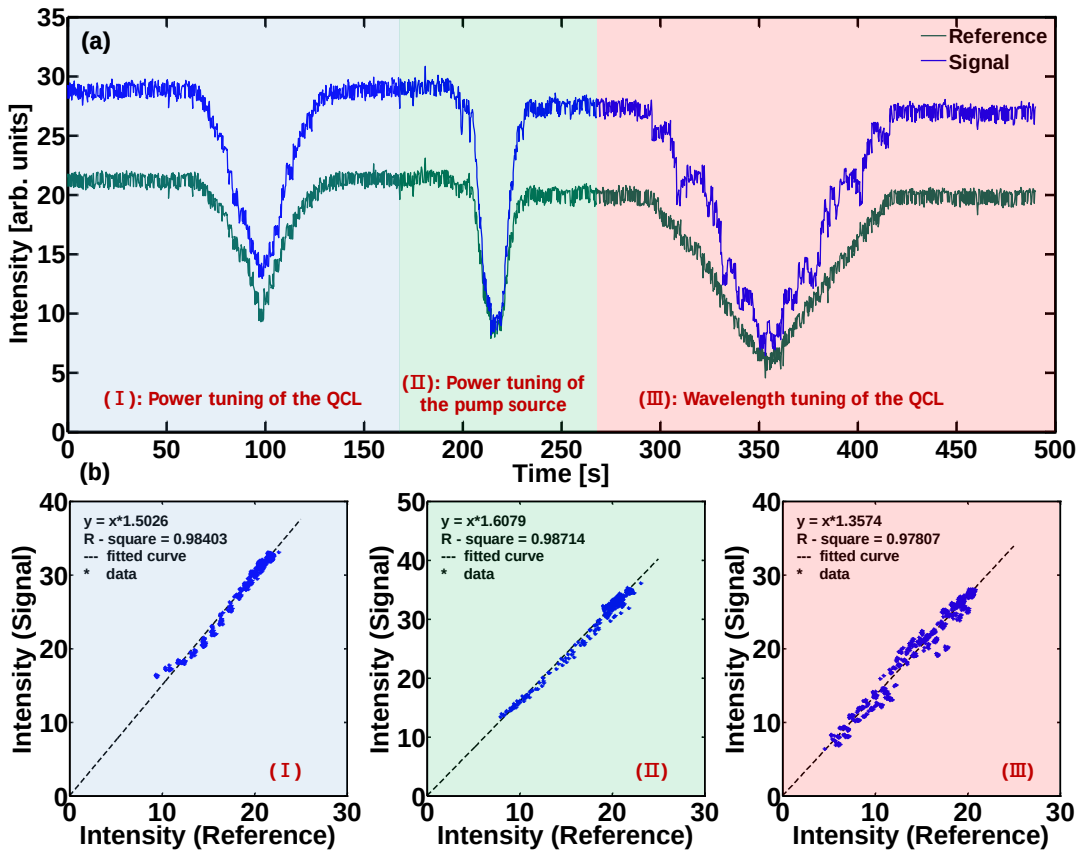

Figure 5.4: (a) Modulated intensities of the signal (blue curve) and the reference (green curve) beams during (I) power tuning of the QCL, (II) power tuning of the pump source, and (III) wavelength tuning of the QCL, respectively. (b) Correlations between the signal and the reference corresponding to (I), (II), and (III), respectively, where the intensities of both beams are plotted against each other. The dashed black lines show offset-free linear fits.

In order to quantify how well intensity fluctuations of the signal beam are reproduced by the reference beam and thus the potential noise reduction by the self-referencing scheme, the intensity correlation between both beams is investigated. An intensity modulation is imposed on both the signal and the reference beam by varying the power of the QCL source, the power of the pump source, and the wavelength of the QCL source, respectively. Fig. 5.4(a) shows the modulated intensities of the signal (blue curve) and the reference (green curve) during (I) power tuning of the QCL, (II) power tuning of the pump source, and (III) wavelength tuning of the QCL, respectively. Fig. 5.4(b) shows correlations between the signal and the reference in which the intensities of both beams are plotted against each other. The correlations are linearly fitted (offset-free) and the corresponding high R-squared values indicate a high degree of correlation. This result is very promising for the implementation of noise reduction using this self-referencing system by removing the common-mode noise (obtained from the reference) from the signal used for measurements.

5.4 Potential application using the self-referencing system

Furthermore, the self-referencing system can be combined with an upconversion gas spectroscopy system for gas monitoring, e.g. trichloroethylene (TCE) and tetrachloroethylene (PCE). Nowadays, the TCE and PCE is monitored using passive samples (tubes) on the site which requires long sampling time (weeks) to measure low concentration of gas-phase pollutants. After sampling, the absorbed analyzes is then analyzed in the lab to evaluate the contaminant concentration. However the variations of the concentrations of TCE and PCE occur over time, and these variations cannot be monitored due to the long sampling time. The upconversion gas spectroscopy has been developed for concentration measurement of TCE and PCE in real time, allowing for efficient data acquisition of air pollutant over time. The improved sampling time would allow to localize these substances and find the their penetration pathway for a better understanding of exposure patterns.

Fig. 5.5 illustrates the upconversion gas spectroscopy system which was built by our formal group member [61]. The system includes a LWIR source (QCL), a pump source (MOPA), an upconversion detector allowing for LWIR detection using a Si-based camera, and a multi-pass Herriott cell, giving a total interaction length of 36 m allowing to measure low-concentration components. Combining the self-referencing method with the gas system can potentially improve signal-to-noise ratio, hopefully to be able to measure a gas sample down to the ppb (part per billion) level.

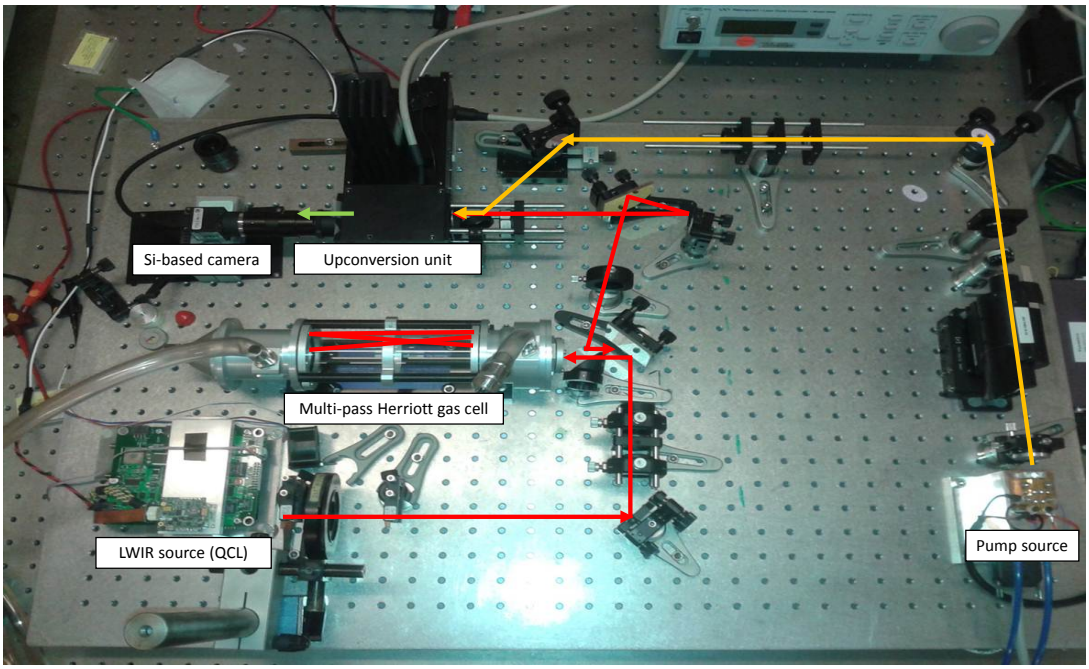

Figure 5.5: Photograph of the upconversion gas spectroscopy, including a LWIR source, a pump source, an upconversion detector allowing for LWIR detection using a Si-based camera, and a multi-pass Herriott cell for gas monitoring in the laboratory.

5.5 Conclusion

The implementation of the self-referencing system with the purpose of noise reduction for the LWIR upconversion detection was investigated in this chapter. Excellent correlation (high R-squared) between the signal and the reference was found, allowing for improvement of the signal-to-noise ratio by removing the common-mode noise from the signal using the reference beam. The concept of the self-referencing system can be readily implemented in various upconversion-based systems, in particular the upconversion raster scanning microscopy imaging system presented in chapter 4 or upconversion spectroscopy capable of detecting indoor environmental contaminants [61], such as organic compounds (TCE and PCE). The results of this work pave the way for implementing low-noise upconversion detection schemes.

Chapter 6

Summary and conclusions

6.1 Summary of the thesis

In this thesis, a LWIR upconversion detector was investigated, combined with a tunable QCL source and a microscopy unit it was implement as a raster scanning upconversion microscopy system, enabling label-free spectral imaging of *DCIS* breast cancer biopsies. The upconversion detector was shown to be able to convert LWIR (9.4 µm to 12 µm) to NIR (956 nm to 977 nm) signals, promising an improvement of acquisition speed and signal-to-noise ratio. A numerical model was presented, showing excellent agreement with measured data in terms of both conversion efficiency and acceptance parameters. The model takes into account the finite beam size, diffraction and absorption of the infrared signal in the nonlinear crystal, as well as the angular dependence of the refractive index. This allows to accurately model the performance of the upconversion detector before its implementation.

The raster scanning upconversion microscopy imaging system was shown to be able to identify *DCIS* breast cancer microcalcifications. The imaging system is capable of providing chemical images with wavenumbers below 900 cm^{-1} required to identify carbonate substitution of HAP in microcalcifications as a biomarker for the progression of the breast cancer disease. Detection of LWIR signals below 900 cm^{-1} using a regular FTIR system is unreliable due to unavoidable dark noise originating from the finite temperature of the LWIR detector. In contrast to a FTIR system, which acquires full spectra, the laser-based upconversion imaging system using a QCL source enables discrete wavelength turning across the spectral range containing the biomedical features of interest. Therefore, only few wavelengths are required, e.g. covering a narrow range around the phosphate (1020 cm^{-1}) and carbonate (875 cm^{-1}) bands, for the identification of breast cancer microcalcifications. A comparison between the upconversion imaging system and a commercial Micro-

FTIR system shows excellent agreement in terms of the spatial distribution and the spectral features of the microcalcifications. The use of upconversion presents an alternative for the LWIR detection, promising a fast acquisition speed and a good signal-to-noise ratio using silicon-based detectors. We also measured 14 breast cancer biopsies at different stages of benign, *DCIS*, and invasive ductal carcinoma (*IDC*) using both the commercial Micro-FTIR system and the upconversion imaging system. The analysis of the data from both systems (data cubes of spectrally resolved images) is the subject of currently ongoing research.

The implementation of a self-referencing system with the purpose of noise reduction for the LWIR detection was investigated, showing its potential for intensity correlation between the signal and the reference. This results demonstrates its potential to improve the signal-to-noise ratio by removing the common mode noise from the signal using the reference beam, paving the way for implementing low-noise upconversion detection schemes.

6.2 Outlook for future work

To extend the work shown in chapter 3, the detection wavelength range of LWIR can be expanded further from 12 µm to ∼18 µm by using an $AgGaSe_2$ as the nonlinear crystal for upconversion detection. Longer wave spectroscopy may find future applications within gas sensing. Polychlorinated biphenyls (PCBs) was used in building materials e.g. elastic material, between ∼1960 to 1975 and has been reported as one of toxic indoor contaminants. This substance needs to be monitored in order to maintain total PCB exposure below the reference dose, the maximum acceptable oral dose of a toxic substance [62]. PCBs has IR spectral features above the wavelength range of ∼13 µm [63].

$AgGaSe_2$ crystals has good transparency, e.g. ∼95 % transmission at a wavelength of 12 µm in contrast a $AgGaS_2$ crystal, which has only ∼10 % transmission at 12 µm, meaning that most of the LWIR power is absorbed by the crystal and does not contribute to the frequency conversion process. A 1.9 µm pump source is required for the phase-matching process due to the dispersion of the $AgGaSe_2$ nonlinear crystal, where e.g. a 12 µm LWIR signal mixed with a 1.9 µm pump signal can be upconverted to 1640 nm and acquired by a InGaAs camera. This configuration can be implemented by using the current QCL source (shown in chapter 3) and a 1.9 µm pump source, which is currently being built in our group [64], for sum-frequency generation. Globar can also be used as a LWIR source for testing this configuration, as was demonstrated in a concurrent masters project.

The raster-scanning upconversion microscope imaging system can be improved by optimizing the optical setup. Tight focusing achromatic objective lenses can be

used to reduce the spot size of the LWIR beam on the biological sample, improving the spatial resolution of the images. In addition, a comparison of the SNR using e.g. a single-point MCT detector and a silicon-based detector can be made to quantify the improved SNR performance of the upconversion detector over a direct LWIR detector. The scan speed of the X-Y translation stage (7 mm/s) is the maximum speed of the current stage) can be improved using an advanced translation stage which can move faster. Acquisition during a high-speed movement of the stage results in less integration time at each pixel (the integration time at each pixel depends on the speed of the stage movement), therefore the potential reduction of the SNR needs to be considered when measuring at higher speeds, which constitutes a trade-off between SNR and acquisition time. This imaging system can be also combined with a supercontinuum laser as the infrared illumination source for hyperspectral imaging, and even allows using different scanning patterns, e.g. a spiral pattern, reducing the data acquisition time. Due to the use of a sensitive silicon detector for LWIR detection, it would be interesting to measure thinly cut frozen fresh tissue without the need for paraffin processing (and thus signal contamination with paraffin signatures) and exogenous staining with the aim of fast diagnosis of the biopsies.

A further analysis of the self-referencing system including appropriate upconversion modeling will allow identifying and compensating for different noise contributions from different parts of the system, e.g. intensity fluctuations of the QCL/pump sources or wavelength drift of the QCL. This system can be further combined with upconversion spectroscopy for gas detection, potentially providing significantly better SNR and thus enabling the concentration measurement of a gas sample down to the ppb (part per billion) level.

Appendix

In this appendix, we illustrate the derivation of the upconverted electric field including beam diffraction for both the pump and signal beams. Refer to Fig. 2.5 for the coordinate system and naming convention. The upconverted electric field based on the Green function approach [29, 32, 58] is given by:

$$E_{up}(r_{uv}, \boldsymbol{k_{up}}) \equiv \frac{\exp(-ik_{up}r_{uv})}{4\pi r_{uv}} \int_V S_{up}(\boldsymbol{r'}) \exp(i\boldsymbol{k_{up}} \cdot \boldsymbol{r'}) dr' \tag{6.1}$$

where $r_{uv} = |\boldsymbol{r_{uv}}|$ is a distance between the source point and the far field observation point. The source term, $S_{up}(\boldsymbol{r'})$, for a $\chi^{(2)}$ nonlinear process is given by

$$S_{up}(\boldsymbol{r'}) = -\mu_0 \frac{\partial^2 P_{up}}{\partial^2 t} = \frac{2d_{eff}\omega_{up}^2}{c^2} E_p(\boldsymbol{r'}) E_{ir}(\boldsymbol{r'}) e^{-i(\boldsymbol{k_{ir}}+\boldsymbol{k_p})\cdot\boldsymbol{r'}} \tag{6.2}$$

where d_{eff} is the effective nonlinear coefficient to be calculated in terms of the polarization states of the interacting fields and geometry of the nonlinear medium regarding to crystal class. P_{up} is polarization density of the upconverted field, given by

$$P_{up} = 2\epsilon_0 d_{eff} E_p(\boldsymbol{r'}) E_{ir}(\boldsymbol{r'}) e^{-i(\boldsymbol{k_{ir}}+\boldsymbol{k_p})\cdot\boldsymbol{r'}} e^{i(\omega_{ir}+\omega_p)t} \tag{6.3}$$

where $w_{ir} + w_p = w_{up}$, $E_p(\boldsymbol{r'})$ and $E_{ir}(\boldsymbol{r'})$ are the pump (p) and LWIR (ir) fields, respectively. $E_p(\boldsymbol{r'})$ and $E_{ir}(\boldsymbol{r'})$ are given by

$$E_p(\boldsymbol{r'}) \exp(-ik_{pz}z) = \frac{E_p}{1 + i\frac{z}{z_{Rp}}} \exp(-ik_{pz}z) \exp\left\{-\frac{x^2+y^2}{W_p^2(1+i\frac{z}{z_{Rp}})}\right\} \tag{6.4}$$

$$E_{ir}(\boldsymbol{r'}) \exp(-ik_{irz}z) = \frac{E_{ir}}{1 + i\frac{z}{z_{Rir}}} \exp(-ik_{irz}z) \exp\left\{-\frac{x^2+y^2}{W_{ir}^2(1+i\frac{z}{z_{Rir}})}\right\} \tag{6.5}$$

where W_{ir} and W_p are the beam waists, $z_{R_{ir}}$ and z_{R_p} are the Rayleigh lengths and k_{irz} and k_{pz} are the wave vectors of the LWIR and pump fields (in z direction), respectively. Substituting Eqn (6.4) and Eqn (6.5) into Eqn (6.1), we obtains

$$E_{up}(r_{uv}, \boldsymbol{k_{up}}) = 2\frac{d_{eff}\omega_{up}^2}{4\pi c^2}E_{ir}E_p\frac{e^{-i\boldsymbol{k_{up}}\cdot\boldsymbol{r_{uv}}}}{r_{uv}}\int_z\int_y\int_x\frac{1}{(1+i\frac{z}{z_{Rir}})(1+i\frac{z}{z_{Rp}})}\times$$

$$\exp\left\{-\frac{x^2+y^2}{W_{ir}^2(1+i\frac{z}{z_{Rir}})}\right\}\exp\left\{-\frac{x^2+y^2}{W_p^2(1+i\frac{z}{z_{Rp}})}\right\}\times \tag{6.6}$$

$$\exp\{i\boldsymbol{k_{up}}\cdot\boldsymbol{r'}\}\exp\{-i(k_{irz}+k_{pz})z\}dxdydz$$

where the effective value of the nonlinear coefficient (d_{eff}) is calculated in terms of the directions of E_p and E_{ir} fields and the nonzero values of the nonlinear susceptibility tensor regarding to crystal class. Using $z_{R_{ir}} = \pi n_{ir}W_{ir}^2/\lambda_{ir}$, $z_{R_p} = \pi n_p W_p^2/\lambda_p$, and $e^{i\boldsymbol{k_{up}}\cdot\boldsymbol{r'}} = e^{ik_{upx}x}e^{ik_{upy}y}e^{ik_{upz}z}$, we can rewrite Eqn (6.6) as

$$E_{up}(r_{uv}, \boldsymbol{k_{up}}) = 2\frac{d_{eff}\omega_{up}^2}{4\pi c^2}E_{ir}E_p\frac{e^{-i\boldsymbol{k_{up}}\cdot\boldsymbol{r_{uv}}}\int_z}{r_{uv}}\int_y\int_x\frac{W_{ir}^2W_p^2}{(W_{ir}^2+i\frac{\lambda_{ir}z}{\pi n_{ir}})(W_p^2+i\frac{\lambda_p z}{\pi n_p})}\times$$

$$\exp\left\{-\frac{x^2+y^2}{W_{ir}^2+i\frac{\lambda_{ir}z}{\pi n_{ir}}}\right\}\exp\left\{-\frac{x^2+y^2}{W_p^2+i\frac{\lambda_p z}{\pi n_p}}\right\}e^{ik_{upx}x}\ e^{ik_{upy}y}\ e^{i\Delta k_z z}\ dxdydz \tag{6.7}$$

with $\Delta k_z = k_{upz} - k_{irz} - k_{pz}$. Substituting

$$W_{ir}^2 + i\frac{\lambda_p z}{\pi n_{ir}} = S, \quad W_p^2 + i\frac{\lambda_{pz}}{\pi n_p} = P,$$

into Eqn (6.7), we obtains

$$E_{up}(r_{uv}, \boldsymbol{k_{up}}) = 2\frac{d_{eff}\omega_{up}^2}{4\pi c^2}E_{ir}E_p\frac{e^{-i\boldsymbol{k_{up}}\cdot\boldsymbol{r_{uv}}}}{r_{uv}}\int_z\frac{W_{ir}^2W_p^2}{SP}e^{i\Delta k_z z}\times$$

$$\int_y\exp\left\{-\frac{S+P}{SP}y^2\right\}e^{ik_{upy}y}dy\int_x\exp\left\{-\frac{S+P}{SP}x^2\right\}e^{ik_{upx}x}dx \tag{6.8}$$

Next, we use the following Fourier transform identity

$$\int_{-\infty}^{\infty} e^{-\alpha x^2} e^{ik_x x} dx = \sqrt{\frac{\pi}{\alpha}} \exp\left\{-\frac{k_x^2}{4\alpha}\right\} \tag{6.9}$$

and substitute $\alpha = \frac{S+P}{SP}$ in the corresponding integral terms in Eqn (6.9):

$$\int_y \exp\left\{-\frac{S+P}{SP} y^2\right\} e^{ik_{upy} y} dy = \sqrt{\frac{\pi SP}{S+P}} \exp\left\{-\frac{k_{upy}^2}{4} \frac{SP}{S+P}\right\},$$

$$\int_x \exp\left\{-\frac{S+P}{SP} x^2\right\} e^{ik_{upx} x} dx = \sqrt{\frac{\pi SP}{S+P}} \exp\left\{-\frac{k_{upx}^2}{4} \frac{SP}{S+P}\right\},$$

which simplifies Eqn (6.8) to:

$$E_{up}(r_{uv}, \boldsymbol{k_{up}}) = 2\frac{d_{eff}\omega_{up}^2}{4\pi c^2} E_{ir} E_p \frac{e^{-i\boldsymbol{k_{up}}\cdot\boldsymbol{r_{uv}}}}{r_{uv}} \int_z \frac{W_{ir}^2 W_p^2}{SP} \sqrt{\frac{\pi SP}{S+P}} \sqrt{\frac{\pi SP}{S+P}} \times$$
$$\exp\left\{-\frac{1}{4}\frac{SP}{S+P}(k_{upx}^2 + k_{upy}^2)\right\} e^{i\Delta k_z z} dz \tag{6.10}$$

Since upconversion is only efficient at small phase mismatch status, we replace k_{upx} and k_{upy} with phase mismatch terms Δk_u in x direction and Δk_v in y direction, respectively, and use $\omega_{up} = \frac{2\pi c}{\lambda_{up}}$ to obtain

$$E_{up}(r_{uv}, \Delta k_u, \Delta k_v, \Delta k_z) = 2\frac{d_{eff}\pi^2}{\lambda_{up}^2} \sqrt{\frac{2}{c\epsilon_0 n_{ir}} \frac{2P_{ir}}{\pi W_{ir}^2}} \sqrt{\frac{2}{c\epsilon_0 n_p} \frac{2P_p}{\pi W_p^2}} \frac{e^{-i\boldsymbol{k_{up}}\cdot\boldsymbol{r_{uv}}}}{r_{uv}} \int_z \frac{W_{ir}^2 W_p^2}{S+P}$$
$$\exp\left\{-\frac{1}{4}\frac{SP}{S+P}(\Delta k_u^2 + \Delta k_v^2)\right\} e^{i\Delta k_z z} dz \tag{6.11}$$

where we used the definition of the intensity $I_{(ir,p)}$ to replace the electric field amplitudes in Eqn (6.8) with the respective powers:

$$I_{(ir,p)} = \frac{c\epsilon_0 n_{(ir,p)}}{2} |E_{(ir,p)}|^2 = \frac{2P_{(ir,p)}}{\pi W_{(ir,p)}}$$

After simplifying Eqn (6.10), transforming it into the (u, v) polar coordinate system and inserting the absorption term with α_{ir} being the absorption constant for the upconverted radiation and l the crystal length, we obtain:

$$E_{up}(r_{uv}, \Delta k_u, \Delta k_v, \Delta k_z) = 4\frac{d_{eff}\pi^2}{c\epsilon_0\lambda_{up}^2}\sqrt{\frac{2P_{ir}}{n_{ir}\pi W_{ir}^2}}\sqrt{\frac{2P_p}{n_p\pi W_p^2}}\frac{e^{-i\boldsymbol{k_{up}}\cdot\boldsymbol{r_{uv}}}}{r_{uv}}\int_z \frac{W_{ir}^2 W_p^2}{S+P}\times$$

$$\exp\left\{-\frac{1}{4}\frac{SP}{S+P}(\Delta k_u^2 + \Delta k_v^2)\right\}\exp\left\{-\frac{\alpha_{ir}}{2}\left(z+\frac{l}{2}\right)\right\}e^{i\Delta k_z z}dz \tag{6.12}$$

Finally, we substitute S and P back into Eqn (6.12) and set the integration limits to the crystal length:

$$E_{up}(r_{uv}, \Delta k_u, \Delta k_u, \Delta k_z) = \frac{4d_{eff}\pi^2}{c\epsilon_0\lambda_{up}^2}\sqrt{\frac{2P_{ir}}{n_s\pi W_{ir}^2}}\sqrt{\frac{2P_p}{n_p\pi W_p^2}}\frac{e^{-i\boldsymbol{k_{up}}\cdot\boldsymbol{r_{uv}}}}{r_{uv}}\times$$

$$\int_{-\frac{l}{2}}^{\frac{l}{2}}\frac{W_{ir}^2 W_p^2}{W_{ir}^2 + W_p^2 + i\frac{\lambda_s z}{\pi n_{ir}} + i\frac{\lambda_p z}{\pi n_p}}\exp\left\{-\frac{1}{4}\frac{(W_{ir}^2 + i\frac{\lambda_{ir} z}{\pi n_{ir}})(W_p^2 + i\frac{\lambda_p z}{\pi n_p})}{W_{ir}^2 + W_p^2 + i\frac{\lambda_{ir} z}{\pi n_{ir}} + i\frac{\lambda_p z}{\pi n_p}}(\Delta k_u^2 + \Delta k_u^2)\right\}\times$$

$$\exp\left\{-\frac{\alpha_{ir}}{2}\left(z+\frac{l}{2}\right)\right\}e^{i\Delta k_z z}dz \tag{6.13}$$

The total upconverted power can be obtained by integrating the square of the upconverted field E_{up} given by Eqn (6.13) along both u and v angles:

$$P_{up} = \frac{c\epsilon_0 n_{up}}{2}\int_u\int_v |E_{up}(u, v, r_{uv})|^2 r_{uv}^2 du dv \tag{6.14}$$

Bibliography

[1] E. Normand, M. McCulloch, G. Duxbury, and N. Langford. *Fast, real-time spectrometer based on a pulsed quantum-cascade laser*. Optics letters **28**, 16–18 (2003).

[2] D. D. Nelson, B. McManus, S. Urbanski, S. Herndon, and M. S. Zahniser. *High precision measurements of atmospheric nitrous oxide and methane using thermoelectrically cooled mid-infrared quantum cascade lasers and detectors*. Spectrochimica Acta - Part A: Molecular and Biomolecular Spectroscopy **60**, 3325–3335 (2004).

[3] M. Imaki and T. Kobayashi. *Infrared frequency upconverter for high-sensitivity imaging of gas plumes*. Optics letters **32**, 1923–1925 (2007).

[4] P. Tidemand-Lichtenberg, J. S. Dam, H. V. Andersen, L. Høgstedt, and C. Pedersen. *Mid-infrared upconversion spectroscopy*. Journal of the Optical Society of America B **33**, D28 (2016).

[5] R. W. Boyd and C. H. Townes. *An infrared upconverter for astronomical imaging*. Applied Physics Letters **31**, 440–442 (1977).

[6] M. R. Kole, R. K. Reddy, M. V. Schulmerich, M. K. Gelber, and R. Bhargava. *Discrete Frequency Infrared Microspectroscopy and Imaging with a Tunable Quantum Cascade Laser*. Analytical Chemistry **84**, 10366–10372 (2012).

[7] N. Kröger, A. Egl, M. Engel, N. Gretz, K. Haase, I. Herpich, B. Kränzlin, S. Neudecker, A. Pucci, A. Schönhals, J. Vogt, and W. Petrich. *Quantum cascade laser–based hyperspectral imaging of biological tissue*. Journal of Biomedical Optics **19**, 111607 (2014).

[8] K. Yeh, S. Kenkel, J.-n. Liu, and R. Bhargava. *Fast Infrared Chemical Imaging with a Quantum Cascade Laser Fast Infrared Chemical Imaging with a Quantum Cascade Laser*. Analytical Chemistry **87**, 485–493 (2015).

[9] Z. W. Sun, Z. S. Li, B. Li, M. Aldén, and P. Ewart. *Detection of C2H2and HCl using mid-infrared degenerate four-wave mixing with stable beam alignment: Towards practical in situ sensing of trace molecular species*. Applied Physics B: Lasers and Optics **98**, 593–600 (2010).

[10] P. Ciais, C. Sabine, G. Bala, L. Bopp, V. Brovkin, J. Canadell, a. Chhabra, R. DeFries, J. Galloway, M. Heimann, C. Jones, C. Le Quéré, R. B. Myneni, S. Piao, and P. Thornton. *6SM. Carbon and Other Biogeochemical Cycles*. Climate Change 2013: The Physical Science Basis. Contribution of Working Group I to the Fifth Assessment Report of the Intergovernmental Panel on Climate Change, 6–9 (2013).

[11] Y. Saalberg and M. Wolff. *VOC breath biomarkers in lung cancer*. Clinica Chimica Acta **459**, 5–9 (2016).

[12] E. van Mastrigt, a. Reyes-Reyes, K. Brand, N. Bhattacharya, H. P. Urbach, a. P. Stubbs, J. C. de Jongste, and M. W. Pijnenburg. *Exhaled breath profiling using broadband quantum cascade laser-based spectroscopy in healthy children and children with asthma and cystic fibrosis*. Journal of breath research **10**, 026003 (2016).

[13] T. Stacewicz, Z. Bielecki, J. Wojtas, P. Magryta, J. Mikolajczyk, Szabra, and D. *Detection of disease markers in human breath with laser absorption spectroscopy*. Opto-Electronics Review **24**, 82–94 (2016).

[14] R. Baker, K. D. Rogers, N. Shepherd, and N. Stone. *New relationships between breast microcalcifications and cancer*. British Journal of Cancer **103**, 1034–1039 (2010).

[15] S. Chaitanya Kumar, P. G. Schunemann, K. T. Zawilski, and M. Ebrahim-Zadeh. *Advances in ultrafast optical parametric sources for the mid-infrared based on CdSiP_2*. Journal of the Optical Society of America B **33**, D44 (2016).

[16] A. Hugi, R. Terazzi, Y. Bonetti, A. Wittmann, M. Fischer, M. Beck, J. Faist, Gini, and E. *External cavity quantum cascade laser tunable from 7.6 to 11.4 μm*. **2834**, 2007–2010 (2009).

[17] *Optical detection systems*. https://www.newport.com/n/optical-detection-systems.

[18] M. M. FEJER, G. A. MAGEL, D. H. JUNDT, and R. L. BYER. *Quasi-Phase-Matched 2Nd Harmonic-Generation - Tuning and Tolerances*. Ieee Journal of Quantum Electronics **28**, 2631–2654 (1992).

[19] L. Høgstedt, A. Fix, M. Wirth, C. Pedersen, and P. Tidemand-lichtenberg. *Upconversion-based lidar measurements of atmospheric CO2*. **24**, 1579–1582 (2016).

[20] J. S. Dam, P. Tidemand-Lichtenberg, and C. Pedersen. *Room-temperature mid-infrared single-photon spectral imaging*. Nature Photonics **6**, 788–793 (2012).

[21] G. Temporão, S. Tanzilli, H. Zbinden, N. Gisin, T. Aellen, M. Giovannini, and J. Faist. *Mid-infrared single-photon counting*. Optics Letters **31**, 1094 (2006).

[22] K. Karstad, A. Stefanov, M. Wegmuller, H. Zbinden, N. Gisin, T. Aellen, M. Beck, and J. Faist. *Detection of mid-IR radiation by sum frequency generation for free space optical communication*. Optics and Lasers in Engineering **43**, 537–544 (2005).

[23] J.-J. Zondy. *The effects of focusing in type-I and type-II difference-frequency generations*. Opt. Commun. **149**, 181–206 (1998).

[24] G. C. BHAR, S. DAS, and P. K. DATTA. *Tangentially Phase-Matched Infrared Detection in AgGaS2*. Journal of Physics D-Applied Physics **27**, 228–230 (1994).

[25] S. A. Andreev, I. N. Matveev, I. P. Nekrasov, S. M. Pshenichnikov, and N. P. Sopina. *Parametric conversion of infrared radiation in an AgGaS2 crystal.* Sov. J. Quantum Electron. **7**, 366–368 (1977).

[26] G. C. Bhar, S. Das, U. Chatterjee, R. S. Feigelson, and R. K. Route. *Synchronous and noncollinear infrared upconversion in AgGaS2.* Applied Physics Letters **54**, 1489–1491 (1989).

[27] A. Smith. *Software: SNLO.* http://www.as-photonics.com/snlo.

[28] J.-J. Zondy, D. Touahri, and O. Acef. *Absolute value of the d_36 nonlinear coefficient of AgGaS_2: prospect for a low-threshold doubly resonant oscillator-based 3:1 frequency divider.* Journal of the Optical Society of America B **14**, 2481 (1997).

[29] B. E. A. Saleh and M. C. Teich. *Fundamentals of Photonics.* Wiley Series in Pure and Applied Optics (John Wiley & Sons, Inc., New York, USA, Aug. 1991).

[30] K. Rottwitt and P. Tidemand-Lichtenberg. *Nonlinear optics: principles and applications* (CRC Press, 2014).

[31] G. D. Boyd and D. A. Kleinman. *Parametric interaction of focused Gaussian light beams.* Journal of Applied Physics **39**, 3597–3639 (1968).

[32] C. Pedersen, Q. Hu, L. Høgstedt, P. Tidemand-Lichtenberg, and J. S. Dam. *Noncollinear upconversion of infrared light.* Optics Express **22**, 28027 (2014).

[33] A. Gavrielides, P. Peterson, and D. Cardimona. *Diffractive imaging in three-wave interactions.* Journal of Applied Physics **62**, 2640–2645 (1987).

[34] L. Wang, Z. Cao, H. Wang, H. Zhao, W. Gao, Y. Yuan, W. Chen, W. Zhang, Y. Wang, and X. Gao. *A widely tunable (5-12.5 μm) continuous-wave mid-infrared laser spectrometer based on difference frequency generation in AgGaS2.* Optics Communications **284**, 358–362 (2011).

[35] E. Takaoka and K. Kato. *Thermo-optic dispersion formula for AgGaS2.* Applied optics **38**, 4577–4580 (1999).

[36] M. Tawfieq, A. Muller, J. Fricke, P. Della Casa, P. Ressel, D. Feise, B.. Sumpf, and G. Trankle. *Extended 9.7 nm tuning range in a MOPA system with a tunable dual grating Y-branch laser.* Optics letters **42**, 4227–4230 (2017).

[37] C. E. DeSantis, J. Ma, A. G. Sauer, L. A. Newman, and A. Jermal. *Breast Cancer Statistics , 2017 , Racial Disparity in Mortality by State.* A Cancer Journal for Clinicians **67**, 439–448 (2017).

[38] L. Wilkinson, V. Thomas, and N. Sharma. *Microcalcification on mammography: Approaches to interpretation and biopsy.* British Journal of Radiology **90** (2017) 10.1259/bjr.20160594.

[39] C. Kendall, M. Isabelle, F. Bazant-Hegemark, J. Hutchings, L. Orr, J. Babrah, R. Baker, and N. Stone. *Vibrational spectroscopy: A clinical tool for cancer diagnostics.* Analyst **134**, 1029–1045 (2009).

[40] M. Sattlecker, R. Baker, N. Stone, and C. Bessant. *Support vector machine ensembles for breast cancer type prediction from mid-FTIR micro-calcification spectra.* Chemometrics and Intelligent Laboratory Systems **107**, 363–370 (2011).

[41] M. Hermes, R. B. Morrish, L. Huot, L. Meng, S. Junaid, J. Tomko, G. R. Lloyd, W. T. Masselink, P. Tidemand-Lichtenberg, C. Pedersen, F. Palombo, and N. Stone. *Mid-IR hyperspectral imaging for label-free histopathology and cytology.* Journal of Optics (United Kingdom) **20** (2018) 10.1088/2040-8986/aaa36b.

[42] G. Shetty, C. Kendall, N. Shepherd, N. Stone, and H. Barr. *Raman spectroscopy: Elucidation of biochemical changes in carcinogenesis of oesophagus.* British Journal of Cancer **94**, 1460–1464 (2006).

[43] N. Stone, C. Kendall, J. Smith, P. Crow, and H. Barr. *Raman spectroscopy for identification of epithelial cancers.* Faraday Discussions **126**, 141–157 (2004).

[44] N. Stone, M. C. Hart Prieto, P. Crow, J. Uff, and A. W. Ritchie. *The use of Raman spectroscopy to provide an estimation of the gross biochemistry associated with urological pathologies.* Analytical and Bioanalytical Chemistry **387**, 1657–1668 (2007).

[45] J. Nallala, G. R. Lloyd, M. Hermes, N. Shepherd, and N. Stone. *Enhanced spectral histology in the colon using high-magnification benchtop FTIR imaging.* Vibrational Spectroscopy (2016) 10.1016/j.vibspec.2016.08.013.

[46] A. S. Haka, K. E. Shafer-peltier, M. Fitzmaurice, J. Crowe, R. R. Dasari, and M. S. Feld. *Identifying Microcalcifications in Benign and Malignant Breast Lesions by Probing Differences in Their Chemical Composition Using Raman Spectroscopy 1.* 5375–5380 (2002).

[47] M. J. Baker, H. J. Byrne, J. Chalmers, P. Gardner, R. Goodacre, A. Henderson, S. G. Kazarian, F. L. Martin, J. Moger, N. Stone, and J. Sulé-Suso. *Clinical applications of infrared and Raman spectroscopy: State of play and future challenges.* Analyst **143**, 1735–1757 (2018).

[48] J. Mansfield, J. Moger, E. Green, C. Moger, and C. P. Winlove. *Chemically specific imaging and in-situ chemical analysis of articular cartilage with stimulated raman scattering.* Journal of Biophotonics **6**, 803–814 (2013).

[49] K. Das, C. Kendall, M. Isabelle, C. Fowler, J. Christie-Brown, and N. Stone. *FTIR of touch imprint cytology: A novel tissue diagnostic technique.* Journal of Photochemistry and Photobiology B: Biology **92**, 160–164 (2008).

[50] C. Kuepper, A. Kallenbach-Thieltges, F. Großerueschkamp, K. Gerwert, H. Juette, and A. Tannapfel. *Quantum Cascade Laser-Based Infrared Microscopy for Label-Free and Automated Cancer Classification in Tissue Sections.* 2018.

[51] A. Ogunleke, V. Bobroff, H. H. Chen, J. Rowlette, M. Delugin, B. Recur, Y. Hwu, and C. Petibois. *Fourier-transform vs. quantum-cascade-laser infrared microscopes for histo-pathology: From lab to hospital?* TrAC - Trends in Analytical Chemistry **89**, 190–196 (2017).

[52] C. R. Petersen, N. Prtljaga, M. Farries, J. Ward, B. Napier, G. R. Lloyd, J. Nallala, N. Stone, and O. Bang. *Mid-infrared multispectral tissue imaging using a chalcogenide fiber supercontinuum source.* Optics Letters **43**, 999 (2018).

[53] S. Mittal, K. Yeh, L. S. Leslie, S. Kenkel, A. Kajdacsy-Balla, and R. Bhargava. *Simultaneous cancer and tumor microenvironment subtyping using confocal infrared microscopy for all-digital molecular histopathology.* Proceedings of the National Academy of Sciences **115**, E5651–E5660 (2018).

[54] Antoni Rogalski. *Infrared Detectors.* Vol. 1542. 9 (2015), pp. 33–36.

[55] N. Pleshko, A. Boskey, and R. Mendelsohn. *Novel infrared spectroscopic method for the determination of crystallinity of hydroxyapatite minerals.* Biophysical Journal **60**, 786–793 (1991).

[56] M. M. Kerssens, P. Matousek, K. Rogers, and N. Stone. *Towards a safe non-invasive method for evaluating the carbonate substitution levels of hydroxyapatite (HAP) in micro-calcifications found in breast tissue.* Analyst **135**, 3156–3161 (2010).

[57] The biopsy was obtained with ethical approval from Gloucestershire Royal Hospitals NHS Foundation Trust and collected by our biomedical partner Nick Stone, a Consultant Clinical Scientist and Professor in Exeter University.

[58] Y.-P. Tseng, C. Pedersen, and P. Tidemand-Lichtenberg. *Upconversion detection of long-wave infrared radiation from a quantum cascade laser.* Optical Materials Express **8** (2018) 10.1364/OME.8.001313.

[59] L. Høgstedt, J. S. Dam, A.-L. Sahlberg, Z. Li, M. Aldén, C. Pedersen, and P. Tidemand-Lichtenberg. *Low-noise mid-IR upconversion detector for improved IR-degenerate four-wave mixing gas sensing.* Optics Letter (2014).

[60] L. Meng, A. Fix, M. Wirth, L. Høgstedt, P. Tidemand-Lichtenberg, C. Pedersen, and P. J. Rodrigo. *Upconversion detector for range-resolved DIAL measurement of atmospheric CH4.* Optics Express **26**, 3850 (2018).

[61] N. Hamburger, H. Hansen, F. Bak, M. Terkelsen, M. Christophersen, L. Bennedsen, Y.-P. Tseng, P. Tidemand-Lichtenberg, and C. Pedersen. *Development and test of optical sensor for real time measurement of volatile organic contaminants in air.* In, Poster Presentation (D3) at 10th international conference on remediation of chlorinated and recalcitrant compounds, Palm Springs, California, USA. (May 2016).

[62] E. Balfanz, J. Fuchs, and H. Kieper. *Polychlorinated biphenyls (PCB) and polychlorinated dibenzofurans and dibenzo (p) dioxins (PCDF/D) in indoor air due to elastic sealants and coated particle boards.* Organohalogen Compounds **13**, 115–118 (1993).

[63] B. Bush and E. Barnard. *Gas phase infrared spectra of 209 polychlorinated biphenyl congeners using gas chromatography with Fourier transform infrared detection: Internal standardization with a 13 C-labelled congener.* Archives of environmental contamination and toxicology **29**, 322–326 (1995).

[64] E. Raptodimos. *Tm-lasers and applications for nonlinear frequency conversion*, Technical University of Denmark (2017).